Title
Flash Converted Graphene Supercapacitors for Industrial Applications

Author
Wang, Lisa

Publication Date
2015

Peer reviewed|Thesis/dissertation

UNIVERSITY OF CALIFORNIA

Los Angeles

Flash Converted Graphene Supercapacitors for Industrial Applications

A dissertation submitted in partial satisfaction of the

requirements for the degree Doctor of Philosophy

in Chemistry

by

Lisa Jiao-Jiao Wang

2015

ABSTRACT OF THE DISSERTATION

Flash Converted Graphene Supercapacitors for Industrial Applications

By

Lisa Jiao-Jiao Wang

Doctor of Philosophy in Chemistry

University of California, Los Angeles, 2015

Professor Richard B. Kaner, Chair

Energy storage devices allow us to charge portable electronics and use them when a wired energy source, such as a power outlet, is not available. One type of energy storage device is a supercapacitor. Supercapacitors store electrical energy through electric double layers and are based on positive and negative ions interacting with the surface of an active material. The active material is very important in determining the supercapacitor's ability to store charge, the time it takes to store charge, and the number of times the supercapacitor can be charged and discharged. The ideal active material has a large accessible surface area and high electrical conductivity. The use of flash converted graphene as an active material in supercapacitors is investigated. These supercapacitors are shown to have capacitive behavior that surpasses that of current commercial supercapacitors. Flash converted graphene is a graphene material prepared by using a flash lamp

to photothermally deoxygenate graphene oxide, an oxidized form of graphite. The flashing process creates a graphene material that has an advantageous 3D corrugated morphology relative to other types of graphene materials.

The first chapter of this thesis is investigates the electrochemical performance of flash converted graphene (FCG) supercapacitor devices. Two methods of making FCG supercapcaitor electrodes are developed and compared. The FCG supercapacitor electrodes were fabricated into coin cells and measured using a potentiostat. The FCG sueprcapcaitors have a specific power that is 10 times higher than that of commercial supercapacitors, whereas the specific energy of the FCG supercapacitors is comparable to that of commercial supercapacitors.

In the second chapter, the FCG electrodes are improved by reducing the amount of oxygen functional groups still adhered to the FCG sheets. The oxygen groups are reduced by annealing the flash converted graphene electrodes in a reducing atmosphere of H_2 gas. The annealing process reduced the oxygen content to 1% and the device retained >88% of its capacitance after 10,000 cycles.

The third chapter describes a novel approach to reducing the resistance of the FCG supercapcitors by using a top-contact method of making a more intimate interface between the current collector and the active material. This top-contact approach uses the sputter deposition of gold to make a homogeneous gold film current collector. The thickness of the gold current collector is controlled by the deposition time. The resistance of the FCG electrodes with a sputter deposited gold current collector is 1.4 times lower than that of the FCG electrodes made with a traditional aluminum foil-based current collector.

The focus of the fourth chapter is to increase the capacitance and hence, the energy density of FCG supercapacitors by compositing FCG with activated carbon. Flash converted graphene/activated carbon composite material improved the frequency response time by a factor of 6 compared to activated carbon supercapacitors. Furthermore, the capacitance of the composite was increased by 15 times compared to FCG supercapacitors.

The fifth chapter of this thesis describes the synthesis and characterization of a mixed-metal metal-organic framework (MOF) using the MOF-74 framework. Because the mixed-metal MOF framework contains more than one type of metal, it has potential to undergo multiple redox reactions. Thus, it is promising for increasing the energy component of supercapacitors when used as an electrode active material.

Illustrated in the sixth chapter is a possible future direction for the FCG supercapcitors. The goal is to further improve the capacitance and energy of FCG supercapacitors, and the approach is by compositing FCG with other materials such as metal-organic frameworks (MOFs). MOFs contain metal oxide moieties that can undergo redox charge storage, while still maintaining a high surface area. In the MOF/FCG composite, the FCG acts as an electron highway, electrically binding the MOF particles together, and serving as a conductive binder.

The dissertation of Lisa Jiao-Jiao Wang is approved.

Xiangfeng Duan

Yang Yang

Richard B. Kaner, Committee Chair

University of California, Los Angeles

2015

I dedicate this dissertation to:

my father, *Dr. Dong Wang*, for teaching me the importance of being myself and believing in myself.

my mother, *Jill Jiao*, for teaching me the importance of humility, humbleness, and respect.

my grandmas, *Yang Shu Fang and Han Gui Zhen*, for teaching me the importance of determination.

Table of Contents

ACKNOWLEDGMENTS

Although the journey has been long and extremely difficult at times, I am very excited to finally reach my educational goals of becoming a doctor. I am now looking forward to the next volume in my life and to tackle the new challenges that await. I will meet those challenges confidently because I am equipped with the skills I have learned during my graduate studies. But developing those skills took an endless amount of time, patience, and support from several people in my life.

I want to express my deepest gratitude to my graduate advisor Prof. Richard Kaner. He has not only given me the resources and opportunity to complete my graduate research but has also prepared me for my journey after graduate studies. He is knowledgeable, wise, and a great teacher. I am so grateful to have him as my graduate advisor.

My gratitude also goes out to my supercapacitor sub-group lab members. Dr. Maher El-Kady deserves my thanks because he was my mentor on supercapcaitors and helped me get started in this new area. I also want to specifically thank Jee Youn Hwang and Yuanlong Shao for their insightful discussions and wonderful friendship. A special thanks also goes to Dr. Sergey Dubin and Matthew Kowal for not only providing me a plentiful supply of graphene oxide, but also for the very practical experimental advice. The two undergraduate students, Rebecca Li and Amylynn Chen, who I had the opportunity to mentor have assisted me on my projects and also warrant my appreciation.

I would also like to thank all of my fellow lab mates from the Kaner group. In particular, I would like to thank Dr. Thomas Farrell, William Huang, Dr. Andrew Lech, Dr. James Ma, Kris Marsh, Brian McVerry, Dr. Jaime Torres, Chris Turner, Dr. Jessica Wang, Dr. Miao Xie, and Michael Yeung for their advice, support, and friendship. Thanks for making these past few years great!

My sincere appreciation goes to my collaborators at Maxwell Technologies, NASA, Aerospace Corporation, and Novacentrix for the wonderful and productive projects we worked on. It was a pleasure to work with you.

I also want to thank the wonderful friends I have met here at UCLA. Specifically, Jenny Chen Link, thank you for being my roommate and best friend. Your courage and brightness has made a magnificent impact on my life and helped me get through the tough times during my graduate journey. Thank you for always being there for me and not only listening to me but also responding with the perfect advice.

Nathaniel Moore, my fiancé, thank you for your love and support through this process. I am so lucky to have met you and have you in my life.

And finally, I especially want to show my loving gratitude and appreciation to the best parents in the world, Dr. Dong Wang and Jill Jiao. Thank you for all the support and for always being there for me even when it's three o'clock in the morning! I am so proud to be your daughter.

Previous Publications and Contributions of Co-Authors:

Chapter 1 is a version of: Lisa J. Wang, Maher F. El-Kady, Sergey Dubin, Jee Youn Hwang, Yuanlong Shao, Kris Marsh, Brian McVerry, Matthew D. Kowal, Prof. Mir F. Mousavi, and Prof. Richard B. Kaner, "Flash converted graphene for ultra-high power supercapacitors." I wrote the manuscript. Maher F. El-Kady, Sergey Dubin, Jee Youn Hwang, Yuanlong Shao helped with scientific discussions. Kris Marsh helped with X-ray photoelectron spectroscopy measurements. Brian McVerry helped with surface area measurements. Matthew D. Kowal helped with synthesizing graphene oxide. Prof. Mir F. Mousavi and Prof. Richard B. Kaner helped edit this manuscript. Funding was provided by the NSF Integrative Graduate Education and Research Traineeship Fellowship. This manuscript will be submitted soon.

Chapter 2 is a version of: Lisa J. Wang, Kris Marsh, Jaime Torres, Prof. Mir F. Mousavi, and Prof. Richard B. Kaner, "Design for specific flash converted graphene supercapacitor properties by reducing the amount of oxygen impurity." I wrote the manuscript. Kris Marsh helped with X-ray photoelectron spectroscopy measurements. Jaime Torres helped with the operation of the furnace. Prof. Mir F. Mousavi and Prof. Richard B. Kaner helped edit this manuscript. Funding was provided by the NSF Integrative Graduate Education and Research Traineeship Fellowship. This manuscript will be submitted soon.

Chapter 3 is a version of: Lisa J. Wang, Maher F. El-Kady, Jee Youn Hwang, Prof. Mir F. Mousavi, Prof. Richard B. Kaner, "Improving energy and power of flash converted graphene supercapacitor electrodes by compositing with activated carbon." I wrote the manuscript. Maher F. El-Kady and Jee Youn Hwang helped with scientific discussions and experiments. Prof. Mir

F. Mousavi and Prof. Richard B. Kaner helped edit this manuscript. Funding was provided by the NSF Integrative Graduate Education and Research Traineeship Fellowship. This manuscript will be submitted soon.

Chapter 4 is a version of: Lisa J. Wang, Rebecca Li, and Richard B. Kaner, "Influence of sputter deposited gold current collector thickness on the capacitive behavior of flash converted graphene supercapacitors." I wrote the manuscript. Rebecca Li helped with experiments. Prof. Richard B. Kaner helped edit this manuscript. Funding was provided by the NSF Integrative Graduate Education and Research Traineeship Fellowship.This manuscript will be submitted soon.

Chapter 5 is a version of: Lisa J. Wang, Hexiang Deng, Hiro Furukawa, Felipe Gándara, Kyle Cordova, Dani Peri, and Omar M. Yaghi, "Synthesis and Characterization of Metal-organic Framework-74 Containing 2, 4, 6, 8, and10 Different Metals", *Inorganic Chemistry*, 2014, 53(12): 5881–5883, DOI: 10.1021/ic500434a. I wrote the manuscript. Hexiang Deng helped collect the solid state NMR data. Hexiang Deng, Hiro Furukawa, Felipe Gándara, Kyle Cordova, Dani Peri, and Prof. Omar Yaghi helped with scientific discussions and editing this manuscript. This manuscript has been published in *Inorganic Chemistry* in 2014. I appreciate *Inorganic Chemistry* for giving me the permission to reproduce the manuscript here.

VITA

2010-2015	Graduate Research Assistant, UCLA
2010-2015	American Chemical Society
2012	NSF Integrative Graduate Education and Research Traineeship Fellow, UCLA
2012	Hanson-Dow Teaching Assistantship Award, UCLA
2010	Bachelors of Arts, Chemistry, Carleton College, MN
2008-2010	Undergraduate Researcher and Laboratory Teaching Assistant, Carleton College, MN
2009	DOE Summer Undergraduate Laboratory Intern, PNNL, WA
2009	DOE Science Undergraduate Laboratory Internship Research Excellence Certificate
2007	NSF Materials Research Science and Engineering Center Internship Researcher, University of Minnesota-Twin Cities, MN

PUBLICATIONS AND SELECTED PRESENTATIONS

Wang, L.J., El-Kady, M.F., Dubin, S., Hwang, J.Y., Shao, Y., Marsh, K., McVerry, B., Kowal, M.D., Mousavi, M.F., Kaner, R.B. “Flash converted graphene for ultra-high power supercapacitors”. (in preparation).

Wang, L.J., Marsh, K., Torres, J., Mousavi, M.F., Kaner, R.B. “Design for specific flash converted graphene supercapacitor performance properties by reducing the amount of oxygen impurities”. (in preparation).

Wang, L.J., El-Kady, M.F., Hwang, J.Y., Mousavi, M.F., Kaner, R.B. “Improving energy and power of flash converted graphene supercapacitor electrodes by compositing with activated carbon”. (in preparation).

Wang, L.J., Li, R., Kaner, R.B. “Influence of sputter deposited gold current collector thickness on the capacitive behavior of flash converted graphene supercapacitors”. (in preparation).

Hwang, J.Y., El-Kady, M.F., Wang, Y., **Wang, L.J.**, Shao, Y., Marsh, K., Ko, J., Kaner, R.B. “Direct preparation and processing of graphene/RuO2 nanocomposite electrodes for high-performance hybrid electrochemical capacitors”, *Nano Letters* (submitted).

Shao Y., El-Kady, M.F., **Wang, L.J.**, Zhang, Q., Li, Y., Wang, H., Mousavi, M.F., Kaner, R.B. “Graphene-based materials for flexible supercapacitors”, *Chemical Society Reviews* (accepted).

Wang L.J., Deng, H., Furukawa, H., Gándara, F., Cordova, K.E., Peri, D., Yaghi, O.M. “Synthesis and characterization of metal-organic framework-74 containing 2, 4, 6, 8, and10 different metals”, *Inorganic Chemistry*, 2014, 53(12): 5881–5883.

Yaghi, O.M, **Wang L.J.**, Deng, H., Suzuki, M. “Metal organic frameworks comprising a plurality of SBUs with different metal ions and/or a plurality of organic linking ligands with different functional groups”, Patent application number: 61/972, 124, filed on March 28, 2014.

Wang, L.J., and Exarhos, G.J. "Persistent conductivity in post-growth doped ZnO films following pulsed UV laser irradiation", *Thin Solid Films*, 2010, 519(5):1495-1500.

Mackey, P.J., El-Kady, M.F., Johansen, M.R., Hogue, M.D., **Wang, L.J.**, Hwang , J.Y., Kaner, R.B., Calle, C.I. “Graphene-based energy storage devices for space applications”, Presented at the 4th International Symposium on Graphene Devices (ISGD-4), Bellevue, WA, September 21-25, 2014.

Wang, L.J., Gross, D.S., Dutcher, D.D., Olson, B., Kuehn, T.M. “Chemical composition of cooking aerosols”, Poster presented at the American Chemical Society National Meeting, San Francisco, CA, March 21 – 25, 2010. **Poster selected as one of 21 presentations out of ~12,500 for a press release by ACS.**

Wang, L.J., Wanamaker, C.L., Hillmyer, M.A. “Homo-polymerization of lactide and γ-butyrolactone with Zn(II) alkoxide catalyst”, Poster presentation at University of Minnesota, Minneapolis. 2007.

Chapter 1: Flash Converted Graphene for Ultra-High Power Supercapacitors

Abstract

Supercapacitors are known for their rapid energy charge-discharge properties, often ten to a hundred times faster than batteries. However, there is still a demand for supercapacitors with even faster charge-discharge characteristics to fulfill the requirements of emerging technologies. The power and rate capabilities of supercapacitors are highly dependent on the morphology of their electrode materials. An electrically conductive 3-dimensional porous structure possessing a high surface area for ions to access is ideal. Using a flash of light, we have developed a method to produce highly interconnected 3D graphene architectures with high surface area and good conductivity. The flash converted graphene is synthesized by reducing freeze-dried graphene oxide using an ordinary camera flash as a photothermal source. The flash converted graphene is used in coin cell supercapacitors to investigate its electrode materials properties. The electrodes were fabricated using either a pre-coating flash conversion or a post-coating flash conversion of graphene oxide. Both techniques produced supercapacitors possessing high power and ultra-high rate capabilities (5-7 x 10^5 W/kg). Furthermore, optimized supercapacitors retained >50% of their capacitance when operated at an ultrahigh current density up to 220 A/g_{FCG}.

1.1 Introduction

Electric double-layer capacitors (EDLCs), a type of supercapacitor, are energy storage devices that can be charged and/or discharged within seconds, provide high power, and operate under much higher currents than can be withstood by batteries. Carbon-based supercapacitors are

currently a $1 billion industry which is projected to grow to more than $3 billion within five years because of the demands for advanced consumer products[1-3] that require fast storing and retrieval of energy. These technologies include vehicle ignition, pitch control in wind turbines, cold starting of trucks, load leveling from renewable energy sources, and space exploration applications.[4-7] In regard to the latter, high specific power (by mass) is required for satellites, and space station operations.[8,9,10,11,12] Thus, EDLCs have favorable charge-discharge properties; providing high power and the ability to operate at high rates suitable for these advanced applications.

Traditional methods for the production of supercapacitor electrodes involve mixing a carbon source, such as activated carbon, with an insulating binder that is cast onto a current collector.[4,13,14] The carbon materials used in these traditional methods generally exhibit low conductivity, especially when compared to graphene. The conductivity of chemically converted graphene (CCG) is ~7,200 S/m (close to that of pristine graphite),[15,16] while the conductivity of activated carbon is only 10-100 S/m.[17] Graphene is composed of planar sheets of sp^2 hybridized carbon atoms containing large networks of delocalized π electrons resulting in very high conductivity.[18] When used in supercapacitor electrodes, graphene's planar structure gives rise to fast charging and discharging because the electrolyte ions can readily access the large surface areas of the sheets.[7,19] The efficient transport of ions between the electrolyte and graphene surfaces is advantageous for high power and rate capabilities and rapid response times. However, processing graphene can be problematic. The planar aromatic sheets often restack due to favorable π-π interactions between adjacent sheets.[20,21] Upon restacking, the graphene is

converted back into a graphite-like material and no longer possesses the high surface area of single layer graphene, reducing the material's high power and rate capabilities.[22]

Well-known methods for producing graphene include chemical conversion from graphene oxide,[15,23,24] intercalation and exfoliation of graphite,[14,25,26] thermal conversion of graphene oxide,[27] and electrochemical reduction of graphene oxide.[28] These methods yield robust graphene, but as mentioned above, the sheets readily restack leading to dense packing and loss of surface area.[22] Our group has recently developed a method for the preparation of graphene via the photothermal reduction of graphene oxide using the flash from a camera. The result of the reduction is a low density, 3-dimensional graphene architecture that is ideal as an electrode material.[29] Figure 1.1 shows images of chemically converted graphene and flash converted graphene for comparison. Photothermal conversion creates a disordered corrugated graphene structure in which adjacent sheets are no longer oriented parallel to each other. The photothermal conversion can be accomplished with different light sources, e.g. using a LightScribe with a 780 nm laser[30] or using a flash lamp.[29] The latter method, known as flash converted graphene, offers a scalable method to produce graphene from graphene oxide that minimizes restacking of sheets.

In electric double-layer capacitors, the electrode must soak in the electrolyte solution to allow diffusion of ions to the available surfaces of the elctrode. When applying a charging or discharging current, the ions travel atomic distances to/from the electrode surfaces thereby creating/dispensing capacitance.[31,32] A 3D corrugated foam structure is advantageous because it maximizes the exposed surfaces.[33-36] Therefore, flash converted graphene (FCG) could be an ideal material for electric double layer capacitors (EDLCs) (Figure 1.2).

Here, we demonstrate the use of FCG as an electrode material in graphene-based supercapacitors. A commercially available flash lamp is used to produce FCG, which is processed into binder-free coin cell supercapacitors. Two highly scalable and versatile protocols for fabricating the FCG electrodes are reported. In the first method, bulk graphene oxide is first converted to FCG (pre-FCG), then cast onto a current collector. For the second method, the graphene oxide solution is first cast onto the current collector, then converted to FCG (post-FCG) (Figure 1.3). Both methods produce supercapacitors that exhibit exceptional specific power, response time, and rate capability. The FCG supercapacitors possess many properties superior to other EDLCs. The specific power and rate capabilities of pre-FCG and post-FCG are among the highest reported for graphene-based supercapacitors (Table 1.1). Furthermore, the specific power of the FCG devices are ten times higher than that of carbon-based commercial supercapacitors (Table 1.2).

1.2 Results and Discussion

Based on the mechanism of electric double-layer capacitors, surface area is a crucial factor in determining the energy storage capabilities. Since EDLC supercapacitors store charge through the electric double-layer of ions formed on the exposed surfaces of the electrode active material, a larger active material surface will, therefore, store more charge.[13, 31] Graphene converted from a flash lamp (FCG) has a desirable increased surface area relative to many other forms of graphene materials. The combined effects of freeze-drying and flashing graphene oxide produce a low-density, high surface area material with a porous network of graphene sheets. Freeze-drying the aqueous dispersion of graphene oxide acts to pre-set the density of the cast

material, essentially immobilizing the graphene oxide molecular configuration as it exists as a dispersion. As an aqueous colloidal, the graphene oxide interacts with water molecules forming hydrogen bonds and aggregates to create a low-density morphology. Upon flashing, the reduced, freeze-dried graphene oxide slightly expands. This expansion can be attributed to the conversion of the oxygen functional groups on graphene oxide from C-OH, C=O, C-O-C, and –COOH into gaseous CO_2, and H_2O, along with some residual SO_2 from the synthesis. The presence of CO_2, H_2O, and residual SO_2 gases was confirmed by gas chromatography-mass spectrometry (GC-MS) with H_2O at 18.1 m/z the most abundant, followed by CO_2 at 44.0 m/z, and SO_2 at 63.9 m/z (Figure 1.4). Thus, the expansion of FCG and creation of a 3D porous network is related to the emission of CO_2, H_2O, and SO_2 gases from the graphene oxide sheets.

SEM images of the FCG electrode films from each coating method show a highly porous 3D morphology (Figure 1.5). The post-FCG electrode exhibits a corrugated cardboard-like structure with interconnected structures in fractal-like geometry. The post-FCG electrode has a even greater degree of 3D corrugated morphology because the graphene is converted on the current collector after casting, whereas pre-FCG is converted before casting and dispersed in a solvent prior to casting. The dispersion in solvent may facilitate some restacking of the sheets. The 3D morphorlogy of FCG enables a small diffusion barrier allowing electrolyte ions to readily access the surfaces of FCG.

The BET surface area of FCG (733 m^2/g) is higher than that of the starting material, graphene oxide (15 m^2/g) (Figure 1.6), but does not reach the theoretical specific surface area of

graphene (2630 m^2/g).[18] The lower surface area of FCG may be due to incomplete reduction of graphene oxide or some restacking of graphene sheets.

X-ray photoelectron spectroscopy (XPS) and X-ray difraction (XRD) were carried out on the FCG to shed light on the extent of the π conjugation by investigating the amount of remaining unreduced oxygen. The percentages of carbon and oxygen in pre-FCG are 79.0% and 21.0%, respectively, while post-FCG electrodes contain 85.6% carbon and 14.4% oxygen (Figure 1.7). Comparing the XRD pattern of FCG to that of GO indicates that the majority of GO was reduced to graphene during the flashing process (Figure 1.8). The post-FCG shows no diffraction peaks, whereas the pre-FCG shows two small intensity peaks that indicate the presence of some graphene oxide. Since the flash lamp emits a high power pulse of light energy the graphene oxide is heated locally. The heat penetrates deeper below the surfaces of the electrode material with more flash treatments. Because post-FCG is first cast into a GO film on the current collector before the flashing process, the photothermal energy can penetrate the thin film of graphene oxide, resulting in more complete reduction. In contrast, pre-FCG is flashed as bulk GO powder before casting. The bulk freeze-dried GO is thicker than its cast post-FCG counterpart, which can prevent the penetration of light and thus heat from the flash to reach all of the underlying material. Any unreduced oxygen will act as a barrier for the delocalized π system in the graphene sheets, thereby, limiting the electrical conductivity.[15]

Along with electrode morphology, the electrical conductivity plays a key role in the performance of a supercapacitor. The conductivity of a carbon material depends on the delocalization of π-electrons throughout the system. Pristine graphite has high conductivity

because of its large delocalized π system. Graphene oxide, in contrast, possesses a low conductivity because the π system is disrupted by sp^3 carbons bound to oxygen atoms or oxygen containing carbonyl or epoxide groups. When converted with a flash, the resulting FCG material exhibits relatively good conductivity of 60.7 S/m (Equation 1.1) compared to the resistive GO starting material (<0.01 S/m). The conductivity of FCG is comparable to activated carbon electrodes (10-100 S/m), but lower than chemically converted graphene (~7,200 S/m),[15,16,17] probably due to incomplete reduction during the flash process.

To test the performance of the FCG electrodes in supercapacitors, devices were fabricated from both methods. The pre-FCG and post-FCG electrodes both demonstrate electric double layer behavior with good capacitance, and extremely high specific power and rate capabilities. The specific power and rate capabilities are significantly higher than many state-of-the-art supercapacitors as determined from both cyclic voltammetry, and constant current electrochemical measurements (Figure 1.9). The gravimetric capacitance of the pre-FCG supercapacitor device is 48 $F/g_{FCG/electrode}$ and that of the post-FCG supercapacitor device is 64 $F/g_{FCG/electrode}$ using a 0 to 2 V window at a current density of 1 A/g_{FCG}. At 10 A/g_{FCG} from 0 V to 2 V, the gravimetric capacitance of pre-FCG and post-FCG is 40 $F/g_{FCG/electrode}$ and 60 $F/g_{FCG/electrode}$, respectively. When increased to a 2.6 V window, the capacitance of post-FCG doubled to 88 $F/g_{FCG/electrode}$. The corresponding specific energy of pre-FCG and post-FCG supercapacitor devices (based on the total FCG active material) at 1 A/g_{FCG} are 7 Wh/kg and 9 Wh/kg, respectively. Compared with other recently reported electric double layer capacitors such as 3D sponge-like graphene (SPG) and graphene hydrogels,[37,38] the FCG CR2032 coin cell

supercapcitor devices show improved electric double layer behavior, with higher rate capabilities by greater than a factor of two, while possessing comparable specific energy (Table 1.1). Additionally, the FCG CR2032 devices exhibit significantly higher power than the majority of graphene EDLCs currently reported. The specific power for pre-FCG and post-FCG at 1 A/g_{FCG} from 0 V to 2 V is 5 x 10^5 W/kg and 7 x 10^5 W/kg, respectively. FCG devices possess specific power over two times that of microwave exfoliated GO (a-MEGO),[39] one order of magnitude higher than 3D SPG[37] and pilliared graphene paper (GP),[40] and two to three orders of magnitude higher than a thermally reduced melamine resin functionalized GO (cMR-rGO_{th}), a hydrazine reduced GO (rGO_H), a carbon nanotube GO composite (CNT-rGO_{th}),[41] and graphene hydrogels.[38] Although many of the reported electrode active materials represent important contributions to EDLC research, few appear scalable. On the other hand, flash converted graphene appear to be readily scalable. Furthermore, the specific power of FCG CR2032 coin cell supercapacitor devices is one order of magnitude higher than that of several common commercial devices (Table 1.2).[42]

Density plays an important role in the gravimetric and volumetric performance of supercapacitor devices. The post-FCG electrode has a very low density (0.0080 g/cm^3) and exhibits higher specific energy and power, but lower volumetric capacitance (1.2 x 10^{-1} $F/cm^3_{/device}$). The pre-FCG electrode density is 0.039 g/cm^3 and shows a lower specific energy and power, but a higher volumetric capacitance (2.5 x 10^{-1} $F/cm^3_{/device}$). The density of the electrode material is important because a lower density means it has more void space, not only allowing more surface area for ion adsorption, but also for faster ion transport. However, the low

density FCG electrode is not as robust, with less adhesion between the material and the current collector than denser electrodes. Thus, the rate capability of pre-FCG is greater than that of post-FCG. However, both pre-FCG and post-FCG are made from purely carbon materials, with no binders or other inactive additives. This has the advantage of easy production with the potential for lower cost and toxicity.[13]

The high power of the FCG devices can also be deduced from the rectangular cyclic votammogram (CV) shape, even at high scan rates of 1000 mV/s. The sharp vertical transition at 0 V and 2 V in the CV indicates very low active material resistance resulting in low equivalent series resistance (ESR) and high power. This is further supported by the fast time response found through electrochemical impedance spectroscopy. The time response obtained from a Bode Plot of the devices are 4.6×10^{-1} seconds for pre-FCG and 2.3×10^{-1} seconds for post-FCG (Figure 1.10).

On a mechanistic level, the precise rectangular shape of the CV indicates ideal electrochemical double layer formation during charging and discharging of current. The storage of electrons is mainly due to adsorption of ions on the surfaces of the graphene sheets. Thus, the pure EDL behavior enables the fast response and speed of ion adsorption on the FCG active material, thereby giving rise to an enhanced power density. Additionally, post-FCG can be run at an even higher potential window. A preliminary test of the device at 2.6 V gave a capacitance of 88 $F/g_{FCG/electrode}$, a 36% increase in capacitance when compared to that obtained with a 2 V window.

Electrochemical impedance spectroscopy was employed on the FCG supercapacitor devices at open circuit potential from 1 MHz to 10 mHz to further characterize their electrochemical behavior (Figure 1.11). Both pre-FCG and post-FCG devices show capacitance behavior at high frequencies of 360.6 Hz and 178.9 Hz, respectively, translating to fast time responses. The time response from the Bode plot at -45° for pre-FCG is 4.6×10^{-1} seconds and for post-FCG is 2.3×10^{-1} seconds. The equivalent series resistance (ESR) of pre-FCG is estimated to be 5.1 ohms and that of post-FCG is estimated to be 0.9 ohms. The ESR of the FCG electrodes is exceedingly low. The post-FCG electrode has an ESR even lower than other reputed electrode materials including a-MEGO (4.6 ohms)[39] and graphene hydrogel (3.5 ohms).[38] The low ESR values of FCG are consistent with EDL formation and fast ion transport.

Both pre-FCG and post-FCG CR2032 coin cell devices retained 50% relative capacitance at a fast rate of 220 A/g_{FCG}, but even more impressive is that pre-FCG and post-FCG devices retained >1% relative capacitance at 900 and 500 A/g_{FCG}. One of the leading graphene-based supercapacitors, graphene hydrogels, was reported to retain 70% relative capacitance at 20 A/g.[38] Here, the FCG electrodes retain 77% and 86% relative capacitance at 20 A/g. Furthermore, as a comparison, three commercial supercapacitors retained 50% relative capacitance at only 5-40 $A/g_{\text{total active material}}$, and retained >1% relative capacitance only up to 12-80 $A/g_{\text{total active material}}$. The superior rate capability of FCG supercapacitors make them potentially attractive for applications such as load leveling and space exploration.

Finally, the cycle stability of FCG devices were tested. A device of post-FCG was taken as an example and charged and discharged over 5000 times at 1 A/g_{FCG}. The device retained

78.5% capacitance after 1000 cycles and after that remained nearly constant up to 5000 cycles (Figure 1.12). The loss in capacitance may be due to impurities such as incomplete removal of water before device assembly. Water facilitates the decomposition of the organic electrolyte rendering a device less stable. Another possibility is the presence of residual oxygen from the flash conversion process of graphene oxide to FCG. Oxygen serves as a redox contributor, thereby making the device less stable.[43,44] Nevertheless, the FCG devices still show good cycle stability in terms of capacitance as well as power. The IR drop increased only 16.6% after 1000 cycles, with retention of 85.7% of its power.

1.3 Conclusions

The photothermal conversion of GO to graphene via a flash lamp yields FCG with a 3D framework, causing a 3D structure that effectively prevents restacking of sheets. Two new methods for fabricating FCG into devices known as pre-FCG and post-FCG are demonstrated with specific energies of 7 and 9 Wh/kg, and extremely high power (5×10^5 W/kg and 7×10^5 W/kg) and rate capabilities (900 and 500 A/g). The power and rate capability of the FCG CR2032 coin cell devices are higher than that of many state-of-the-art graphene-based CR2032 coin cell supercapacitors and higher than that of several commercial supercapacitors (Figure 1.13). The flash method is also straightforward, versatile and scalable. FCG supercapcitors are readily made into commercially viable form factors such as coin cells that could be used in a wide range of applications.

1.4 Experimental Section

1.4.1 Preparation and Fabrication of pre-FCG Electrodes

The precursor to FCG, graphene oxide, was prepared from natural flake graphite using a modified Hummer's Method.[15,45,46] Graphene oxide in an aqueous dispersion (2.6% wt) was freeze-dried using a Labconco Freezone 1L Freeze dry system with the lypholizer vacuum set at 0.020 torr at a temperature of -51 °C. The freeze-dried graphene oxide was transferred to 20 mL scintillation vials (15 mg in each vial) with caps slightly loose. A flash lamp (Alien Bees B1600) was used at full power (640 J) to reduce the graphene oxide and convert it into flash reduced graphene. Each vial was flashed 10 times to ensure that all GO was converted to graphene. 100 mg of FCG was transferred into a new vial. 5 mL of deionized water and 5 mL of ethanol was added to the FCG. The contents were stirred for 30 min on a stir plate and bath sonicated for 99 min at room temperature. Each vial was placed in a vacuum oven at 60 °C for 20 min to remove some solvent and increase the viscosity of the dispersion. The dispersion was then sonicated for 1 min just before casting. A sheet of carbon coated aluminum current collector was placed onto the Gardco automatic drawdown machine II with vacuum to keep the film as flat as possible. 2 mL of the dispersion was transferred to the current collector and was cast at a blade height of 254 micrometers. The cast film was then transferred to an oven and dried at 40 °C overnight.

1.4.2 Preparation and Fabrication of post-FCG Electrodes

The starting material, graphene oxide, was prepared in the same way as that used in pre-FCG [15,45,46] and cast onto carbon coated aluminum foil current collectors using a Gardco automatic drawdown machine II at 610 micrometers. The cast GO film was immediately placed into a liquid nitrogen bath and frozen before being loaded into the lypholizer (Labconco Freezone 1L Freeze dry systems). After the film was freeze-dried overnight (0.018 torr and -51

°C), it was exposed to a flash lamp (Alien Bees B1600) at a flash power of 160 J. The light brown colored GO foam turned darker incrementally, becoming completely black after three flashes.

1.4.3 Morphology, Composition, and Properties

Conductivity of FCG was determined after pressing FCG powder into a pellet with a Carver Press set at 1000 lbs for 10 min, by making a two-point probe measurement using a voltmeter. Several equidistant squares were painted onto the surface of the pellet using silver paint to provide improved contact with lower resistance to the voltmeter probes. The length, width, and height (thickness) between the two squares were measured and conductivity was determined using Equation 1.1:

$$\sigma = \frac{length}{R \bullet width \bullet height}$$

(Eq. 1.1)

Where

R = measured sheet resistance in ohm;

σ = conductivity (Siemens/m or ohms/m)

Nitrogen BET surface area measurements were taken on a Micromeritics Instrument Corporation TriStar II 3020 V1.03 (V1.03) at 77.3 K. XRD patterns were collected on a Bruker D8 Discover Powder X-ray Diffractomator using Cu K_α radiation (λ = 1.5406 Å). The 3D morphology of pre-FCG and post-FCG shown from the SEM images were taken on a FEI Nova 230 Nano SEM. XPS studies were carried out on a Kratos AXIS Ultra DLD with a monochromatic Al Kα X-ray source operating at 10 mA and 15 kV. Survey spectra and individual high-resolution spectra were collected using pass energies of 160 eV and 20 eV, respectively. Data processing were performed using CasaXPS 2.3 software, and spectral binding energies were calibrated by assigning the hydrocarbon peak in the C 1s high-resolution spectra to 284.6 eV. GC-MS experiments were carried out on an Agilent 6890-5975 GC-MS using helium as a carrier gas and argon as the control. Freeze-dried GO was sealed in a vial with a septum cap under an argon atmosphere in a glovebox. The Freeze-dried GO was then converted to FCG via flashing and 1 mL of the air surrounding the FCG in the vial was extracted with a syringe and injected into the GC-MS (G3174A) for analysis.

1.4.4 Assembly of FCG Electrodes into Coin Cell Supercapacitor Devices

For both methods, the process to assemble FCG electrodes into CR2032 coin cell devices was the same. 15 mm diameter discs were punched from the electrodes using a 15 mm diameter round hole arch punch (McMaster-Carr). These discs serve as the electrodes in the coin cell supercapacitor. Each electrode was weighed using a microbalance, and the thicknesses were measured using a micrometer. The assembly of the coin cell (CR2032) device was made by starting with the bottom cap and gasket, then adding the electrodes, the polypropylene separator

(17 mm diameter), the electrolyte (1.0 M tetraethylammonium tetrafluoroborate ($TEABF_4$) in acetonitrile), then adding the spacer, spring, and the top cap. Finally, the stack was crimped shut. Devices were made in both air and in a nitrogen filled glove bag. There was no noticeable difference in the results of the cells made in air versus those made under nitrogen. The time it takes to build a device, from inserting electrolyte to sealing the cell is only about 20 seconds.

1.4.5 Calculations

The capacitances were calculated from cyclic voltammetry data and constant current measurements using a potentiostat (Biologic VMP3) with a 10 Amp booster (VMP3b-10). The equation for capacitance calculations is:

$$C = \frac{i\Delta t}{\Delta V} \qquad \text{(Eq. 1.2)}$$

Where

$C = capacitance\ (F)$;

$i =$ current (A);

$\Delta t = discharge\ time$;

$\Delta V = discharge\ voltage$;

$\frac{\Delta V}{\Delta t} = scan\ rate\ in\ cyclic\ voltammetry$

The resulting capacitance value can then be divided by weight to give gravimetric capacitance. The capacitance based on FCG for one electrode ($F/g_{FCG/electrode}$ or $F/cm^3_{FCG/electrode}$) is calculated by multiplying the capacitance from Equation 1.2 by a factor of four. The factor of four compensates for the 50% decrease in mass or volume going from a single device to per

electrode, and the circuit translation from a device (two electrodes in series) to per electrode (not in series).

$$C_s = \frac{c}{m}$$

Where (Eq. 1.3)

$C_s = specific\ capacitance\ (F/g)$

$m = mass\ of\ active\ material$ (g)

The specific energy is then calculated.

$$E = \left(\frac{1}{2}\right) C_s \Delta V^2$$

Where (Eq. 1.4)

$\Delta V = voltage\ window$

The specific power can also be calculated from constant current data, by using the IR drop value:

$$specific\ power = \frac{(\Delta V)^2}{4mESR} \quad \text{(Eq. 1.5)}$$

Where

$\Delta V = operating\ voltage$

$m = mass\ of\ active\ material$ (g)

$ESR = equilvalent\ series\ resistance$ (ohm)

For the rate capability, the current values were calculated by multiplying the weight by the desired current density (A/g), i.e. 5, 10, 20 A/g. After collecting the data, and calculating the capacitances, the relative capacitance was obtained by dividing each capacitance by the

capacitance measured at 1 A/g. A plot was then made to illustrate the trend. The current density at which the device can retain 50% of capacitance and where the device reaches <1% of capacitance can be readily obtained from these results.

1.4.6 Electrochemical Measurements

Electrochemical properties and results were determined using a Biologic VMP3 potentiostat and a VMP3b-10 10 Amp booster. The devices were measured with a 4-point holder for coin cells. Cyclic voltammetry (CV) and constant current (CC) was obtained from 0 V to 2 V. The stable voltage window (2 V) was determined through CV at 100 mV/s at different voltages (Figure 1.14). Electrochemical Impedance Spectroscopy (EIS) was also taken on the Biologic VMP3 over a frequency range from 1 MHz to 10 mHz at open circuit potential. The cycle life stability was investigated by using constant current charge-discharge from 0 to 2 V at 1 A/g for 5,000 cycles.

1.5 Tables and Figures

Table 1.1 Comparison of FCG and State-of-the-Art Graphene Supercapacitors

Sample	Reference	Synthesis Method	Wh/kg	W/kg	IR Drop (V)	Rate Capability (70%) (A/g)
pre-FCG	Present work	Flash	7	$5x10^{5}$	$2.9x10^{-3}$	$4.5x10^{1}$
post-FCG	Present work	Flash	9	$7x10^{5}$	$3.2x10^{-3}$	$9.0x10^{1}$
3D SPG	37	Microwave	7	$5x10^{4}$	---	---
Graphene hydrogel	38	Hydrothermal	4.5-6.5	$<5x10^{3}$	---	$2.0x10^{1}$
a-MEGO	39	Exfoliation-Activation	70	$3x10^{5}$	$3.4x10^{-2}$	---
Pillared GP	40	Exfoliation-Chemical	26	$5x10^{4}$	---	---
cMR-rGO_{th}	41	Functionalized-Thermal	6-25	$<4x10^{3}$	---	---
rGO_{H}	41	Chemical	3-14	$<3x10^{3}$	---	---
CNT-rGO_{th}	41	Microwave-Thermal	4-5	$<1x10^{3}$	---	---

Table 1.2 Comparison of FCG and Commercial CR2032 Supercapacitors

Sample	g/cm^3	$F/g_{/electrode}$ (1 A/g)	Wh/kg	W/kg	IR Drop (V)	Rate Capability (50%) (A/g)
pre-FCG	0.039	48	7	$5x10^5$	$2.9x10^{-3}$	$2.2x10^2$
post-FCG	0.008	64	9	$7x10^5$	$3.2x10^{-3}$	$2.2x10^2$
Commercial EC1	0.540	44	6	$7x10^4$	$2.9x10^{-2}$	$4.0x10^1$
Commercial EC2	0.480	80	11	$6x10^4$	$3.3x10^{-2}$	$2.0x10^1$
Commercial EC3	0.036	80	11	$6x10^4$	$2.9x10^{-2}$	$5.0x10^0$

A) 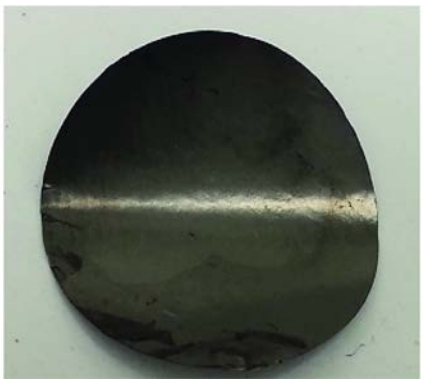 B) 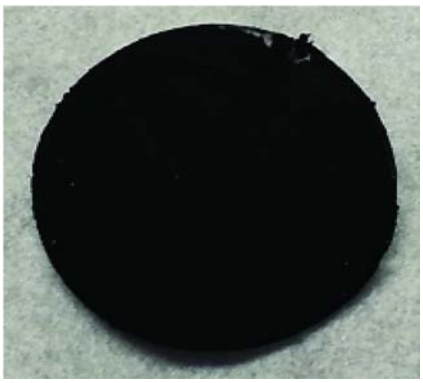

Figure 1.1 Graphene electrodes: A) A smooth chemically converted graphene membrane. B) A rougher, expanded graphene membrane made by photothermal conversion of graphene oxide.

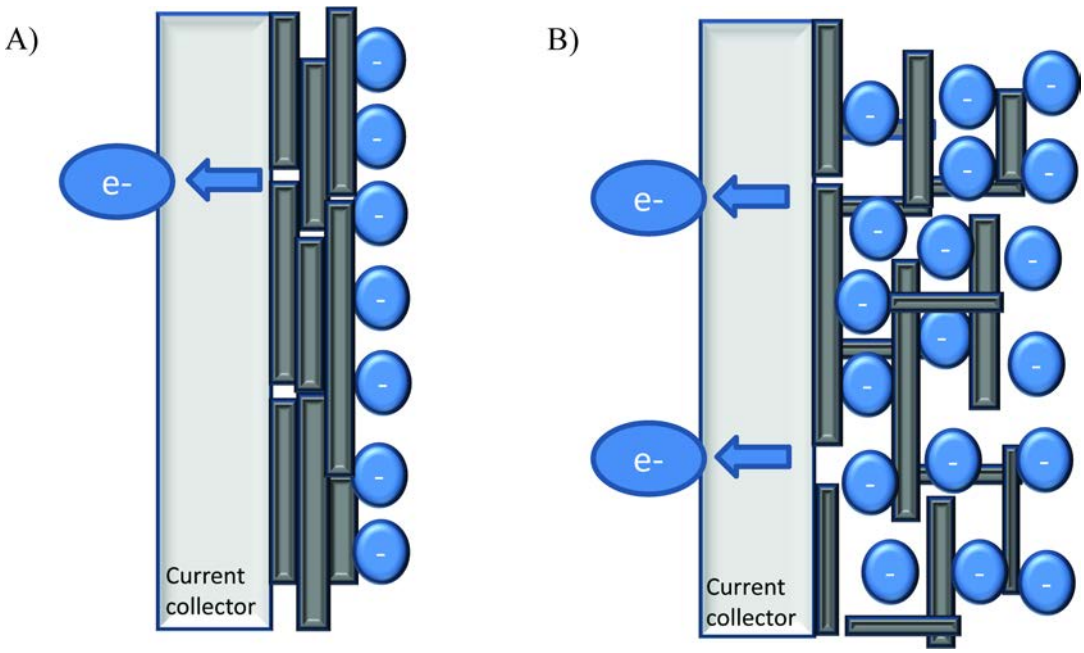

Figure 1.2 Schematic diagram of ions from the electrolyte absorbing onto the accessible surfaces of the electrode active material. A) Ion adsorption occurs only at the surface of the electrode film because of its densely packed morphology. B) Ion adsorption occurs throughout the electrode active material because of its less dense corrugated 3D morphology.

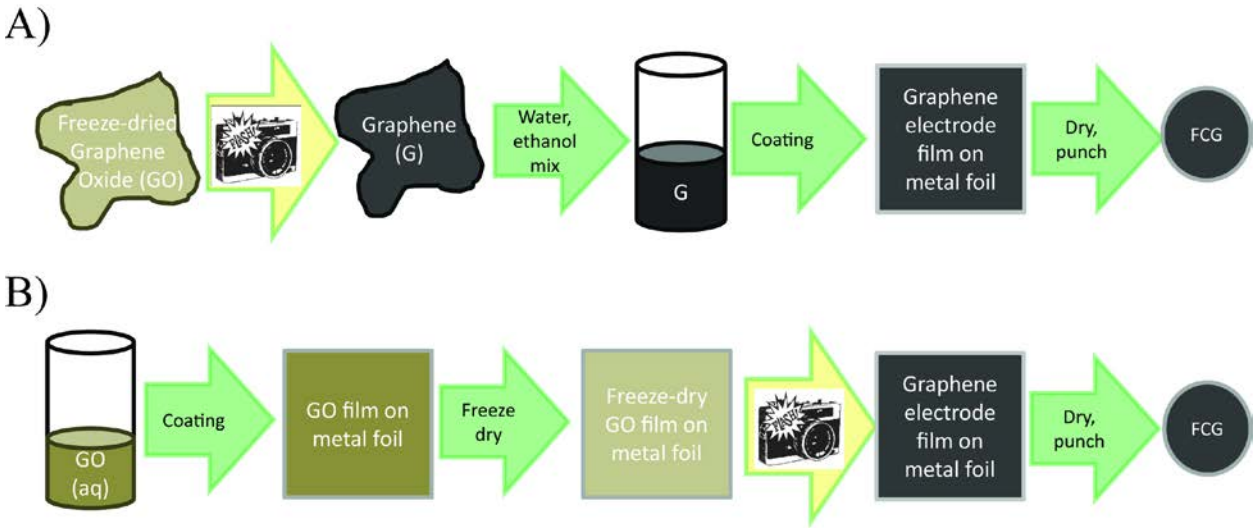

Figure 1.3 The two methods for making FCG electrodes: A) pre-coated flash conversion (pre-FCG) and B) post-coated flash conversion (post-FCG).

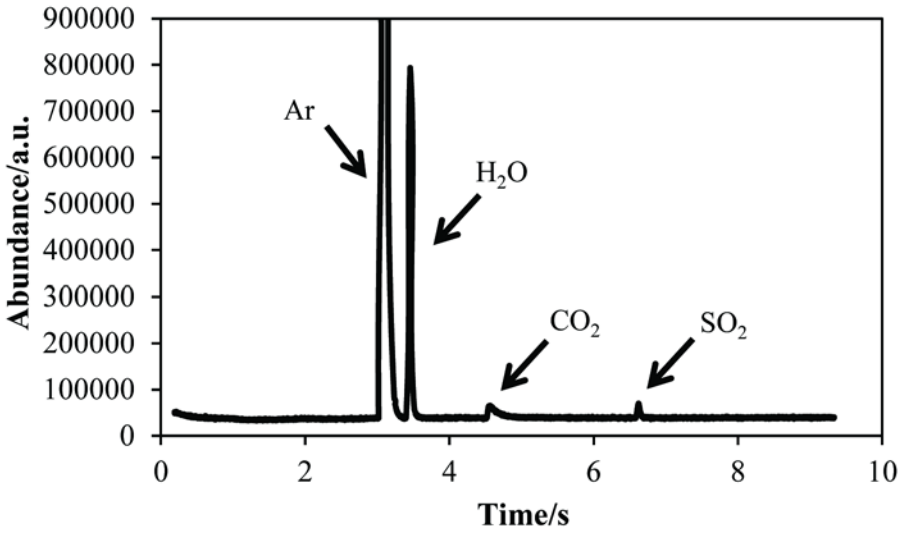

Figure 1.4 GC-MS spectra of gas after flashing freeze-dried GO in a sealed vial filled with argon.

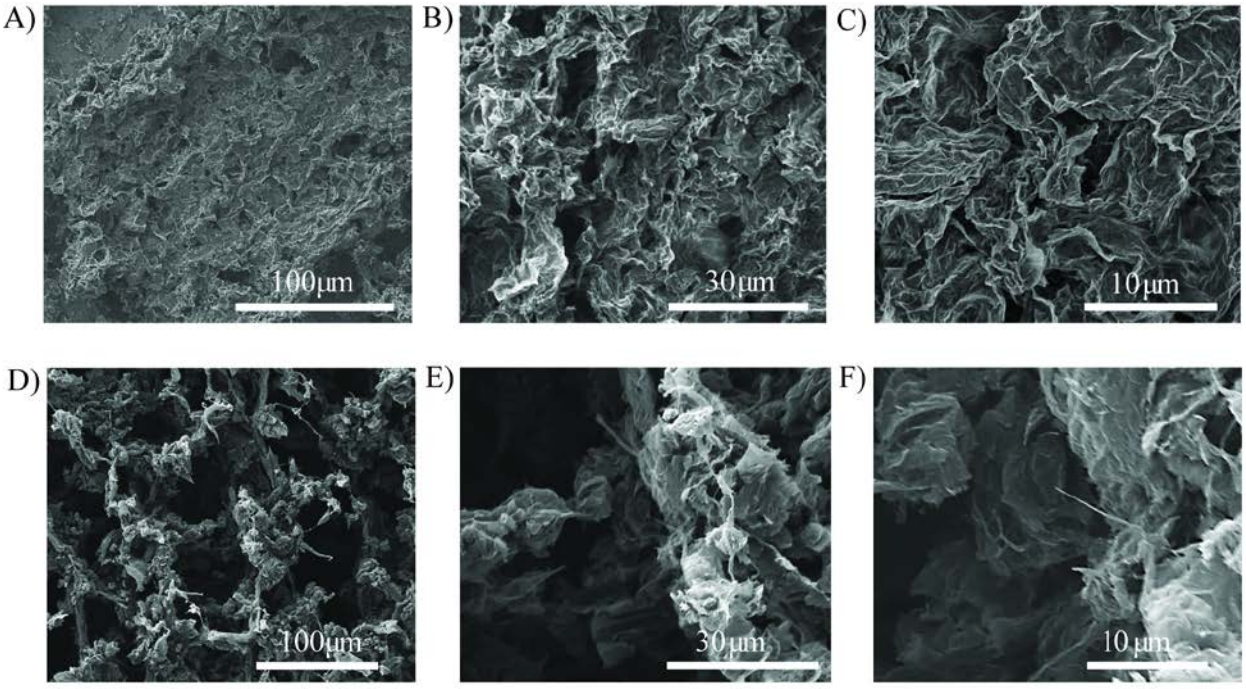

Figure 1.5 SEM images of A-C) pre-FCG, D-F) post-FCG at 0.5 k, 2 k, and 5 k magnification showing the corrugated porous morphology.

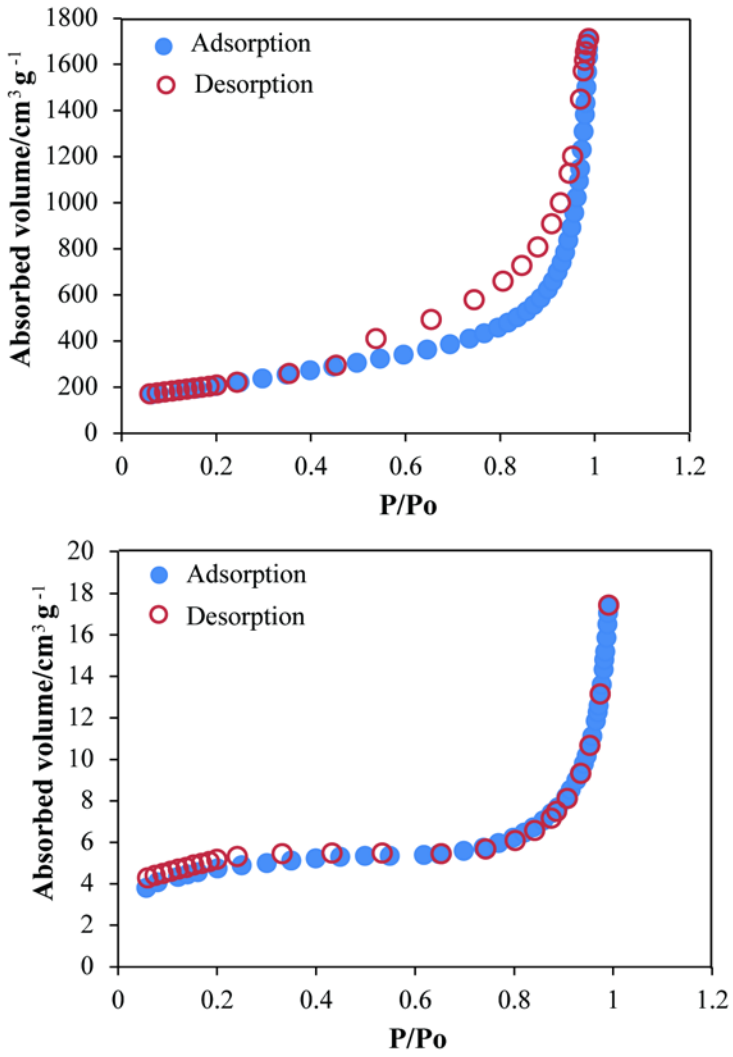

Figure 1.6 BET nitrogen (77 K) adsorption isotherms for FCG powder used in the electrodes (top) and for graphene oxide (GO) (bottom). The FCG BET surface area is 733 m^2g^{-1}, whereas the BET surface area of the freeze-dried GO is only 15 m^2g^{-1}.

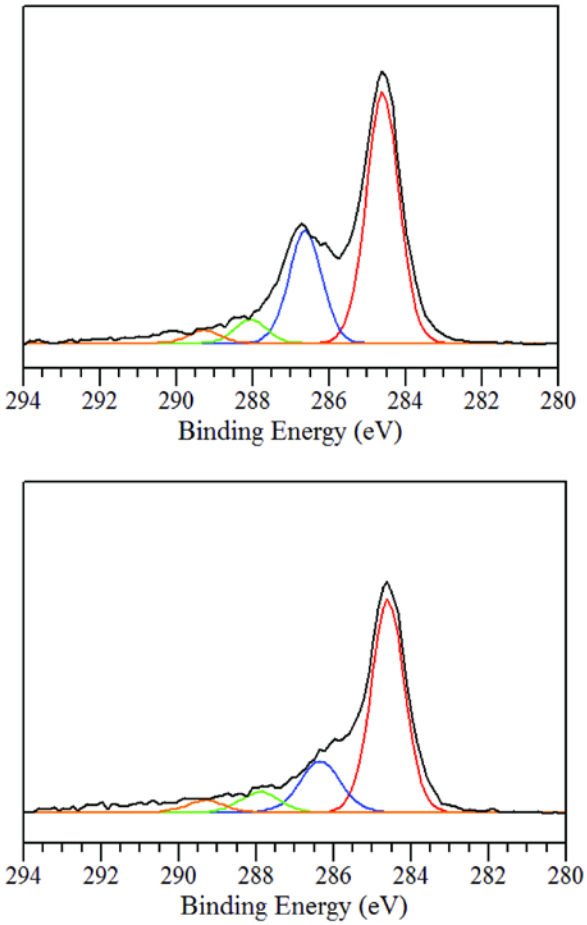

Figure 1.7 XPS high-resolution C 1s spectra of pre-FCG (top) and post-FCG (bottom). The spectral component at 284.6 eV (red) corresponds to sp^2 carbon. Oxygen containing groups, such as C-OH, C=O/C-O-C, and –COOH are shown at 286.7 eV (blue), 288.0 eV (green), and 289.3 eV (orange), respectively.

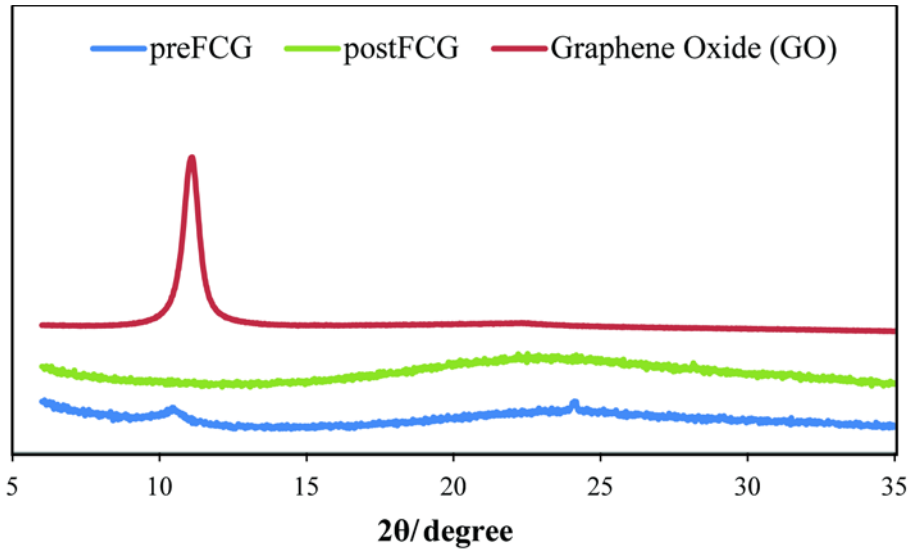

Figure 1.8 X-ray diffraction pattern comparing flash converted graphene used for electrodes (pre-FCG and post-FCG) to GO. A distinct peak in the GO pattern can be seen at 12° 2θ, but only small diffraction peaks are present for pre-FCG and no peaks for post-FCG. The lack of peaks indicates a disordered 3D morphology.

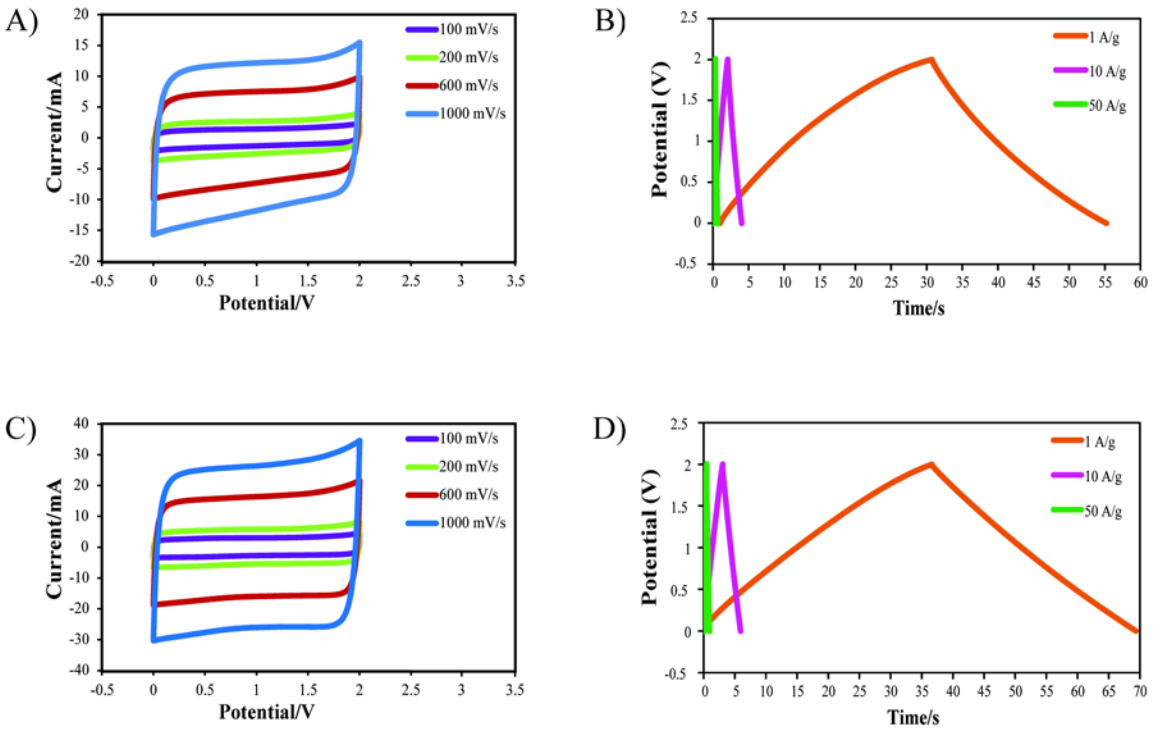

Figure 1.9 Electrochemical performance of pre-FCG (A-B) and post-FCG (C-D) supercapacitor devices. A) and C) Cyclic voltammetry of pre-FCG and post-FCG at scan rates of 100, 200, 600, and 1000 mV/s. The nearly rectangular shape indicates essentially pure capacitive charging through electrochemical double layers. B) and D) Constant current charge-discharge curves of pre-FCG and post-FCG at 1, 10, and 50 A/g_{FCG}.

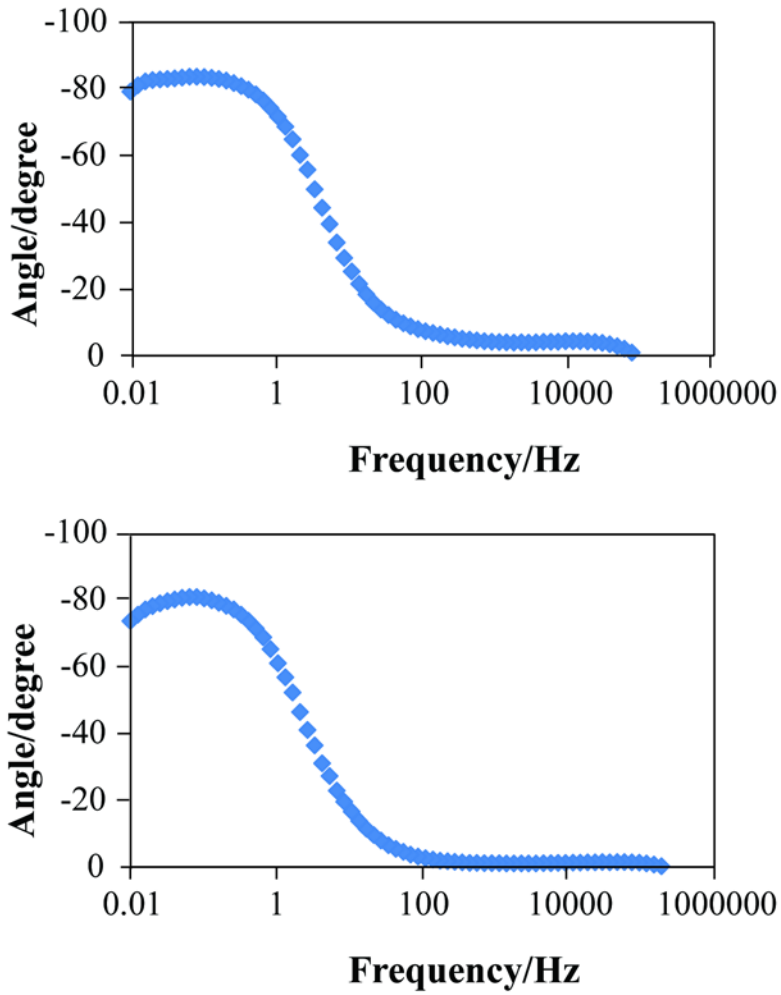

Figure 1.10 Bode plot of pre-FCG (top) and post-FCG (bottom) coin cell devices measured from 1 MHz to 10 mHz at open circuit potential. The time constant is taken from the -45° frequency, where the device exhibits 50% capacitive and 50% resistive characteristics.

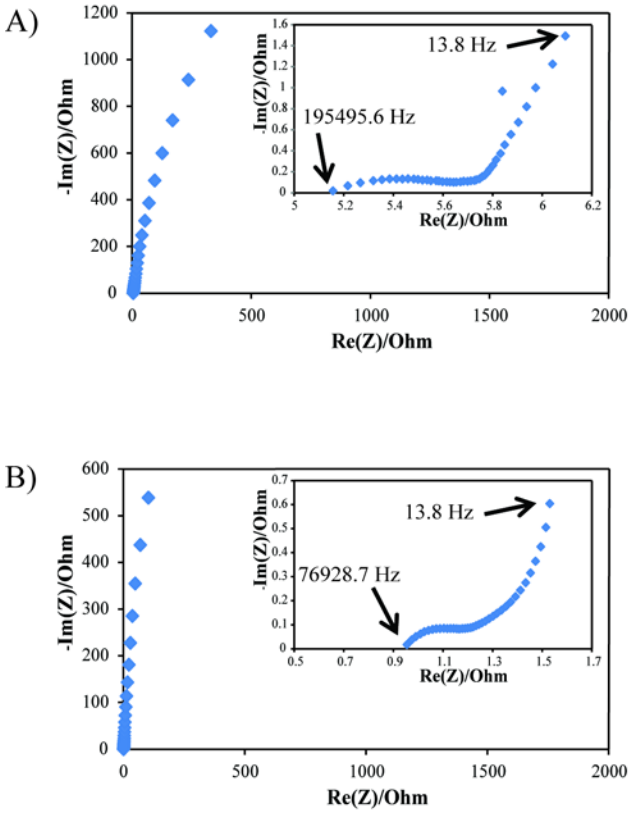

Figure 1.11 Electrochemical impedance spectroscopy: a Nyquist plot of A) pre-FCG and B) post-FCG devices. The insets expand the high frequency region.

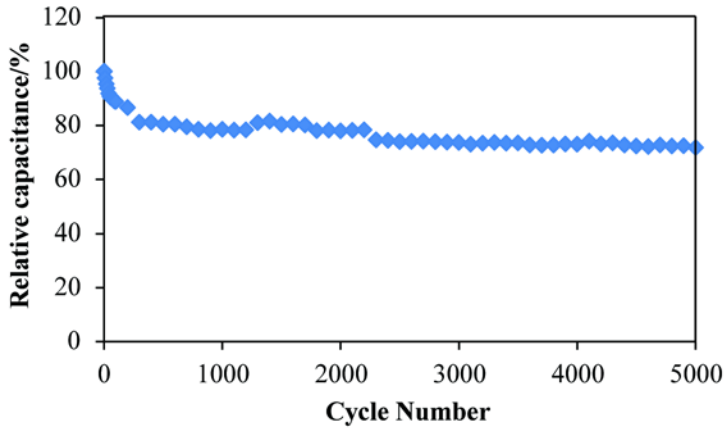

Figure 1.12 Constant current charge-discharge cycling at a current density of 1 A/g.

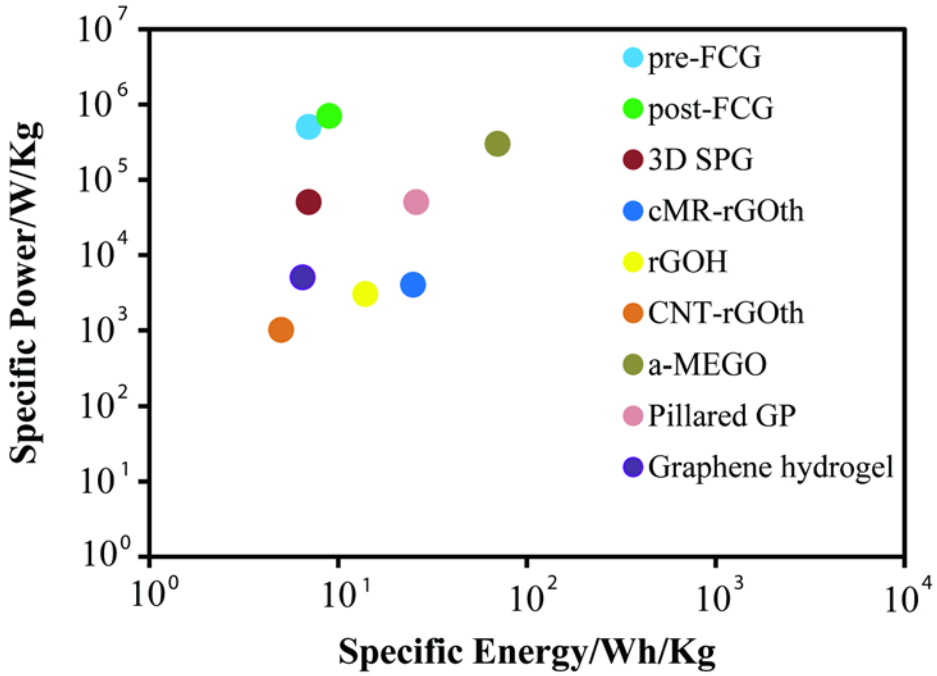

Figure 1.13 Ragone plot illustrating the high specific power of pre-FCG and post-FCG as compared to other state-of-the-art graphene-based supercapacitors.

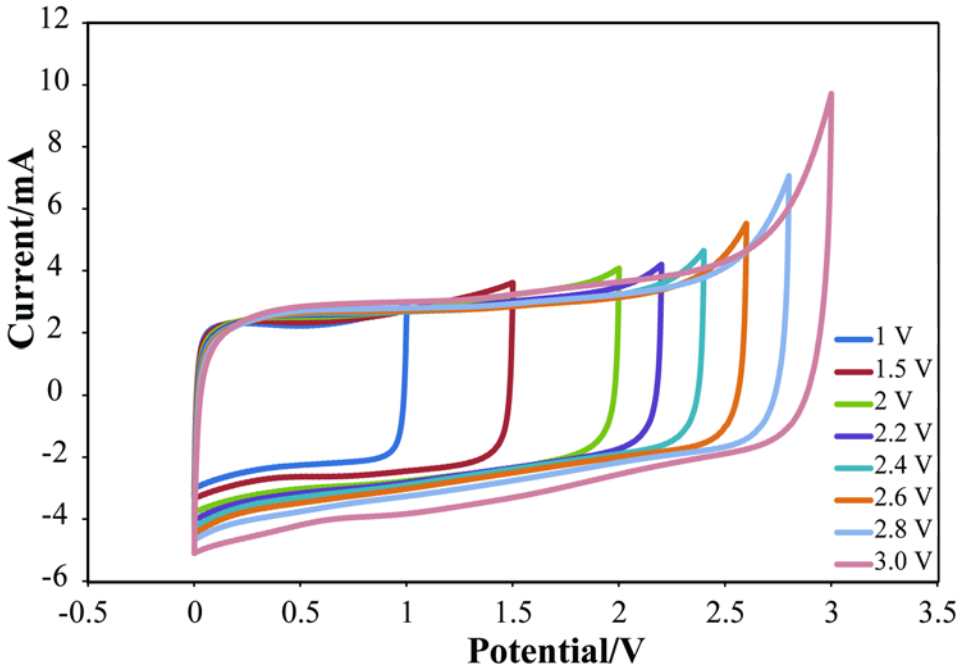

Figure 1.14 Cyclic voltammetry of FCG devices cycled at 100 mV/s from 1.0 V up to 3.0 V to determine the stable operating voltage. Based on these curves, an operating voltage of 2.0 V was selected.

1.6 References

1. BCC Research, Supercapacitors: Technology Developments and Global Markets, http://www.bccresearch.com/market-research/energy-and-resources/supercapacitors-tech-markets-egy068a.html, accessed: Feburary 2014.
2. M. V. Kiamahalleh, S. H. S. Zein, in *Nanostructured Ceramic Oxides for Supercapacitor Applications* (Eds: A. Balakrishnan, K. R. V. Subramanian), CRC Press, Florida, USA **2014**, Ch. 6.
3. Transparency Market Research, Ultracapacitors Market - Global Industry Analysis, Size, Share, Growth,Trends, and Forecast, 2013 - 2019. http://www.transparencymarketresearch.com/capacitors-market.html, accessed: Feburary 2014.
4. A. Chu, P. Braatz, *J. Power Sources.* **2002**, 112, 236.
5. P. Harrop (*IDTechEx)*, Why ultracapacitors maintain 30% market growth, http://www.electricvehiclesresearch.com/articles/why-ultracapacitors-maintain-30-market-growth-00004825.asp?sessionid=1, accessed Feburary 2014.
6. A. G. Pandolfo, A. F. Hollenkamp, *J. Power Sources.* **2006**, 157, 11.
7. J.-S. Lee, S.-I. Kim, J.-C. Yoon, J.-H. Jang, *ACS Nano.* **2013**, 7, 6047.
8. A. Izadi-Najafabadi, T. Yamada, D. N. Futaba, M. Yudasaka, H. Takagi, H. Hatori, S. Iijima, K. Hata, *ACS Nano.* **2011**, 5, 811.
9. S. Potter, M. Bayer, D. Davis, A. Born, D. McCormick, L. Dorazio, P. Patel, Space solar power satellite alternatives and architectures, *AIAA Aerospace Sciences Meeting*. **2009**.

10. C. R. Cabrera, F. Miranda, Advanced Nanomaterials for Aerospace Applications, *CRC Press*. **2014**.

11. B. Lanning, D. Martin, Survey of current and next generation space power technologies, *Defense Technical Information Center*. **2006**.

12. K. Krishen, *Acta Astronautica.* **2008**, 63, 324.

13. M. D. Stoller, S. Park, Y. Zhu, J. An, R. S. Ruoff, *Nano Lett.* **2008**, 8, 3498.

14. J. Yan, Q. Wang, T. Wei, Z. Fan, *Adv. Energy Mater.* **2014**, 4, 1300816.

15. D. Li, M. B. Muller, S. Gilje, R. B. Kaner, G. G. Wallace, *Nat. nanotechnol.* **2008**, 3, 101.

16. I. K. Moon, J. Lee, R. S. Ruoff, H. Lee, *Nat. Commun.* **2010**, 1, 73.

17. R. Chandrasekaran, Y. Soneda, J. Yamashita, M. Kodama, H. Hatori, *J Solid State Electrochem.* **2008**, 12, 1349.

18. Y. Zhu, S. Murali, W. Cai, X. Li, J. W. Suk, J. R. Potts, R. S. Ruoff, *Adv. Mater.* ***2010,*** *22, 3906.*

19. J. H. Lee, N. Park, B. G. Kim, D. S. Jung, K. Im, J. Hur, J. W. Choi, *ACS Nano.* **2013**, 7, 9366.

20. Y. Xu, H. Bai, G. Lu, C. Li, G. Shi, *J. Am. Chem. Soc.* **2008**, 130, 5856.

21. J. Luo, H. D. Jang, J. Huang, *ACS Nano.* **2013**, 7, 1464.

22. T. Kim, G. Jung, S. Yoo, K. S. Suh, R. S. Ruoff, *ACS Nano.* **2013**, 7, 6899.

23. V. C. Tung, M.J. Allen, Y. Yang, R. B. Kaner, R. B, *Nat. nanotechnol.* **2009**, 4, 25.

24. H.-J. Shin, K. K. Kim, A. Benayad, S.-M. Yoon, H. K. Park, I.-S. Jung, M. H. Jin, H.-K. Jeong, J. M. Kim, J.-Y. Choi, Y. H. Lee, *Adv. Funct. Mater.* ***2009****, 19, 1987.*

25. S. Stankovich, D. A. Dikin, R. D. Piner, K. A. Kohlhaas, A. Kleinhammes, Y. Jia, Y. Wu, S. T. Nguyen, R. S. Ruoff, *Carbon.* **2007**, 45, 1558.

26. Z. Jin, J. R. Lomeda, B. K. Price, W. Lu, Y. Zhu, J. M. Tour, *Chem. Mater.* **2009**, 21, 3045.

27. I. Jung, D. A. Field, N. J. Clark, Y. Zhu, D. Yang, R. D. Piner, S. Stankovich, D. A. Dikin, H. Geisler, C. A. Ventrice, R. S. Ruoff, *J. Phys. Chem. C.* **2009**, 113, 18480.

28. Y. Shao, J. Wang, M. Engelhard, C. Wang, Y. Lin, *J. Mater. Chem.* **2010**, 20, 743.

29. S. Gilje, S. Dubin, A. Badakhshan, J. Farrar, S. A. Danczyk, R. B. Kaner, *Adv. Mater.* **2010**, 22, 419.

30. M. F. El-Kady, V. Strong, S. Dubin, R. B. Kaner, *Science.* **2012**, 335, 1326.

31. A. J. Bard, L. R. Faulkner, *Electrochemical Methods: Fundamentals and Applications*, John Wiley & Sons, Inc., New York, USA **2001**.

32. C. Péan, C. Merlet, B. Rotenberg, P. A. Madden, P.-L. Taberna, B. Daffos, M. Salanne, P. Simon, *ACS Nano.* **2014**, 8, 1576.

33. L. L. Zhang, X. S. Zhao, *Chem. Soc. Rev.* **2009**, 38, 2520.

34. M. Zhi, C. Xiang, J. Li, M. Li, N. Wu, *Nanoscale.* **2013**, 5, 72.

35. E. Frackowiak, F. Béguin, *Carbon.* **2001**, 39, 937.

36. A. Schneuwly, R. Gallay, PCIM, *Rossens, Switzerland (***2000**).

37. Z. Xu, Z. Li, C. M. B. Holt, X. Tan, H. Wang, B. S. Amirkhiz, T. Stephenson, D. Mitlin, *J. Phys. Chem. Lett.* **2012**, 3, 2928.

38. Y. Xu, Z. Lin, X. Huang, Y. Liu, Y. Huang, X. Duan, *ACS Nano.* **2013**, 7, 4042.

39. Y. Zhu, S. Murali, M. D. Stoller, K. J. Ganesh, W. Cai, P. J. Ferreira, A. Pirkle, R. M. Wallace, K. A. Cychosz, M. Thommes, D. Su, E. A. Stach, R. S. Ruoff, *Science* **2011**, 332, 1537.

40. G. Wang, X. Sun, F. Lu, H. Sun, M. Yu, W. Jiang, C. Liu, J. Lian, *Small* **2012**, 8, 452.

41. J. H. Lee, N. Park, B. G. Kim, D. S. Jung, K. Im, J. Hur, J. W. Choi, *ACS Nano.* **2013**, 7, 9366.

42. A. Burke, *Electrochim. Acta* **2007**, 53, 1083.

43. Z. Li, L. Zhang, B. S. Amirkhiz, X. Tan, Z. Xu, H. Wang, B. C. Olsen, C. M. B. Holt, D. Mitlin, *Adv. Energy Mater.* **2012**, 2, 431.

44. A. Hammar, P. Venet, R. Lallemand, G. Coquery, G. Rojat, *IEEE Ind. Electron. Mag.* **2010**, 57, 3972.

45. D. R. Dreyer, S. Park, C. W. Bielawski, R. S. Ruoff, *Chem. Soc. Rev.* **2010**, 39, 228.

46. D. Li, M. B. Muller, S. Gilje, R. B. Kaner, G. G. Wallace, *Nat. Nanotechnol.* **2008**, 3, 101.

Chapter 2: Design for Specific Flash Converted Graphene Supercapacitor Performance Properties by Reducing the Amount of Oxygen Impurities

Abstract

Different energy and power specifications are needed for different applications. Thus, many different types of electrode materials with different unique energy storage advantages have been synthesized. The charge storage mechanism for an electric double layer capacitor is through migration of charges on the active material's surface. Pseudocapacitors, on the other hand, have Faradaic components that allow additional energy storage by a charge transfer mechanism. Carbon-based supercapacitors, like graphene, are based on electric double layer charge storage, and have unique advantages such as high power. Oxygen is seen as a redox impurity in these double layer systems. The oxygen impurities in flash converted graphene supercapacitor electrodes are shown to be tuned via a post flash H_2 annealing process at various temperatures. To investigate the role of oxygen in flash converted graphene electrodes, the electrochemical performance and capacitive behaviors of the annealed flash converted graphene electrodes are compared. Annealing the flash converted graphene electrodes at 1000° C gives the lowest oxygen content of 1.0%. The 1000 °C annealed flash converted graphene electrode also gave the most ideal electric double layer behavior with higher power ($7x10^5$ W/kg), rate capability (639 A/g), and frequency response ($1.7x10^{-2}$ s) as compared to flash converted graphene annealed at 800, 600, 400, and 200 °C. Furthermore, the flash converted graphene electrode annealed at 1000 °C shows a capacitance retention of 86.7% after 10,000 cycles, which is nearly a 10%

improvement compared to that of flash converted graphene made at room temperature. The improvements in flash converted graphene supercapacitors via reduction of oxygen impurities provides a powerful tool for selectively designing the capacitance, energy, power, frequency response, cycle stability, and other targeted electrochemical properties of supercapacitors for use in specific applications.

2.1 Introduction

To be able to design a supercapacitor to serve a particular application of interest, such as portable electronics,[1,2] medical devices,[1,3] cold start of trucks,[4-6] space applications,[3,7,8] maintaining power networks and load leveling for the grid,[9-14] memory back-up systems,[9] transportation such as buses and low-emission electric vehicles,[1,2,15] where each application has different energy specifications; i.e. portability, length of storage, minimum or maximum power requirements, performance under high rate, fast response to charge-discharge, and/or energy minimums[16-18] is the pinnacle of research. Being able to design and tune a supercapacitor to fit a specific application may soon become a reality. In order to design and tune a supercapacitor, it is important to understand the electrode materials, their behavior and properties, and variables that can affect the electrochemical performance. One variable that can affect a supercapacitor's electrochemical behavior and performance is the chemical makeup of the electrode. For example, if a supercapacitor electrode is composed of carbon such as graphene, then its charge storage mechanism is through electric double layer (EDL) formation, but if the electrode material consists of redox active materials such as metal oxides or oxygen functional groups, then the charge storage mechanism includes a Faradaic component in addition to the double layer

capacitance[19-21] (Figure 2.1). Most of the known carbon electrodes have a significant amount of oxygen impurities due to their synthesis methods. For example, Kosynkin et al. reports on unzipping carbon nanotubes and subsequent hydrazine (N_2H_4) reduction resulting in 16.1% oxygen,[22] Stankovich et al. reported that reduction of graphene oxide nanoplatelets using hydrazine hydrate at 100 °C for 24 hours gave 25% oxygen remaining.[23] Another case of chemically derived graphene by Bagri et al. shows that approximately 20% oxygen remains after chemical reduction of graphene oxide.[24] Mattevi et al. obtained 8% oxygen after thermal conversion of graphene oxide to graphene at 450 °C.[25] Murugan et al. achieved 8.3% oxygen by using microwave-solvothermal synthesis of graphene from graphene oxide,[26]. 10% oxygen was achieved by Fan et al. by using an aluminum powder as the reagent.[27,28] Furthermore, theoretical models show that the reduction of oxygen in graphene oxide below 6.25% is difficult due to the binding of hydroxyl groups.[29] Many of the synthesis methods of graphene materials involve graphene oxide as the precursor, where graphene oxide is made of graphene with oxygen functional groups on the basal and edge planes of the graphene sheets (Figure 2.2). The residual oxygen impurities are from the incomplete reduction of oxygen. This study investigates the role of oxygen impurities in post-FCG in terms of its electrochemical behaviors such as capacitance, energy, power, rate capability, frequency response, time response, resistance, cycle life, and electric double layer behavior. Thus, different electrochemical properties can be enhanced with even slight variations on the amount of oxygen in the electrode material.

Oxygen is known to be a contributor to pseudocapacitance through redox reactions because it is an electro-active species. Oxygen is known to be a highly reactive oxidizing agent,

as it has two lone pairs of electrons making it highly electronegative.[30] Oxygen, in the form of hydroxyls and carboxylates are proposed to undergo a two-electron transfer, where the specific mechanism depends on the electrode's structure and surface materials. Oxygen on edge sites of graphene are shown to be more reactive than the functionalities on the basal plane.[31-33] Metal oxides such as RuO_2, Co_3O_4, NiO, or MnO_2 undergo redox reactions by electron transfer between metal and oxygen with electrolyte ions. Many carbon/polymer composites, such as polyaniline, also show pseudocapacitance, where the conjugated polymers generally contain redox active oxygen or nitrogen functional groups.[18,34] Furthermore, oxygen functionalities in the form of quinones are known to undergo redox reactions and are deemed as basic functionalities which will react with cations.[35-38] The presence of scarce amounts of oxygen functional groups in many different types of supercapacitor active materials, such as activated carbon, graphene, and carbon nanotubes, are seen to improve energy, but hinder power. These oxygen groups are also seen to lower the stability of supercapacitors during prolonged cycling.[18] Reducing the oxygen groups in the active material increases the number of sp^2 carbons, thus delocalizing π bonds and thereby improving charge transport. The conjugation in the graphene sheets then becomes connected and extended over larger areas forming a conducting network.[25, 31] In a pure electric double layer capacitor, the redox components can potentially jeopardize desired electrochemical properties required for a targeted application.

Herein, the effects of oxygen impurities on the electrochemical performance of flash converted graphene (FCG) supercapacitors are reported. Improvements in FCG supercapacitors via incrementally reducing oxygen impurities are demonstrated. The controlled reduction of

oxygen impurities provides a powerful tool for selectively designing supercapacitors for specific applications. The post-FCG electrodes are used in this study as a model system because of their good electrochemical performance, tunable oxygen content, and their graphene-based active material, which enables good electric double layer capacitance.

In this study the role of oxygen impurities in FCG supercapacitors are investigated. The FCG electrodes were annealed under 11 sccm of 5% H_2 in Ar for 4 hours in a furnace and then assembled into coin cells for testing. This annealing process prevents the disturbance of the 3D corrugated morphology and ensures that no unwanted impurities are added to the FCG materials. A series of temperatures were used in the annealing experiments for comparison, where each set of post-FCG electrode was subject to 11 sccms of 5% H_2 in Ar at different annealing temperatures. The annealing temperatures are 200 °C (200-post-FCG), 400 °C (400-post-FCG), 600 °C (600-post-FCG), 800 °C (800-post-FCG), and 1000 °C (1000-post-FCG). All of the annealed post-FCG electrodes were compared to post-FCG electrodes with no annealing. 1000-post-FCG gave the lowest oxygen content of 1.0%, the lowest capacitance of 37 $F/g_{/electrode}$ (0.10 $F/cm^3_{/device}$), but the highest operating rate capability of 639 A/g, the best power of $7x10^5$ W/kg, the fastest frequency response of $1.7x10^{-2}$ s, shortest time response of 0.08 s, and longest cycle life (88.2% at 5000 cycles; 86.7% at 10,000 cycles) compared to non-annealed post-FCG (14.4% oxygen).

2.2 Results and Discussion

2.2.1 Effect of Post Flash H_2 Annealing Temperature on Oxygen in post-FCG

The post flash H_2 annealing process reduces the amount of oxygen impurities in the post-FCG electrode materials. The extent of the decrease in oxygen depends on the temperature used in the annealing process. A higher annealing temperature gives a more reduced post-FCG electrode. The oxygen content of post-FCG without the post flash H_2 annealing process is 14.4% as shown previously. A maximum of 1000 °C was used in the annealing experiments, which produced a FCG electrode material with only 1.0% oxygen impurity. Oxygen contents of the FCG electrodes with annealing temperatures in between 200-1000 °C range from 13.5-1.0% as shown in Table 2.1. Oxygen amounts were obtained using X-ray photoelectron spectroscopy (XPS). Oxygen was found to be in the form of oxygen containing functional groups (C-OH, C-O-C, C=O, and COOH) (Figure 2.3). No other compounds were detected in appreciable amounts for each of the FCG samples.

The linear dependence between the amount of oxygen in post-FCG and the annealing temperature suggests an incremental loss of oxygen from post-FCG material (Figure 2.4). From extrapolation of the linear curve of annealing temperature and oxygen amount, an annealing temperature of 1073 °C would result in 0% oxygen in the FCG samples. At this temperature all the residual oxygen functional groups would be removed. During the annealing process oxygen is eliminated from the FCG material and the proposed by-products of the conversion of graphene oxide to graphene is H_2O vapor and CO_2 gas.[25, 31] The incremental change in oxygen content

with different annealing temperatures shows that this annealing process serves as a tool for the design and tuning of post-FCG material with varying amounts of redox active oxygen species.

Residual oxygen in FCG is found in the form of oxygen functional groups such as C-OH, C-O-C, C=O, and COOH and originate from the oxygen functional groups in the graphene oxide (GO) precursor. The amount of each oxygen functional group in the FCG samples varies. However, all of the annealed FCG samples have the largest amount of C-OH (54.4-71.7%). C-O-C was seen as the second most predominant oxygen functional group (20.0-28.3%), while the amount of C=O and COOH (0-0.1%) were negligible. Furthermore, all of the oxygen functional groups decreased with increasing post H_2 annealing temperature. Between 200-post-FCG and 1000-post-FCG the C-OH content decreased from 18.2% to 4.9%, C-O-C decreased from 6.7% to 1.9%, C=O decreased from 2.5% to 0%, and COOH decreased from 2.5% to 0%. Thus, essentially all C=O and COOH was eliminated from FCG after the post H_2 annealing process at 1000 °C. In 1000-post-FCG, 4.9% C-OH and 1.9% C-O-C was present after annealing FCG at 1000 °C. Thus, for 1000-post-FCG the redox components are most likely from C-OH and C-O-C. Profiling the oxygen functional groups in the annealed FCG samples gives insight as to which types of oxygen functional groups are contributors to redox processes.

Raman spectra for the annealed post-FCG samples were collected and compared in Figure 2.5. The peaks in Raman spectroscopy represent vibrational, rotational, and other low-frequency modes of a material. For graphitic materials, such as graphite and graphene oxide, the peaks of interest are the G band arising from sp^2 bond stretching of its rings and chains, the D band corresponding to breathing modes of all sp^2 atoms in the rings, and the 2D band which is an

overtone of the D band and thought to arise from the zero order phonons at the zero boundary.[39-41] More specifically for graphite, the G band is a result of the high frequency E2g Raman allowed optical phonon and the D band, which emerges for nanocrystalline graphite, resulting from the A1g breathing mode at the Brillouin Zone K boundary.[40] In carbon materials, the G peak usually emerges at around 1560 cm^{-1} and the D peak emerges around 1360 cm^{-1}.[41] In graphite, the G peak is found at around 1580 cm^{-1}, while the D peak is found at around 1350 cm^{-1}.[42] A change from graphene oxide materials to graphene materials has been reported to induce a shift in the G peak from 1609 cm^{-1} to 1589 cm^{-1}.[43] In the annealed post-FCG samples, both the G and D peaks are observed for all annealing temperatures. The G peaks ranges between 1594 cm^{-1} for 200-post-FCG and 1579 cm^{-1} for 1000-post-FCG. A sequential shift in G peaks from 1594 cm^{-1} to 1579 cm^{-1} with increasing temperature of the post anneal process is seen and suggests a shift in characteristics from a graphene oxide material to a graphene-like material due to the loss of oxygen. The D peak is found around 1352 cm^{-1} for the post annealed FCG samples. Also, the graphitic 2D peak, which is present around 2700 cm^{-1}, is seen most prominently for 1000-post-FCG sample (Figure 2.5), further supporting the reduction of oxygen in the FCG samples with increased post annealing temperature. The ratio of the intensity of the D to G band (I_D/I_G) also sheds light on the nature of the graphene material, for instance, in predicting the presence of defects or the size of in-plane sp^2 regions. This ratio is known to be inversely proportional to the size of the crystalline grains. The I_D/I_G ratio value for graphene oxide is reported to be around 0.99.[43] For the annealed FCG samples, the I_D/I_G ratio sequentially decreases with incremental increase in annealing temperature from 200° to 800 °C, but then sharply increases to 1.1 for

1000-post-FCG. 200-post-FCG, 400-post-FCG, 600-post-FCG, 800-post-FCG, and 1000-post-FCG have I_D/I_G ratios of 0.90, 0.86, 0.79, 0.78, and 1.1, respectively.

2.2.2 Characterization: 3D Morphology and Composition

The morphology and composition of 200-post-FCG, 400-post-FCG, 600-post-FCG, 800-post-FCG, and 1000-post-FCG as shown from SEM and PXRD are all similar to that of post-FCG. The 3D corrugated morphology of post-FCG is preserved in the post flash H_2 annealing processes at all temperatures (200-1000 °C). The 3D corrugated morphology is indicated by the presence of a fractal graphene framework surrounding voids as shown from the scanning electron microscopy (SEM) images in Figure 2.6. The 3D corrugated morphology is crucial to the accessibility and migration of electrolyte ions to the surfaces of the FCG electrode material for maximizing double layer capacitance. Also, there were no phase changes detected from X-ray diffraction (XRD) patterns after annealing, thus indicating that the composition of the post flash H_2 annealed FCG electrodes was preserved (Figure 2.7).

2.2.3 Role of Oxygen Impurities on Electrochemical Performance of post-FCG

From the electrochemical results, it is seen that oxygen impurities in post-FCG electrodes significantly affect several properties of electrochemical performance and capacitive behavior. A decrease in oxygen impurities in post-FCG electrode material results in a FCG device with lower resistance giving better performance in terms of power, frequency response, and rate capability. Also, because there is less resistance and more electric double layer behavior, the voltage drop and equivalent series resistance (ESR) are lowered. The cycle life is also affected by the oxygen impurities, where lowering the oxygen amount leads to an increase in cycle stability. The only

downside of decreasing oxygen is that the capacitance and specific energy also decrease (Table 2.2). The reason for the decrease in capacitance and energy with decreasing oxygen is that the Faradaic component of the FCG electrodes is being reduced. Thus, lowering the oxygen impurities in FCG gives a more ideal double layer behavior.

The ideality of the double layer behavior of the FCG samples increases in this order: post-FCG, 200-post-FCG, 400-post-FCG, 600-post-FCG, 800-post-FCG, 1000-post-FCG. Post-FCG, with the highest oxygen content, shows the least rectangular shape and most resistive cyclic voltammogram (CV). The 1000-post-FCG electrode has the lowest amount of oxygen and shows the most rectangular shape and least resistive CV (Figure 2.8). This trend is seen at both low scan rates of 100 mV/s as well as at high scan rates of 10,000 mV/s. Furthermore, the Nyquist plots of the FCG samples show a similar trend in ideality of double layer behavior. More specifically, the Nyquist plot can give valuable information on not only the ideality of the supercapacitor, but also on details such as the types of resistances and the origins of resistance and capacitance of an electrochemical device.[21] The ESR trends for the FCG samples also supports the observation that lower oxygen content gives a more ideal supercapacitor behavior. The ESR for the samples is as follows: 1.32 ohm for post-FCG, 1.17 ohm for 200-post-FCG, 1.39 for 400-post-FCG, 0.78 ohm for 600-post-FCG, 0.68 ohm for 800-post-FCG, and 0.57 ohm for 1000-post-FCG. The lowest ESR is seen for the 1000-post-FCG supercapacitor electrode. From the Nyquist plot we can also investigate the types of resistance and reactions occurring in a supercapacitor device. The presence of a semi-circle in the Nyquist plot indicates the presence of charge transfer resistance (R_{ct}) from Faradaic reactions (such as oxides), or contact resistance in

the case of a pure double layer system. The semi-circle (R_{ct}) is most prominent for post-FCG, 200-post-FCG, 400-post-FCG, and 600-post-FCG, with no significant change between those samples. However, for the 800-post-FCG supercapacitor, the semi-circle (R_{ct}) is drastically reduced in size. The semi-circle (R_{ct}) disappears in the 1000-post-FCG device (Figure 2.9). This trend of decreasing R_{ct} with decreasing amounts of oxygen indicates that the oxygen impurities provide a significant redox contribution to the FCG supercapacitors, and that we can control the amount of oxygen by simply changing the annealing temperatures in the post flash H_2 annealing process.

A Bode plot of the FCG samples further elucidates the findings on the effects of oxygen impurities on the ideality of double layer behavior. A phase shift between voltage and current of -90°, where current leads voltage, indicates the most ideal capacitive behavior. The phase shift of 1000-post-FCG reaches -86.16° and is the closest FCG sample to -90°. The phase shifts for 800-post-FCG (-84.82°), 600-post-FCG (-83.02°), 400-post-FCG (-82.38°), and 200-post-FCG (-82.03°) are sequentially farther away from -90°, and thus, farther from ideal double layer behavior. Furthermore, the frequency responses for annealed FCG samples as seen from the Bode plot are 0.08 s for 1000-post-FCG, 0.11 s for 800-post-FCG, 0.18 s for 600-post-FCG, 0.35 s for 400-post-FCG, and 0.30 s for 200-post-FCG. The frequency response is where the resistive and capacitive components are equal (-45° for a capacitor) (Figure 2.10). Similarly, the time response is a parameter used to judge the performance of a supercapacitor, it is expressed in terms of the time at which the capacitance of the device reaches 50%, and thus the faster the better. The time response of 1000-post-FCG is 1.7×10^{-2} s, 800-post-FCG is 1.9×10^{-2} s, 600-post-

FCG is $2.4x10^{-2}$ s, 400-post-FCG is $2.3x10^{-2}$ s, and 200-post-FCG is $2.3x10^{-2}$ s. The device with the best time response is 1000-post-FCG (Table 2.2). 1000-post-FCG also exhibited the lowest voltage drop ($2.7x10^{-3}$ V), and the highest specific power ($7x10^{5}$ W/kg). The specific power of the annealed FCG samples are 800-post-FCG is $5x10^{5}$ W/kg, 600-post-FCG is $4x10^{5}$ W/kg, 400-post-FCG is $2x10^{5}$ W/kg, and 200-post-FCG is $3x10^{5}$ W/kg (Table 2.2).

The rate capability of the samples were also evaluated and compared. The rate capability of a device is a measure of its ability to operate under different applied currents. A device has higher rate capability if it can operate at higher applied currents, which is important for certain applications.[21] It is also important that the device can hold an appreciable amount of charge when operating at higher currents. The rate capability at which the devices can hold 50% capacitance for 1000-post-FCG is 280 A/g, 800-post-FCG is 224 A/g, 600-post-FCG is 148 A/g, 400-post-FCG is 142 A/g, and 200-post-FCG is 112 A/g. The current density at which the devices become inoperable are 639 A/g for 1000-post-FCG, 538 A/g for 800-post-FCG, 391 A/g for 600-post-FCG, 324 A/g for 400-post-FCG, and 307 A/g for 200-post-FCG. The 1000-post-FCG electrode is operable at the highest current density among the FCG electrodes (Table 2.2 and Figure 2.11). The high rate capability corresponds to lower disruptions to the aromaticity of the graphene sheets due to a higher sp^2/sp^3 ratio.[18]

The cycle stability, which is another important measure of a supercapacitor's performance ability, was evaluated in terms of cycle life via charge-discharge experiments at 1 A/g_{FCG}. As an example, 1000-post-FCG, which exhibited the most ideal double layer behavior, highest power, highest rate capability, and lowest ESR was chosen to compare to post-FCG (not

annealed). Post-FCG as shown previously has relatively good cycle life with 71.8% capacitance retained after 5000 cycles, but 1000-post-FCG showed even higher cycle stability with 88.2% capacitance retained after 5000 cycles. Furthermore, the 1000-post-FCG supercapacitor device retained 86.7% of its capacitance after 10,000 cycles (Figure 2.12).

In terms of capacitance and specific energy, oxygen impurities are beneficial for increasing capacitance and specific energy due to their ability to undergo charge transfer reactions.[32, 33] The oxygen in FCG is originally from graphene oxide and is found in FCG in the form of oxygen containing functional groups such as C-OH, C-O-C, C=O, and COOH. Thus, 1000-post-FCG gave the lowest capacitance (37 $F/g_{electrode}$; 0.46 $F/cm^3_{electrode}$) and specific energy (5 Wh/kg) as compared to the post-FCG electrodes annealed at lower temperatures. The post-FCG electrode that was not annealed has the highest capacitance of 77 $F/g_{electrode}$; 0.98 $F/cm^3_{electrode}$ and highest specific energy of 11 Wh/kg. The capacitances of all other annealed FCG samples are 40 $F/g_{electrode}$ and 0.49 $F/cm^3_{electrode}$ for 800-post-FCG, 46 $F/g_{electrode}$ and 0.57 $F/cm^3_{electrode}$ for 600-post-FCG, and 64 $F/g_{electrode}$, 0.79 $F/cm^3_{electrode}$ for 400-post-FCG, and 62 $F/g_{electrode}$ and 0.76 $F/cm^3_{electrode}$ for 200-post-FCG. And the specific energy of 800-post-FCG is 5 Wh/kg, 600-post-FCG is 6 Wh/kg, 400-post-FCG is 9 Wh/kg, and 200-post-FCG is 9 Wh/kg. The capacitance based on the devices, which includes both the volume of the electrodes and the separator, of 1000-post-FCG is 0.10 F/cm^3_{device}, for 800-post-FCG is 0.11 F/cm^3_{device}, for 600-post-FCG is 0.13 F/cm^3_{device}, for 400-post-FCG is 0.18 F/cm^3_{device}, for 200-post-FCG is 0.17 F/cm^3_{device}, and for post-FCG is 0.21 F/cm^3_{device}. The increase in capacitance and specific energy

with an increase in oxygen impurities is attributed to the redox active properties of the oxygen functional groups in the FCG electrodes.

Thus, 1000-post-FCG had the lowest oxygen content of 1.0%, the lowest capacitance of 37 $F/g_{/electrode}$; 0.46 $F/cm^3_{/electrode}$, but the highest, rate capability, the best power of $7x10^5$ W/kg, lowest time response of $1.7x10^{-2}$ s, the lowest frequency response of 0.08 s, and the longer cycle life compared to non-annealed post-FCG (2.4 times greater). It is seen that not only a large change of 14% oxygen, but also a small change of 2.7% oxygen, can make a significant impact on the electrochemical behavior of the FCG supercapcacitor devices. This means that oxygen, in the form of oxygen functional groups, plays a significant role in contributing a Faradaic component to the system

2.3 Conclusions

This study shows that 1) oxygen impurities in FCG electrode material can be easily tuned via a post flash H_2 annealing process by varying the annealing temperature, and 2) the electrochemical performance and double layer behavior can be altered by tuning the oxygen content. Oxygen is seen to linearly decrease with increasing temperature in the annealing process, with 1000-post-FCG resulting in the lowest oxygen content of 1.0%. This reduction of oxygen impurities shows an improvement in double layer behavior as seen from cyclic voltammetry and electrochemical impedance spectroscopy. The 1000-post-FCG electrode shows higher power ($7x10^5$ W/kg), higher rate capability (639 A/g), and better frequency response ($1.7x10^{-2}$ s). The cycle life is also greatly improved; for example, 1000-post-FCG retained 88.2% capacitance after 5000 cycles and retained 86.7% capacitance after 10,000 cycles, whereas post-

FCG (not annealed; 14.4% oxygen) retained only 71.8% capacitance after 5000 cycles. It was also seen that the capacitance and specific energy is greatest for FCG electrodes with the greatest amount of oxygen because oxygen serves as a Faradaic contributor to the charge storage device. The capacitance of post-FCG is 77 $F/g_{/electrode}$, 0.98 $F/cm^3_{/electrode}$, and the capacitance of 1000-post-FCG is 37 $F/g_{/electrode}$, 0.46 $F/cm^3_{/electrode}$. The specific energy of post-FCG is 11 Wh/kg and that of 1000-post-FCG is 5 Wh/kg. Furthermore, the morphology and composition of the FCG material were preserved during the post flash H_2 annealing process. This study can be extended as a microcosm examining the role of oxygen, and provides indications of how oxygen impurities can influence the electrochemical performance properties of graphene-based electric double layer systems.

2.4 Experimental Section

2.4.1 Synthesis of post-FCG Electrodes

The post-FCG electrodes were prepared by flashing a freeze-dried foam of graphene oxide on a carbon coated aluminum foil current collector. Graphene oxide (GO) was synthesized via a modified Hummer's Method,[44,45] GO (2.6%) was coated onto current collectors and freeze-dried using a Freezone lyophilizer then flash converted using an Alien Bees B1600 flash lamp at 160 J to give post-FCG. Instead of directly assembling the post-FCG electrodes into coin cells, they were annealed at temperatures of 200, 400, 600, 800, and 1000 °C. The post-FCG electrode films were detached from the current collector for annealing and given a fresh piece of current collector prior to cell assembly.

2.4.2 FCG Post Annealing Process for Varying Oxygen Content

All annealing of post-FCG was carried out using an MTI 1200x tube furnace set to 200, 400, 600, 800, and 1000 °C for the five sets of experiments. Each set of post-FCG samples were held at the designated temperature for 4 hours under a constant flow rate of 11 sccm of 5% H_2 in Ar, and then cooled to room temperature under Ar.

2.4.3 Coin Cell Fabrication

Post-FCG, 200-post-FCG, 400-post-FCG, 600-post-FCG, 800-post-FCG, and 1000-post-FCG electrodes were assembled into CR2032 coin cells using the same method as used to make the pre-FCG and post-FCG supercapacitor coin cell devices. The FCG electrodes were 15 mm in diameter with a 17 mm diameter polypropylene separator. The electrolyte used is 1.0 M $TEABF_4$ in acetonitrile.

2.4.4 Electrochemical Measurements and Calculations

Coin cell devices of all FCG electrode samples were measured and calculated using a Biologic VMP3 potentiostat and Biologic VMP3b-10 booster. The coin cells were inserted and tested with a 4-point holder. Capacitance, energy, power, voltage drop, and ESR, were calculated from constant current curves at 1 A/g_{FCG} from 0 V to 2 V. The rate capability for each sample was calculated from constant current curves at different current densities. Cycle stability was also measured using constant current charge-discharge at $1A/g_{FCG}$ from 0 V to 2 V. Frequency response, time response, Nyquist plot, and Bode plots were obtained from electrochemical impedance data measured from 1 MHz to 10 mHz at open circuit potential.

Capacitance (C) was calculated from the applied current (i) and the slope of the discharge constant current curve (dv/dt) using Equation 2.1:

$$C = \frac{idt}{dv}$$ (Eq. 2.1)

The gravimetric and volumetric capacitances were obtained by dividing C by mass and volume, respectively. And energy is calculated using C.

$$E = \frac{1}{2}CV^2$$ (Eq. 2.2)

Where V is the operating voltage used.

The power of the FCG devices was calculated from the operating voltage and the ESR.

2.4.5 XPS Measurements and Analysis

The relative amounts of carbon and oxygen in the FCG electrode materials were measured using a Kratos AXIS Ultra DLD with a monochromatic Al Kα X-ray source X-ray photoelectron spectroscopy (XPS) operating at 10 mA and 15 kV. All data were processed using CasaXPS 2.3 software.

2.4.6 Characterization: Morphology and Composition

Morphological investigations of the post-FCG, 200-post-FCG, 400-post-FCG, 600-post-FCG, 800-post-FCG, and 1000-post-FCG samples were carried out via SEM (FEI Nova 230 Nano SEM). The PXRD patterns used to shed light on the compositional changes were collected using a Bruker D8 Discover Powder X-ray Diffractomator. Raman spectra of the post annealed FCG samples were taken using an inVia Raman (Renishaw) with a 514 nm Ar laser.

2.5 Tables and Figures

Table 2.1 Oxygen Percentages with Increasing Annealing Temperatures

FCG	Temperature (°C)	Oxygen %
Post-FCG	NA	14.4
200-post-FCG	200	13.5
400-post-FCG	400	9.6
600-post-FCG	600	6.7
800-post-FCG	800	3.7
1000-post-FCG	1000	1.0

Table 2.2 Comparison of Electrochemical Performance for Post Flash H_2 Annealed FCG Samples at Different Temperatures

FCG	F/g	F/cm^3	$F/cm^3_{/device}$	Wh/kg	W/kg	V Drop (1A/g)	ESR	Frequency Response (s)	Time Response (s)	Rate Capability (1%)
200-post-FCG	62	0.76	0.17	9	$3x10^5$	$6.7x10^{-3}$	1.17	0.30	$2.3x10^{-2}$	307
400-post-FCG	64	0.79	0.18	9	$2x10^5$	$1.4x10^{-2}$	1.39	0.35	$2.3x10^{-2}$	324
600-post-FCG	46	0.57	0.13	6	$4x10^5$	$5.6x10^{-3}$	0.78	0.18	$2.4x10^{-2}$	391
800-post-FCG	40	0.49	0.11	5	$5x10^5$	$3.6x10^{-3}$	0.68	0.11	$1.9x10^{-2}$	538
1000-post-FCG	37	0.46	0.10	5	$7x10^5$	$2.7x10^{-3}$	0.57	0.08	$1.7x10^{-2}$	639

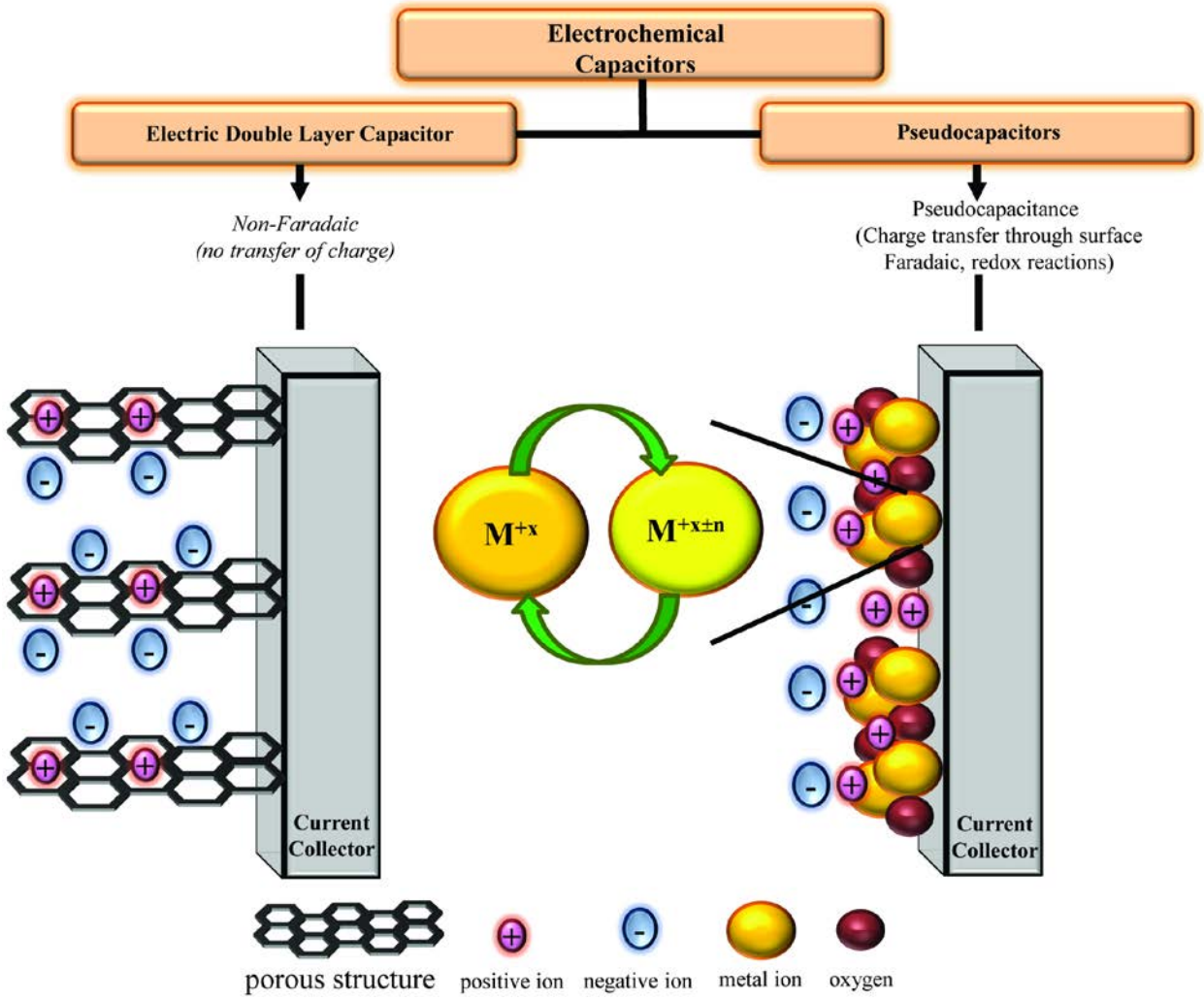

Figure 2.1 Electrochemical capacitors based on two different mechanisms. Electric double layer capacitors (left) store charge through double layer formation at the surface of the active material. Pseudocapacitors store charge through both double layer as well as redox reactions of the active material.

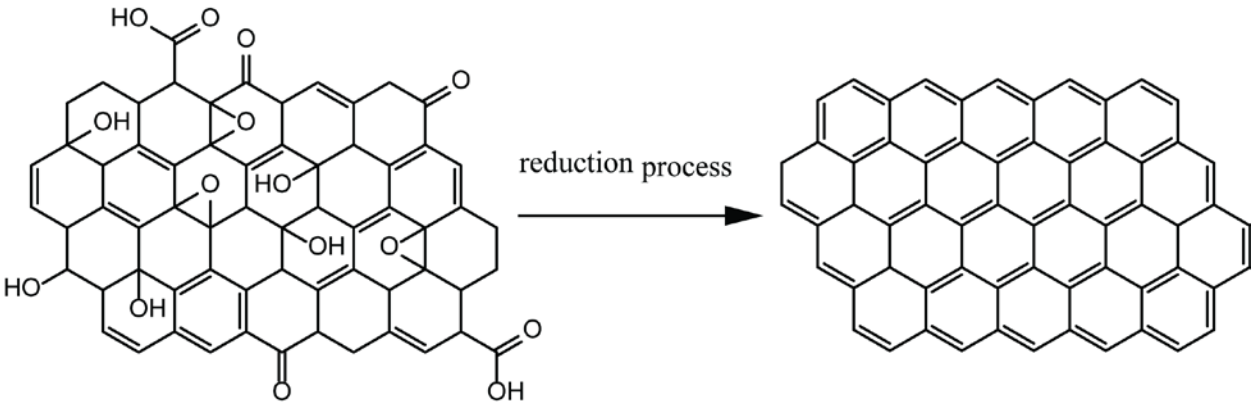

Figure 2.2 Graphene oxide (left) is composed of graphene with oxygen functional groups such as C-OH, C-O-C, C=O, and COOH. Graphene oxide is converted to a graphene material (right) after the reduction process.

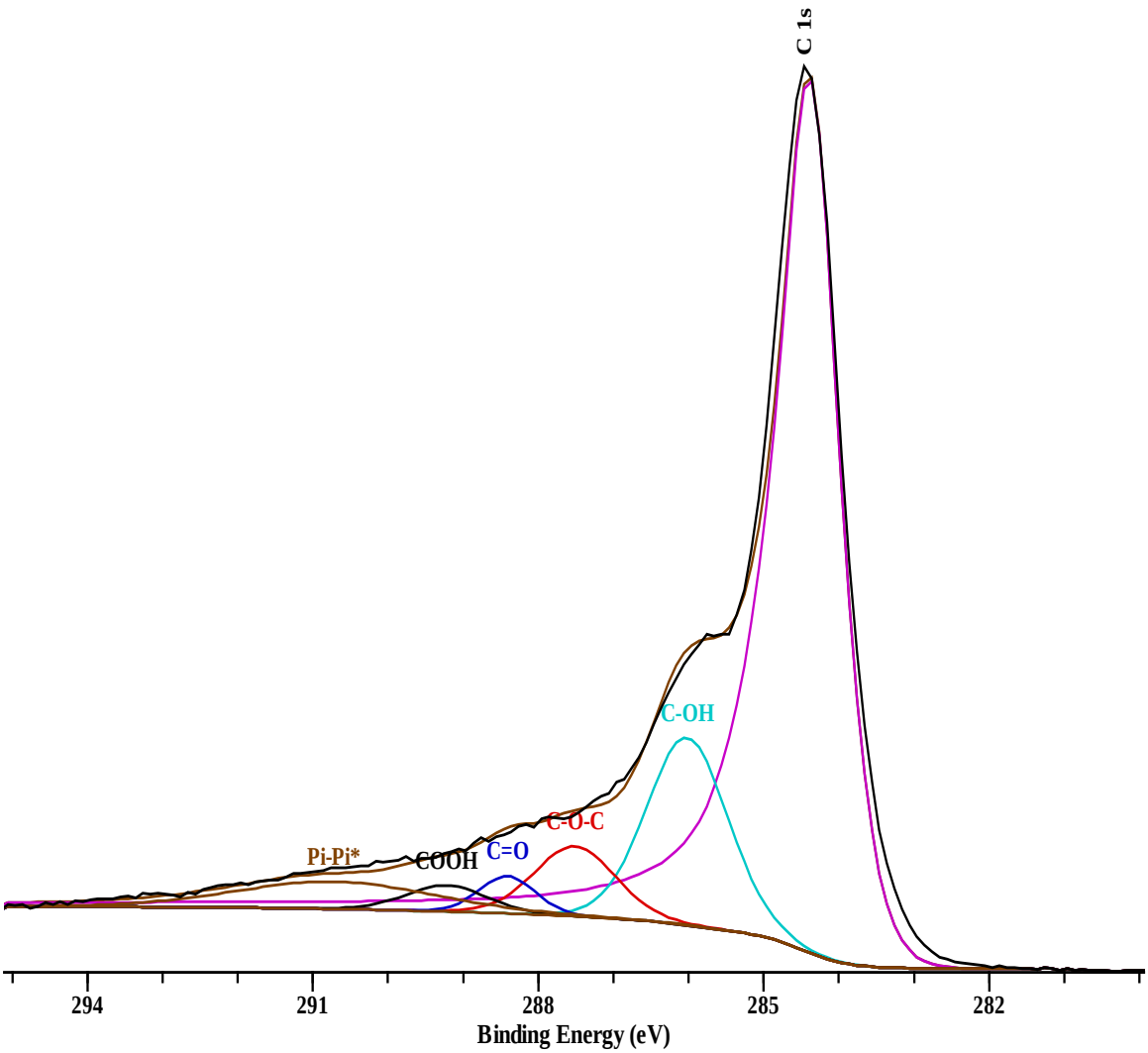

Figure 2.3 XPS of 200-post-FCG with oxygen functional groups.

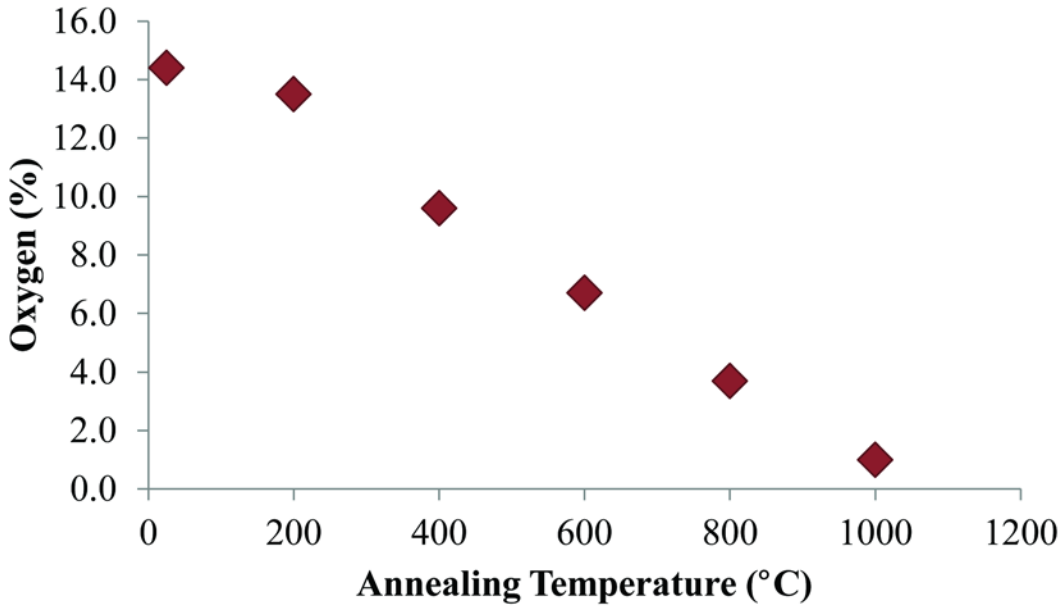

Figure 2.4 A decrease in oxygen amount is seen with increasing the post flash H_2 annealing temperature.

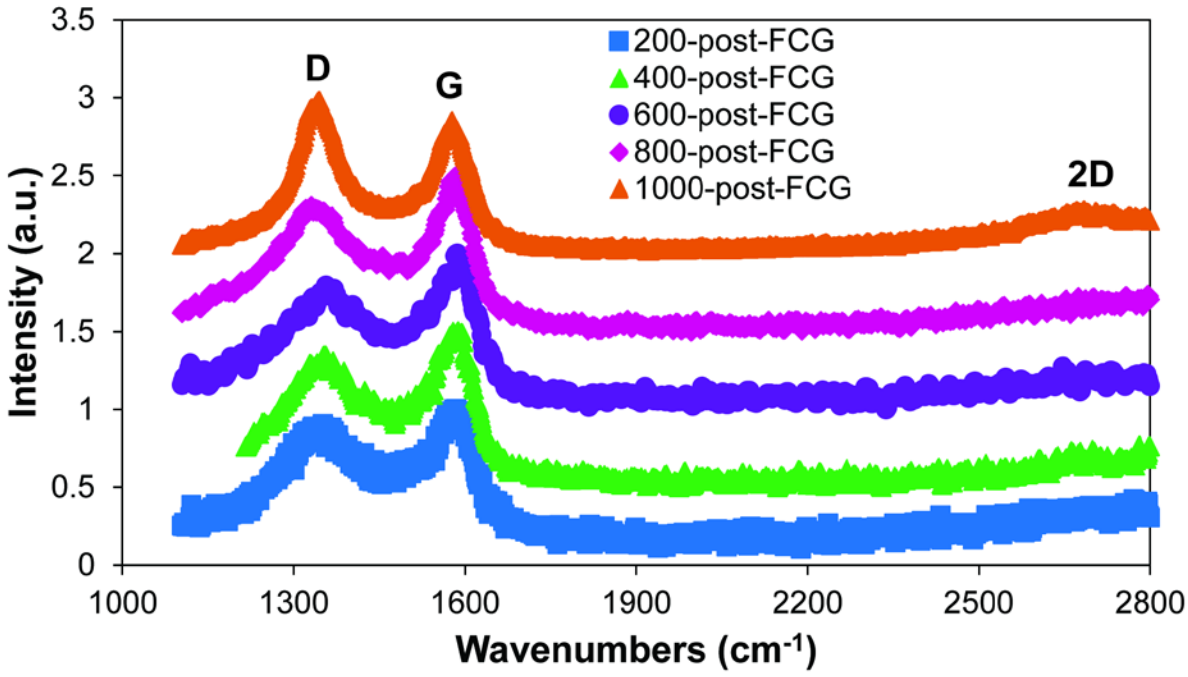

Figure 2.5 Raman spectra of post annealed FCG samples showing G peak shift and emergence of 2D peak with higher annealing temperatures.

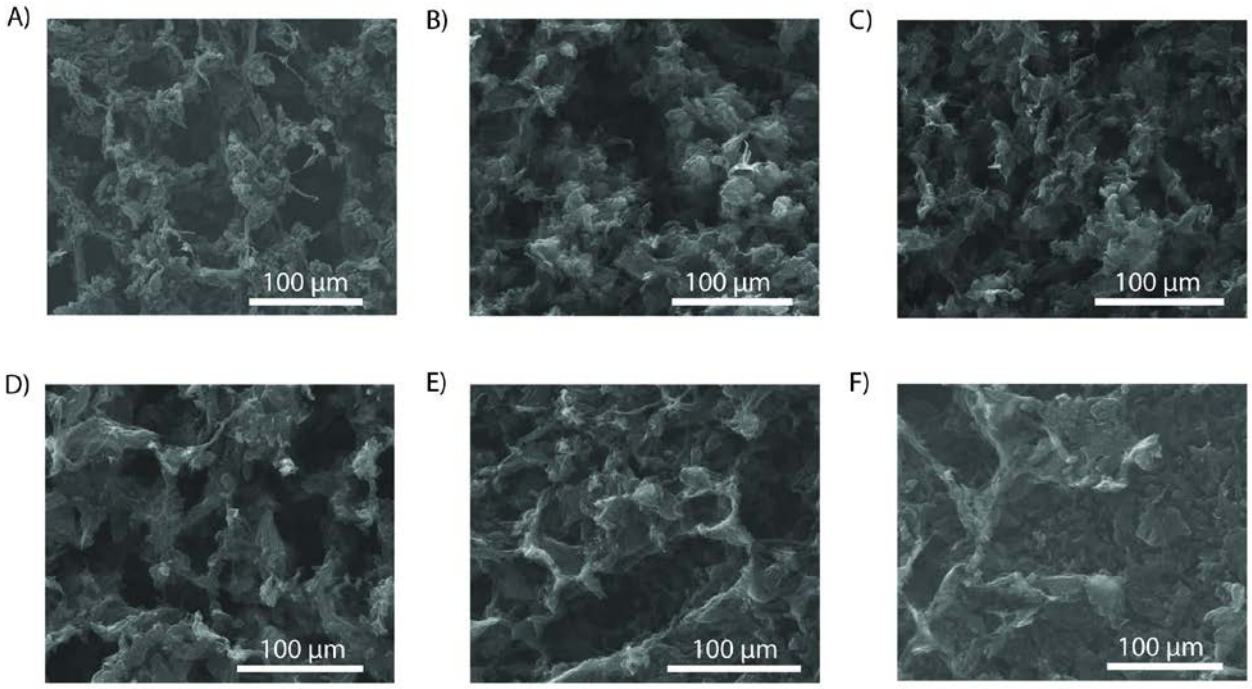

Figure 2.6 SEM images showing the morphology of FCG samples; A) post-FCG, B) 200-post-FCG, C) 400-post-FCG, D) 600-post-FCG, E) 800-post-FCG, F) 1000-post-FCG.

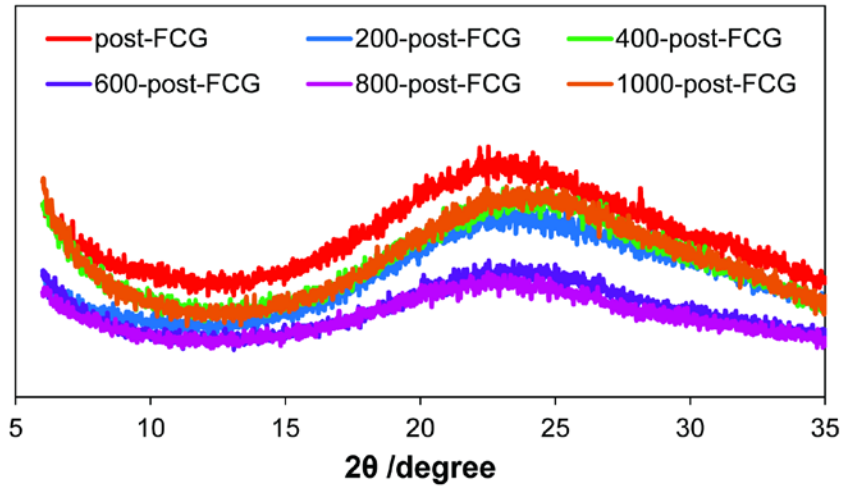

Figure 2.7 X-ray diffraction patterns of post-FCG and annealed post-FCG electrodes.

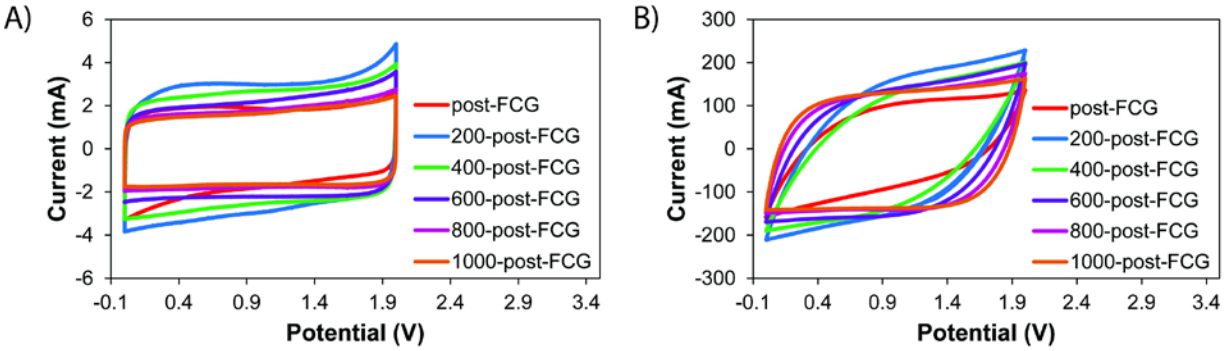

Figure 2.8 Cyclic voltammogram of FCG samples (24-1000 °C post flash H_2 anneal); A) at 100 mV/s and B) at 10,000 mV/s. More ideal capacitive behavior is seen for higher temperature annealed FCG electrodes (lower oxygen amount).

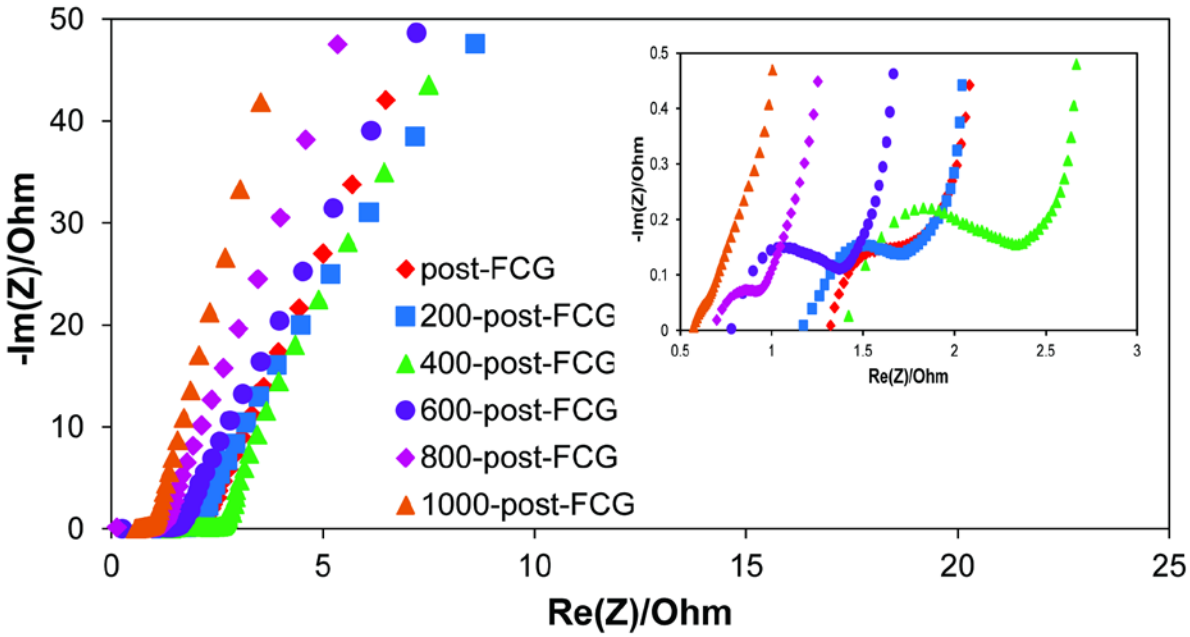

Figure 2.9 Nyquist plot of annealed FCG samples compared to a post-FCG sample. The inset expands the high frequency region.

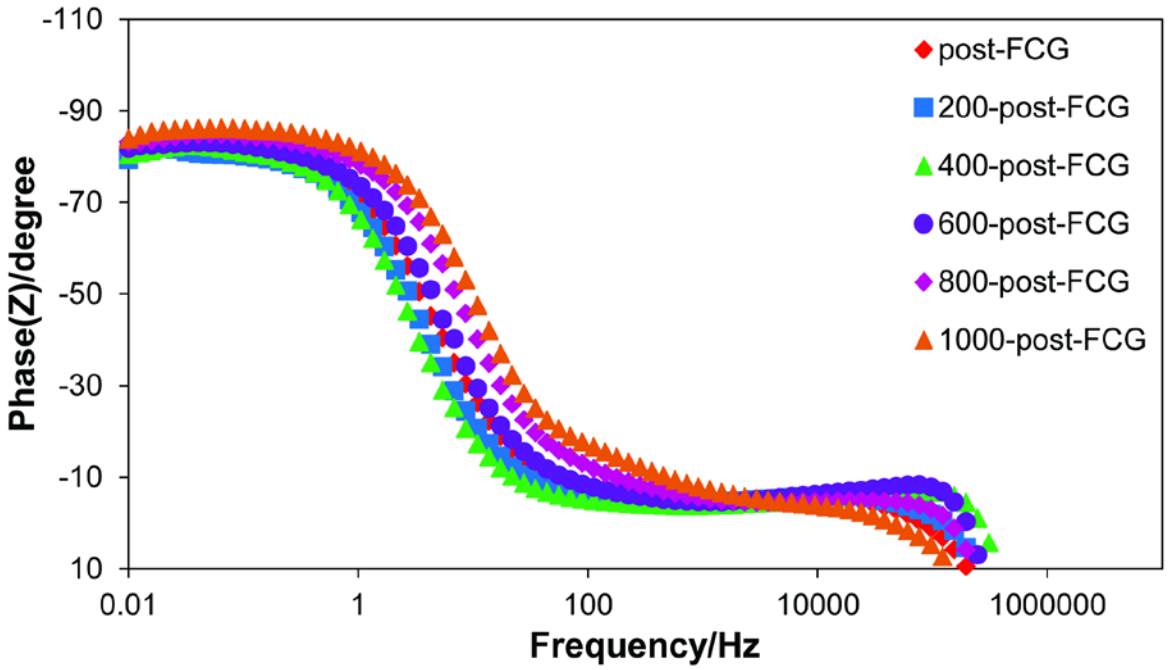

Figure 2.10 Bode plot of annealed FCG samples compared to a post-FCG sample. The 1000-post-FCG electrode is seen to be most capacitive in behavior (closest to -90°).

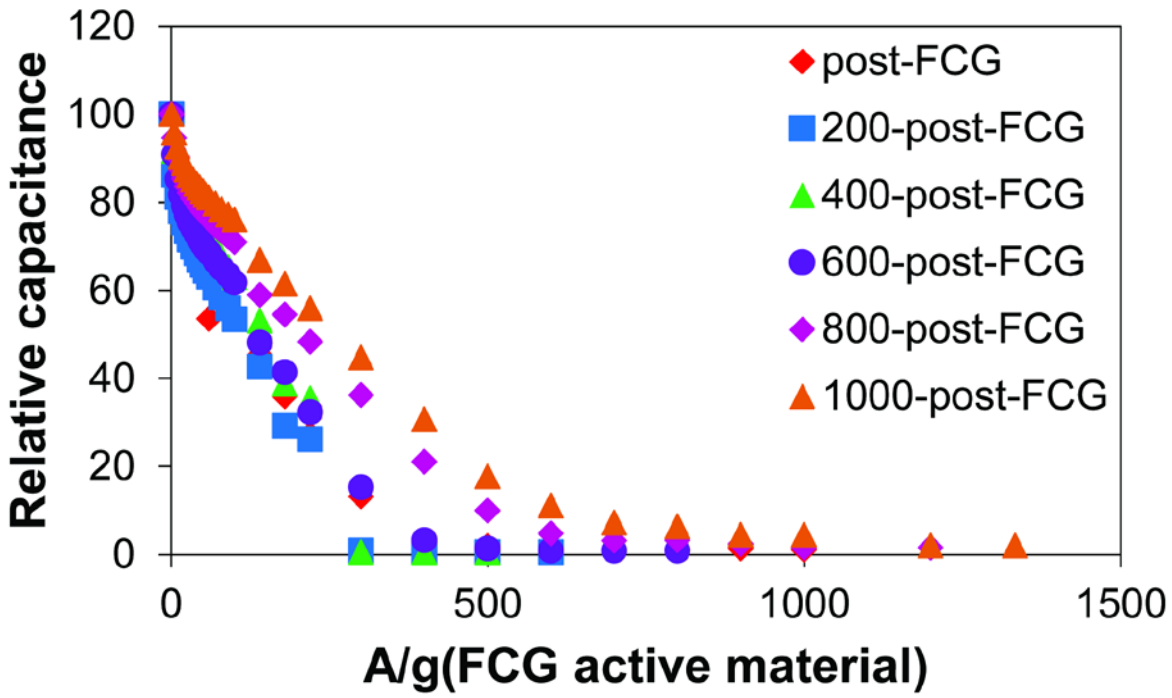

Figure 2.11 Rate capability comparison of FCG and annealed FCG samples. Annealing the post-FCG electrodes gives FCG supercapacitor devices that can operate at higher current densities.

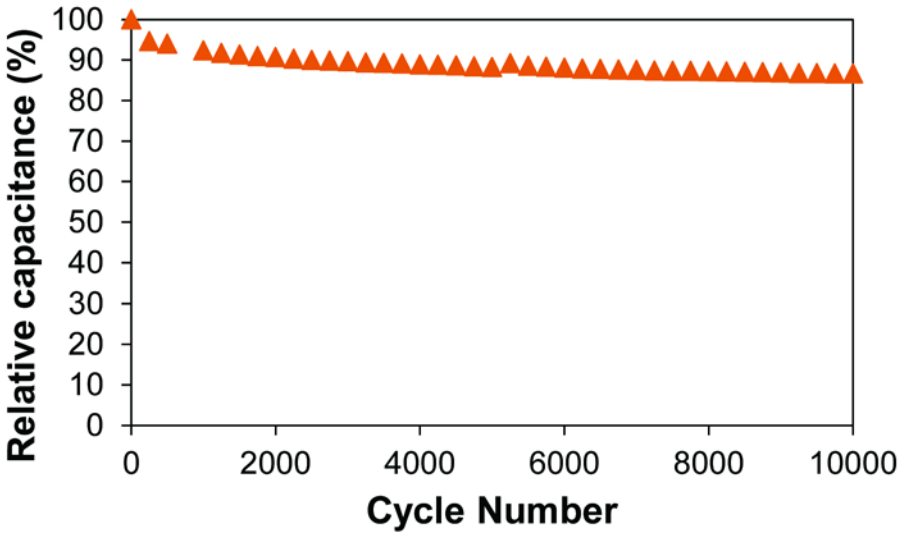

Figure 2.12 Plot of cycle stability for 1000-post-FCG.

2.6 References

1. Hall, P. J.; Bain, E. J. *Energy Policy* 2008, 36, 4352-4355.
2. Pech, D.; Brunet, M.; Durou, H.; Huang, P.; Mochalin, V.; Gogotsi, Y.; Taberna, P.-L.; Simon, P. *Nat Nano* 2010, 5, 651-654.
3. Shamim, A.; Arsalan, M.; Roy, L.; Shams, M.; Tarr, G. *Circuits and Systems II: Express Briefs, IEEE Transactions on* 2008, 55, 643-647.
4. Karden, E.; Ploumen, S.; Fricke, B.; Miller, T.; Snyder, K. *Journal of Power Sources* 2007, 168, 2-11.
5. Hanmin, L.; Zhixin, W.; Jie, C.; Maly, D. *Vehicular Technology, IEEE Transactions on* 2009, 58, 1097-1105.
6. Hanmin, L.; Zhixin, W.; Shutong, Q.; Yunhai, L. In *Improvement of engine cold start capability using supercapacitor and lead-acid battery hybrid*, Applied Power Electronics Conference and Exposition, 2008. APEC 2008. Twenty-Third Annual IEEE, 24-28 Feb. 2008; 2008; pp 668-675.
7. Qu, Q. T.; Shi, Y.; Tian, S.; Chen, Y. H.; Wu, Y. P.; Holze, R. *Journal of Power Sources* 2009, 194, 1222-1225.
8. Shin, D.; Kim, Y.; Wang, Y.; Chang, N.; Pedram, M. *Journal of Power Sources* 2012, 205, 516-524.
9. Kim, Y. *Power Electronics Technology* 2003, 29, 34-39.
10. Thounthong, P.; Raël, S.; Davat, B. *Journal of Power Sources* 2009, 193, 376-385.

11. Kanchev, H.; Di, L.; Colas, F.; Lazarov, V.; Francois, B. *Industrial Electronics, IEEE Transactions on* 2011, 58, 4583-4592.

12. Hadjipaschalis, I.; Poullikkas, A.; Efthimiou, V. *Renewable and Sustainable Energy Reviews* 2009, 13, 1513-1522.

13. Carrasco, J. M.; Franquelo, L. G.; Bialasiewicz, J. T.; Galvan, E.; Guisado, R. C. P.; Prats, M. A. M.; Leon, J. I.; Moreno-Alfonso, N. *Industrial Electronics, IEEE Transactions on* 2006, 53, 1002-1016.

14. Ribeiro, P. F.; Johnson, B. K.; Crow, M. L.; Arsoy, A.; Liu, Y. *Proceedings of the IEEE* 2001, 89, 1744-1756.

15. Winter, M.; Brodd, R. J. *Chemical reviews* 2004, 104, 4245-4270.

16. Ibrahim, H.; Ilinca, A.; Perron, J. *Renewable and Sustainable Energy Reviews* 2008, 12, 1221-1250.

17. Pushparaj, V. L.; Shaijumon, M. M.; Kumar, A.; Murugesan, S.; Ci, L.; Vajtai, R.; Linhardt, R. J.; Nalamasu, O.; Ajayan, P. M. *Proceedings of the National Academy of Sciences* 2007, 104, 13574-13577.

18. Zhang, L. L.; Zhao, X. *Chemical Society Reviews* 2009, 38, 2520-2531.

19. Conway, B. E. *Journal of the Electrochemical Society* 1991, 138, 1539-1548.

20. Conway, B.; Birss, V.; Wojtowicz, J. *Journal of Power Sources* 1997, 66, 1-14.

21. Bard, A. J., Faulkner, Larry R. Electrochemical Methods: Fundamentals and Applications *John Wiley & Sons, Inc., New York* 2001, 87-90, 137-141.

22. Kosynkin, D. V.; Higginbotham, A. L.; Sinitskii, A.; Lomeda, J. R.; Dimiev, A.; Price, B. K.; Tour, J. M. *Nature* 2009, 458, 872-876.

23. Stankovich, S.; Piner, R. D.; Chen, X.; Wu, N.; Nguyen, S. T.; Ruoff, R. S. *Journal of Materials Chemistry* 2006, 16, 155-158.

24. Bagri, A.; Mattevi, C.; Acik, M.; Chabal, Y. J.; Chhowalla, M.; Shenoy, V. B. *Nat Chem* 2010, 2, 581-587.

25. Kuila, T.; Mishra, A. K.; Khanra, P.; Kim, N. H.; Lee, J. H. *Nanoscale* 2013, 5, 52-71.

26. Murugan, A. V.; Muraliganth, T.; Manthiram, A. *Chemistry of Materials* 2009, 21, 5004-5006.

27. Fan, Z.; Wang, K.; Wei, T.; Yan, J.; Song, L.; Shao, B. *Carbon* 2010, 48, 1686-1689.

28. El-Kady, M. F.; Strong, V.; Dubin, S.; Kaner, R. B. *Science* 2012, 335, 1326-1330.

29. Park, S.; Ruoff, R. S. *Nat Nano* 2009, 4, 217-224.

30. Tarasevich, M. R.; Sadkowski, A.; Yeager, E. Oxygen Electrochemistry. In *Comprehensive Treatise of Electrochemistry*, Conway, B.; Bockris, J. M.; Yeager, E.; Khan, S. M.; White, R., Eds. Springer US: 1983; pp 301-398.

31. Pandolfo, A. G.; Hollenkamp, A. F. *Journal of Power Sources* 2006, 157, 11-27.

32. Yang, J.; Gunasekaran, S. *Carbon* 2013, 51, 36-44.

33. Fan, X.; Lu, Y.; Xu, H.; Kong, X.; Wang, J. *Journal of Materials Chemistry* 2011, 21, 18753-18760.

34. Peng, C.; Zhang, S.; Jewell, D.; Chen, G. Z. *Progress in Natural Science* 2008, 18, 777-788.

35. Hulicova-Jurcakova, D.; Seredych, M.; Lu, G. Q.; Bandosz, T. J. *Advanced Functional Materials* 2009, 19, 438-447.

36. Oh, Y. J.; Yoo, J. J.; Kim, Y. I.; Yoon, J. K.; Yoon, H. N.; Kim, J.-H.; Park, S. B. *Electrochimica Acta* 2014, 116, 118-128.

37. Schiffrin, D. J. The electrochemistry of oxygen. In *Electrochemistry: Volume 8*, Pletcher, D., Ed. The Royal Society of Chemistry: 1983; Vol. 8, pp 126-170.

38. Guin, P. S.; Das, S.; Mandal, P. C. *International Journal of Electrochemistry* 2011, 2011.

39. Yang, D.; Velamakanni, A.; Bozoklu, G.; Park, S.; Stoller, M.; Piner, R. D.; Stankovich, S.; Jung, I.; Field, D. A.; Ventrice Jr, C. A. *Carbon* 2009, 47, 145-152.

40. Tuinstra, F.; Koenig, J. L. Raman spectrum of graphite. *The Journal of Chemical Physics* 1970, 53, 1126-1130.

41. Ferrari, A. C. *Solid State Communications* 2007, 143, 47-57.

42. Ferrari, A.; Meyer, J.; Scardaci, V.; Casiraghi, C.; Lazzeri, M.; Mauri, F.; Piscanec, S.; Jiang, D.; Novoselov, K.; Roth, S. *Physical review letters* 2006, 97, 187401.

43. Kaniyoor, A.; Baby, T. T.; Ramaprabhu, S. *Journal of Materials Chemistry* 2010, 20, 8467-8469.

44. Li, D.; Muller, M. B.; Gilje, S.; Kaner, R. B.; Wallace, G. G. *Nat. nanotechnol.* **2008**, 3, 101.

45. Dreyer, D. R.; Park, S.; Bielawski, C. W.; Ruoff, R. S. *Chem. Soc. Rev.* **2010**, 39, 228.

Chapter 3: Influence of Sputter Deposited Gold Current Collector Thickness on the Capacitive Behavior of Flash Converted Graphene Supercapacitors

Abstract

Supercapacitors are traditionally made with a metal foil based current collector in a bottom-contact approach. The metal foil current collectors are known to cause contact resistance at the active material and current collector interface. In this work, a top-contact approach to building flash converted graphene supercapacitor electrodes is presented. The sputter deposition of gold onto flash converted graphene active material prepared in air (air-FCG) was carried out with different gold deposition times leading to different current collector thicknesses. This top-contact approach creates an interlocking jigsaw puzzle design at the interface of the air-FCG active material and current collector. The more intimate interface allows for lower resistance than the traditional carbon coated aluminum foil current collector. Furthermore, an improvement in capacitive behavior is seen for air-FCG with a thicker layer of gold current collector. By using sputter deposition, a new method of using a top-contact approach to provide lower resistance between active material and current collector interface for making FCG supercapacitor devices is developed.

3.1 Introduction

Supercapacitors charge the technology in our lives in many ways.[1] Most of the research on supercapacitors is on improving the electrochemical properties of the electrode active material and electrolyte.[2] However, another part of the supercapacitor that also deserves attention is the

active material and current collector interface. An improvement in the current collector will promote more efficient transport of charges.[3-5]

Some of the basic components of a supercapacitor include the active material, separator, electrolyte, and the current collector. Each of these supercapacitor components is important in increasing capacitance, energy, power, and for lowering resistance. Also, the individual components are each important in improving a supercapacitor's performance in different ways. The current collector transports the electronic current generated from the charges of the electric double layer in the active material to the application that needs energy to operate, and from the power source that charges the supercapacitor electrodes. Having a good current collector and active material interface lowers the resistance and makes the transport of charges more efficient.[6-9] A good active material and current collector interface should have increased conductivity with lower insulating metal oxide layer, optimal adhesion for good mechanical integrity of the active material to the current collector, and a large area of surface contact allowing more pathways for the charges to travel through.[5,7,10]

Traditionally, current collectors are made from a metal foil, such as aluminum. The active material is coated onto the metal foil current collector followed by a possible post-coating processing in this bottom-contact method (Figure 3.1).[6,11,12] The metal foil current collectors are produced by melting a block of the metal, filtering and testing for purity, then made into an ingot of specific dimensions, and milled numerous times (from i.e. 45 cm to <0.025 mm.[13,14] The foils often have significant resistive metal oxide layers on the surface, although a smaller metal oxide layer is advantageous to prevent reactions between the active material and the metal foil;

therefore, a thinner layer is preferred.[7] Furthermore, foils can have problems with keeping the active material adhered onto its surface, which not only increases resistance, but also breaks the charge transport pathways. Another problem that metal foil current collectors have is their surfaces have a certain roughness due to grooves, ridges, and other microstructures that do not necessarily match those of the active material's, thus, hindering the contact surface area between active material and current collector.[2]

The problems with metal foil current collectors have been addressed by several research groups. Several improved methods have been developed[9,11] such as etching the aluminum foil current collector to make it more porous, thereby increasing its contact surfaces[7] or electrospining nickel polymer nanofibers followed by annealing into a nickel foam.[15] Despite these efforts to improve the resistivities, these methods still yield active material and current collector interfaces that possess relatively high resistivities. Some of these methods also involve costly, toxic, and difficult to scale steps. Another way to achieve better adhesion and mechanical integrity of electrodes to current collectors that has been explored is by adding a binder material to the active material, where the binder is usually not conductive. The binder acts as a glue, but is considered dead mass and lowers the energy storage capacity of a supercapacitor device.[6] Perhaps the most successful method to lowering resistance thus far is using a carbon coating on aluminum foil to act as an interface material between active material and current collector.[7,16,17] For example, Portet et al. reported on the use of carbon nanofibers (CNFs) as a coating on aluminum foil current collectors to lower the electrode's internal resistance. Although this method is useful in lowering the resistance, it involves many extra steps. The first step being a

pretreatment etching of the aluminum foil current collectors with chemicals, such as soaking in NaOH for degreasing the foil and then HCl solutions at 80 °C for creating surface roughness. Then there is a subsequent coating of the CNFs onto the aluminum foil through sol-gel formation of carbon materials in a polymer suspension, which is then removed via thermal treatment.[4] Furthermore, these carbon coatings on the aluminum foil current collector still possess appreciable internal resistance.[8]

In this study, the use of a top-contact approach of sputtering gold onto air-FCG electrodes to serve as the current collector is investigated. The air-FCG electrode is more robust and denser, thus, it is easier to handle than post-FCG electrodes. The air-FCG electrode is FCG made from air-dried GO rather than freeze-dried GO. More specifically, the top-contact approach entails using sputter deposition, which employs a physical vapor deposition method, of gold onto the air-FCG electrodes to serve as a current collector (Figure 3.2). In this way, not only is the thickness of the current collector able to be controlled, but the active material and current collector interface also has better adhesion, increased surface contact, and minimized oxide layer. By using this method, the charge transfer across the active material and current collector interface can be greatly improved. The air-FCG and gold current collector is envisioned to fit together like the edges of a jig saw puzzle, thus maximizing contact surfaces (Figure 3.3). Illustrated here is the influence of the sputter deposited gold current collector at different thicknesses on the electrochemical performance of air-FCG. By using a top-contact approach with a gold sputter deposited current collector on an air-FCG electrode, a lower resistance of over 1.4 times improvement than the commonly used carbon-coated aluminum foil current

collector is observed. There is also a dependence of capacitive behavior with increasing gold deposition thickness, allowing for more precise tuning and matching of the current collector to the electrode material for more optimal electrochemical performance.

3.2 Results and Discussion

3.2.1 Morphology, Composition, and Properties of Air-FCG

Flash converted graphene (FCG) prepared by photothermal conversion of graphene oxide (GO) dried on a substrate in air (air-FCG) is denser, but more robust than pre-FCG and post-FCG. The density of air-FCG is 0.069 g/cm^3, which is almost two times higher than that of pre-FCG (0.039 g/cm^3) and more than 8 times higher than that of post-FCG (0.0080 g/cm^3). Scanning electron microscopy (SEM) images of air-FCG (Figure 3.4) show a scale-like morphology on the surfaces of air-FCG. The raised scales on the surface of air-FCG is believed to be produced from the escaping of H_2O vapor and CO_2 gas upon flashing the air-dried graphene oxide films. The air-FCG electrodes have a surface area of 343 m^2/g as determined using a methylene blue method. This surface area is good relative to other graphene materials used as electrodes, but is lower than FCG made from freeze-dried GO (525 m^2/g). The lower surface area of air-FCG is supported by its higher density and lower porosity as seen from the SEM images (Figure 3.4). However, the advantage to air-FCG is that it is more robust than FCG made via freeze-dried GO, making it easier to handle and manipulate for purposes such as the sputter deposition process. The increased density and lower porosity of air-FCG compared to pre-FCG and post-FCG makes it more robust. A film of air-FCG is able to be easily lifted off a

substrate, held with tweezers, undergo vacuum purging of the sputter chamber and subsequent refilling of argon or air, and survive gold particles being deposited on its surface.

The majority of the oxygen groups in the air-dried GO were reduced as confirmed by XPS. The air-FCG electrodes have 87.2% carbon and 12.8% oxygen, which is comparable to FCG made via freeze-drying GO (post-FCG oxygen content is 14.4%).

3.2.2 Sputter Deposited Gold Current Collector on Air-FCG Electrodes

Gold was sputter deposited onto air-FCG in a top-contact approach to make the current collector. The air-FCG electrodes were loaded into the sputterer with one side facing up. The deposition was allowed to take place for different amounts of time: 30, 60, 120, 240, 480, 720, 960, and 1200 seconds. The different times of sputtering gold onto air-FCG gave different gold film thicknesses of 1, 5, 10, 20, 40, 60, 80, and 100 nm for sputter deposition times of 30, 60, 120, 240, 480, 720, 960, and 1200 seconds, respectively. The gold current collector can be visibly seen to be a smooth homogeneous film covering the surface of the air-FCG electrodes (Figure 3.5). The gold is well adhered to the air-FCG surfaces, and cannot be separated, whereas metal foil current collectors made using the bottom-contact approach can be separated. Furthermore, as seen in Figure 3.5, a longer sputter deposition time gives an air-FCG surface that is deeper gold in color. In Figure 3.4 the SEM images of air-FCG also show a progressively thicker layer of gold on top of the air-FCG surface as the deposition time increases. However, with all of the deposition times and thicknesses, the surface morphology was preserved. The SEM images also reveal that the gold is deposited as a uniform, homogeneous, smooth film on the air-FCG surface with no aggregated gold particles observed. The wt% of gold, with respect

to carbon, on the air-FCG electrodes increases (5.31%, 7.38%, 12.89%, 27.23%, 69.84%, 74.59%, 81.07%, and 89.48%) with increasing gold sputter deposition time (30, 60, 120, 240, 480, 720, 960, and 1200 seconds). The progressive increase in wt% of gold on air-FCG with increasing deposition time further supports the increase of a thicker gold film current collector forming on the electrode.

3.2.3 Electrochemical Performance of Air-FCG with Gold Sputter Deposited Current Collector

The air-FCG electrodes with gold sputter deposited current collector tested in a CR2032 coin cell gave lower resistance and overall improved capacitive behavior. The capacitive behavior of the air-FCG electrodes varies with thickness of the sputter deposited gold current collector. When the gold sputter deposition time is less than 480 seconds (40 nm gold), the capacitance is essentially non-existent at 0.20-0.36 $F/g_{FCG/electrode}$ and 0.01 $F/cm^3_{FCG/electrode.}$ The capacitance increases linearly from 480 seconds to 1200 seconds of sputter deposition time from 0.47 $F/cm^3_{FCG/electrode}$ to 1.18 $F/cm^3_{FCG/electrode}$ and 13.75 $F/g_{FCG/electrode}$ to 35.15 $F/g_{FCG/electrode}$. The specific energy of air-FCG deposited for 0, 30, 60, 120, 240, 480, 720, 960, and 1200 seconds are 0.04, 0.04, 0.03, 0.05, 0.03 1.91, 3.54, 3.83, and 4.88 Wh/kg, respectively (Figure 3.6). The first dramatic increase in energy is seen between 240 and 480 seconds of gold deposition times (20 and 40 nm of gold current collector). A thicker gold current collector coverage on air-FCG gives a higher capacitance. The cyclic voltammetry (CV) and constant current (CC) plots in Figure 3.7 illustrate the trend from resistive to electric double layer behavior through increasing the gold current collector thickness. Without any current collector (0 nm of gold deposited on

air-FCG), the CV curve shows that air-FCG is highly resistive, with no EDLC behavior and no capacitance retained. In fact, the resistive behavior is also seen for the air-FCG devices with between 0 to 20 nm of gold sputter deposited current collector. At 40 nm of gold current collector, the air-FCG device shows less resistive behavior, with the CV shape starting to look more rectangular. Between 60 to 100 nm of gold current collector, the air-FCG devices progressively become more EDL in behavior and increase in capacitance. The most dramatic changes in the CV curves of the air-FCG samples are between sputter deposited gold current collector thicknesses of 20 to 60 nm. The gold thickness that provided the most rectangular and EDL behavior of the air-FCG devices is 100 nm. The constant current curves of the air-FCG devices with different gold sputter deposition times further supports the increase in EDL behavior as the gold current collector thickness is increased. The most prominent change in EDL behavior is from 20 to 60 nm of gold. The voltage drop (IR drop) can also be seen to decrease dramatically from 40 to 60 nm thicknesses of the gold sputtered current collector. The voltage drop decreases from 0.04 to 0.02 V between gold thicknesses of 0 nm to 100 nm. A more intimate interface between the active material and current collector provides a better pathway for charge transport and subsequently lowers the resistance.

The specific power also increases with increasing gold thickness. The specific power for 0 seconds of gold deposition is 4.7×10^4 W/kg, whereas, the specific power for 1200 seconds of gold deposition is 1.2×10^5 W/kg (Figure 3.6). Furthermore, the specific power of air-FCG with gold deposition times of less than 240 seconds were essentially non-existent. The first significant increase in power occurred between 240 and 480 seconds.

Another factor affected by the sputter deposition time of the gold current collector is the resistance R_s. The R_s characterizes the resistance of the electrolyte as it contacts the current collector and the electrode.[13] The resistance is decreased if the charges formed by the double layer are more easily transported from the active material through the current collector to the circuit. Thus, the contact area and adhesion of the interface between the active material and the current collector is crucial to lowering R_s. The most optimal interface would not only have a thinner resistive oxide layer, but also have a better adhesion between the active material and current collector for increased mechanical integrity. Furthermore, an increased contact surface area between the active material and current collector allows for more pathways for charges to travel through. The sputter deposition of a metal such as gold onto the active material in a top-contact synthesis approach results in a thinner oxide layer, better active material adhesion to the current collector, and more interface contact area. The R_s of the air-FCG samples is lower than that of the air-FCG on an aluminum foil coated with carbon current collector made in a bottom-contact synthesis method. The air-FCG electrode with the highest energy and gold deposition time of 1200 seconds resulted in an R_s of 0.95 ohms. For comparison, the R_s of the air-FCG electrode on an aluminum foil coated with carbon current collector is 1.37 ohms. Furthermore, the equivalent series resistance (ESR) of the air-FCG electrode with gold sputtered current collector is 7.46 ohms and that of air-FCG electrode with aluminum foil coated with carbon current collector is 7.86 ohms.

The Nyquist plot of the air-FCG samples with different gold deposition thicknesses further supports that capacitive behavior is seen to emerge with air-FCG at 40 nm of gold current

collector and improves with increasing gold thickness (Figure 3.8). From the Bode plot, the air-FCG sample with 40 nm gold sputtered current collector thickness is seen to be more capacitive in behavior (-76°) than those with less than 40 nm gold (-12° to -19°). The air-FCG electrodes with more than 40 nm gold are more capacitive in behavior as they have phase angles closer to -90° (Figure 3.9).

Rate capability is also seen to improve significantly with increased thickness of the sputter deposited gold current collector. Between 0 to 40 nm of gold thickness, the capacitance is stable at less than 5 A/g (Figure 3.10) and drops to less than 20% at 5 A/g. At 60 and 80 nm, however, air-FCG shows 75% capacitance at 5 A/g, and at 100 nm gold current collector the capacitance drops to only 85%.

3.3 Conclusions

The top-contact approach to make more efficient current collectors for air-FCG electrodes were made using sputter deposition of gold. It can be gleaned from this study that this method of sputter depositing current collectors lowers the resistance of air-FCG supercapacitor devices by over 1.4 times as compared to air-FCG with aluminum foil-based current collectors. There is also a trend in increased deposition thickness, whereas, the absence of a current collector shows nearly non-existent capacitive behavior (i.e. 0.04 Wh/kg) while air-FCG with around 40 nm of gold current collector shows an improved capacitive behavior (i.e. 1.91 Wh/kg). The specific energy of air-FCG with 100 nm of gold current collector is 4.88 Wh/kg. This top-contact approach allows for more control tuning the thickness of the current collector and subsequently the electrochemical performance of the FCG device. This method also leads to a

better understanding of the role of the current collector. Thus, construction of next-generation supercapacitors can be fully optimized by this top-contact approach using a sputter deposited current collector.

3.4 Experimental Section

3.4.1 Synthesis of air-FCG

Air-FCG was prepared by casting an aqueous dispersion of 1.7% graphene oxide (GO) onto an aluminum foil substrate using a Guardco automatic drawdown machine II with blade height of 610 micrometers. GO was prepared using a modified Hummer's Method.[18,19] The cast GO was allowed to dry in air at room temperature overnight. After the GO film was dry, it was exposed to 5 flashes of 240 J from an Alien Bees B1600 flash lamp to convert the GO to FCG. The FCG sheets were then detached from the aluminum foil substrate and transferred to a piece of paper towel as an intermediate substrate, and punched into 15 mm diameter electrode discs using a McMaster-Carr round hole arch punch.

3.4.2 Sputter Deposition of Gold onto Air-FCG Electrodes

The air-FCG electrodes were placed on the deposition chamber platform of an Anatech Hummer 6.2 Sputtering System. After purging the chamber with argon, the sputter process began by setting the plasma current to 15 mA and the voltage control position to 7. The chamber vacuum was maintained at 80±5 militorrs with the process gas argon for the allocated sputter deposition time. The air-FCG gold sputter deposition times were 30, 60, 120, 240, 480, 720, 960, and 1200 seconds.

3.4.3 Coin Cell Fabrication

The air-FCG electrodes with sputter deposited gold current collectors were made into CR2032 coin cells. Each of the sputtered air-FCG electrodes were removed from its paper towel substrate and assembled into a coin cell. The separator used for all air-FCG coin cells is made of polypropylene and the electrolyte used is 1.0 M tetraethyl ammonium tetrafluoral borate ($TEABF_4$) in acetonitrile. The cells were crimped using an MTI coin cell CR2032 crimper before testing.

3.4.4 Electrochemical Measurements and Calculations

All air-FCG coin cell devices were measured using an Biologic VMP3 potentiostat with a VMP3b-10 Amp booster. The measurement method and calculations used for this work were the same as that carried out for post-FCG as shown in previous work (see chapter 1.4.5 and 1.4.6). All electrochemical results: capacitance, energy, power, ESR, and voltage drop were calculated from the constant current curves at 1 $A/g_{air\text{-}FCG}$ from 0 V to 2 V. The rate capabilities were also determined from the constant current curves by measuring the air-FCG samples at varying current densities ranging from 1 A/g to 220 A/g. Electrochemical impedance spectroscopy (EIS) was used to further investigate the influence of the different gold current collector thicknesses on the capacitive behaviors of the air-FCG electrodes. Nyquist and Bode plots from the EIS measurements were analyzed from 1 MHz to 10 mHz at open circuit potential.

Capacitance was calculated for each of the air-FCG devices by dividing the current by the rate of the change in voltage (dv/dt). The specific energy was calculated by multiplying the capacitance by $\frac{1}{2} \cdot V^2$, where V is operating voltage window, and dividing by the mass of air-

FCG active material. For finding the capacitance per electrode, the gravimetric and volumetric capacitances were multiplied by a factor of 4 to account for halving the mass or volume and for accounting for the electrodes being in the series circuit configuration.

3.4.5 Characterization: Morphology, Composition, and Properties.

SEM images and EDS measurements for gold wt% of the air-FCG electrodes with sputter deposited gold current collector of different deposition times were taken using a FEI Nova 230 Nano SEM. The carbon and oxygen amounts found in air-FCG were measured using a Kratos AXIS Ultra DLD with a monochromatic Al Kα X-ray source X-ray photoelectron spectroscopy (XPS) operating at 10 mA and 15 kV. All XPS data were processed using CasaXPS 2.3 software.

Methylene blue adsorption was used to determine the surface area of air-FCG. Methylene blue was purchased from Fisher Scientific. A sample of air-FCG was stirred in a solution of Methylene blue in water overnight. The UV-vis of the methylene blue supernatant solution was measured using a Shimadzu UV/visible/near IR spectrophotometer. The surface area was calculated from the concentration difference of methylene blue from before and after addition of air-FCG.

3.5 Figures

Figure 3.1 Method for making commercial supercapacitor electrodes involves a bottom-contact of active material to the current collector. The process starts with the appropriate metal foil current collector. Then, the active material is coated onto the metal foil current collector. The coating is then dried to give the final electrode product.

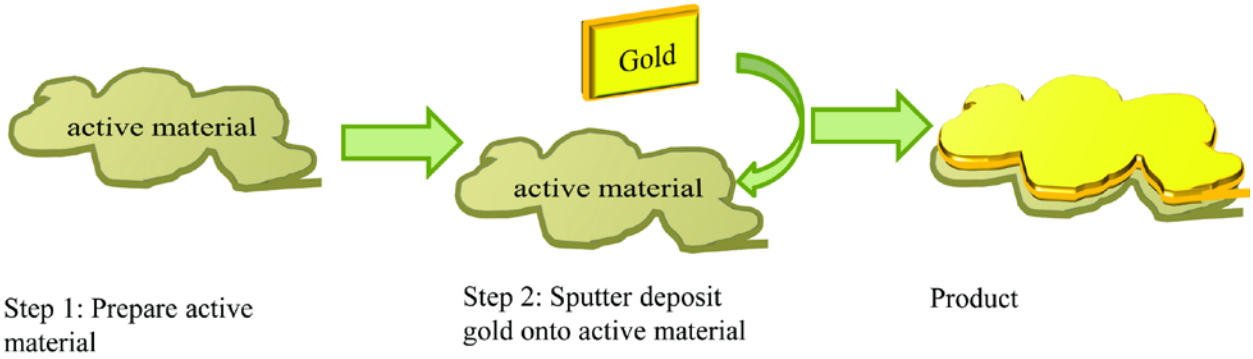

Figure 3.2 Electrode preparation method using top-contact of sputter deposited gold current collector onto FCG active material.

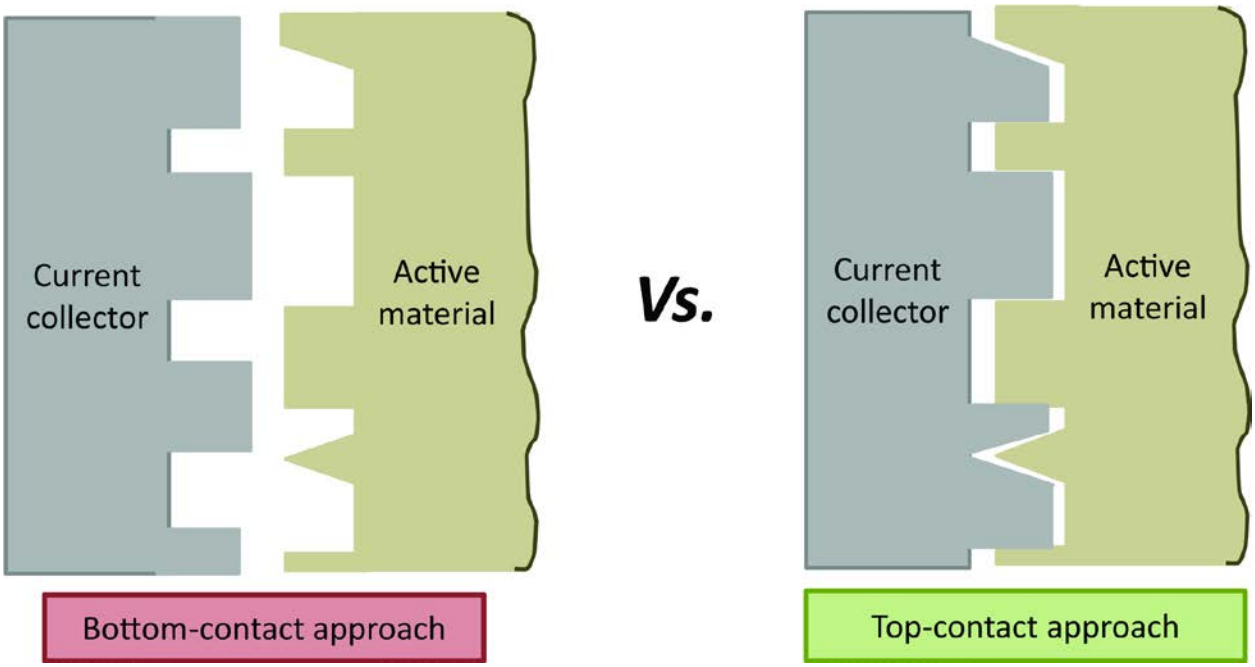

Figure 3.3 The interface of the bottom-contact approach gives lower surface contact between active material and current collector, but the top-contact approach provides a way to increase the contact surfaces of the active material and current collector.

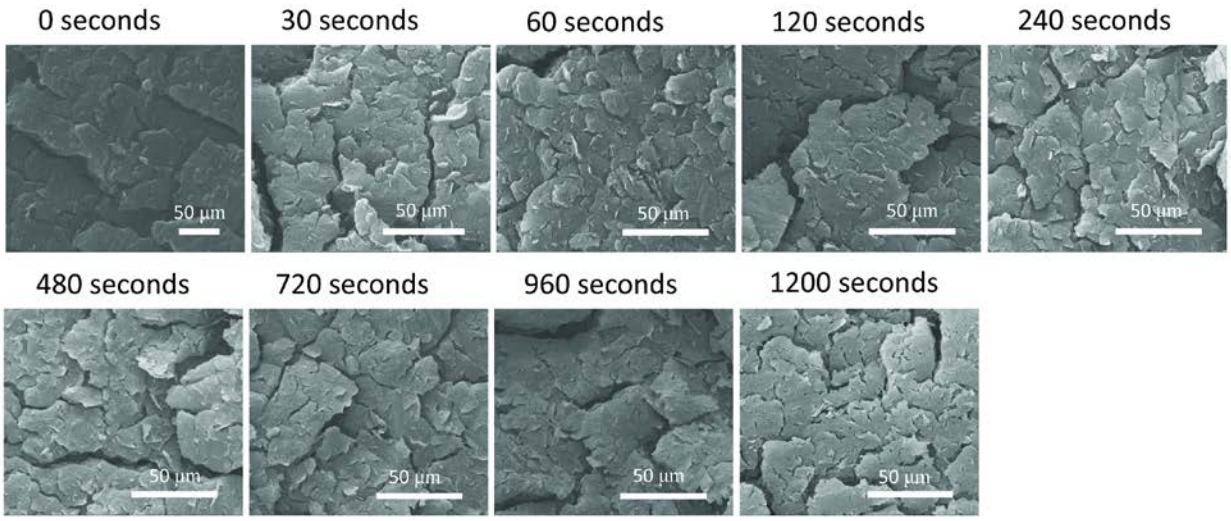

Figure 3.4 The SEM images of the air-FCG electrodes with different gold sputter deposition times show a surface morphology similar to that of air-FCG with no gold. Also, no aggregation of gold particles is seen for any of the air-FCG electrodes.

Figure 3.5 Increasing the gold sputter deposition time gives an air-FCG electrode with more gold visible on the electrode surface.

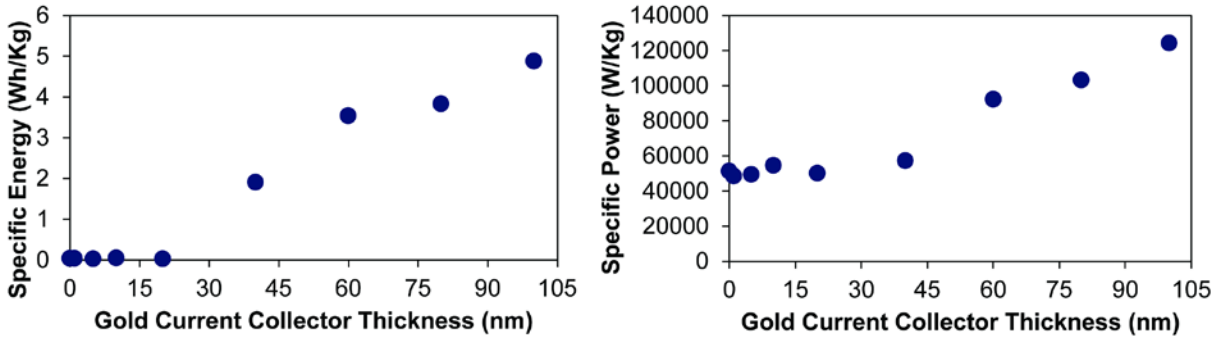

Figure 3.6 An increase in specific energy (left plot) and specific power (right plot) is seen with an increase in gold thickness.

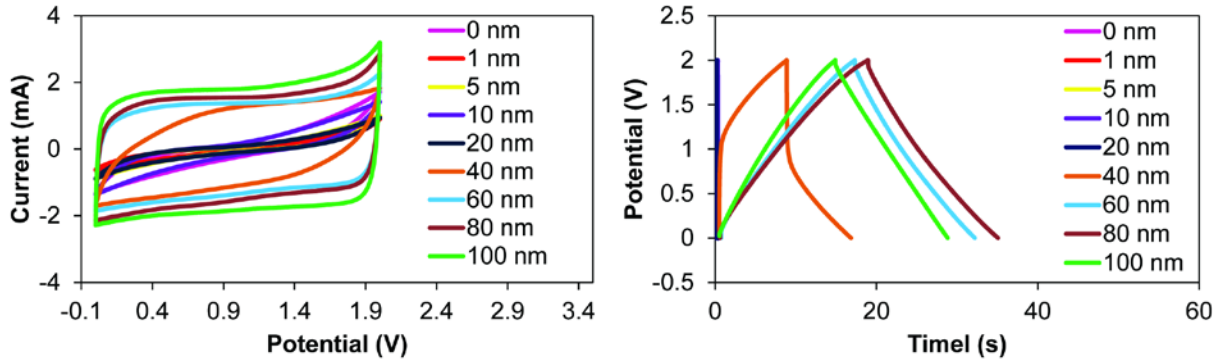

Figure 3.7 Cyclic voltammograms (left) and constant current curves (right) of air-FCG electrodes with increasing gold thicknesses. The air-FCG supercapacitor devices become more ideal in behavior as the thickness of the gold current collector increases.

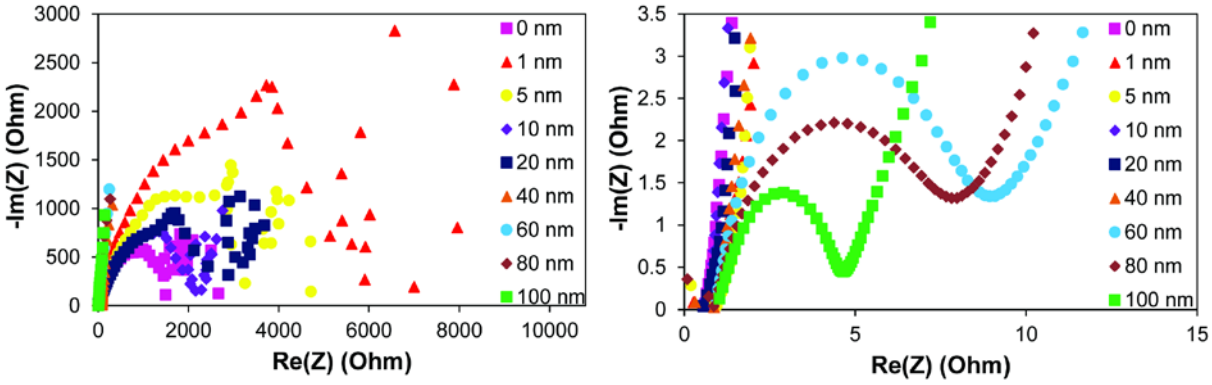

Figure 3.8 Nyquist plot of air-FCG with different gold current collector thicknesses. The right plot magnifies the Nyquist plot at resistance values between 0-15 ohms. The resistance of the air-FCG supercapacitor devices is seen to decrease as the gold thickness increases. Additionally, the air-FCG supercapacitor devices become more capacitive as the gold thickness increases.

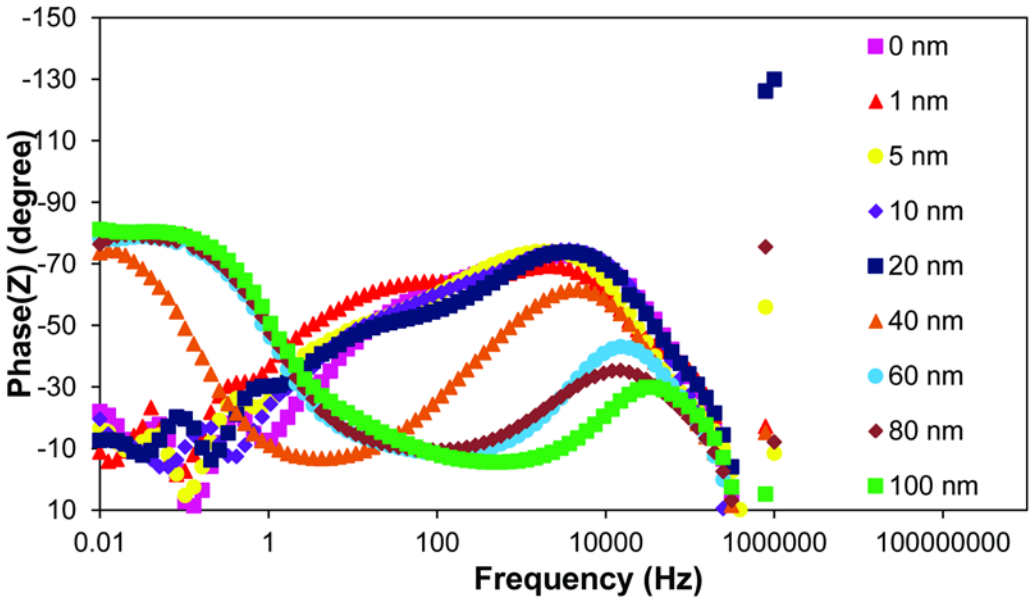

Figure 3.9 The Bode plot of air-FCG with increased gold current collector thicknesses. As the gold thickness increases, the air-FCG supercapacitor devices become closer to a capacitor in behavior (i.e. approaching -90°).

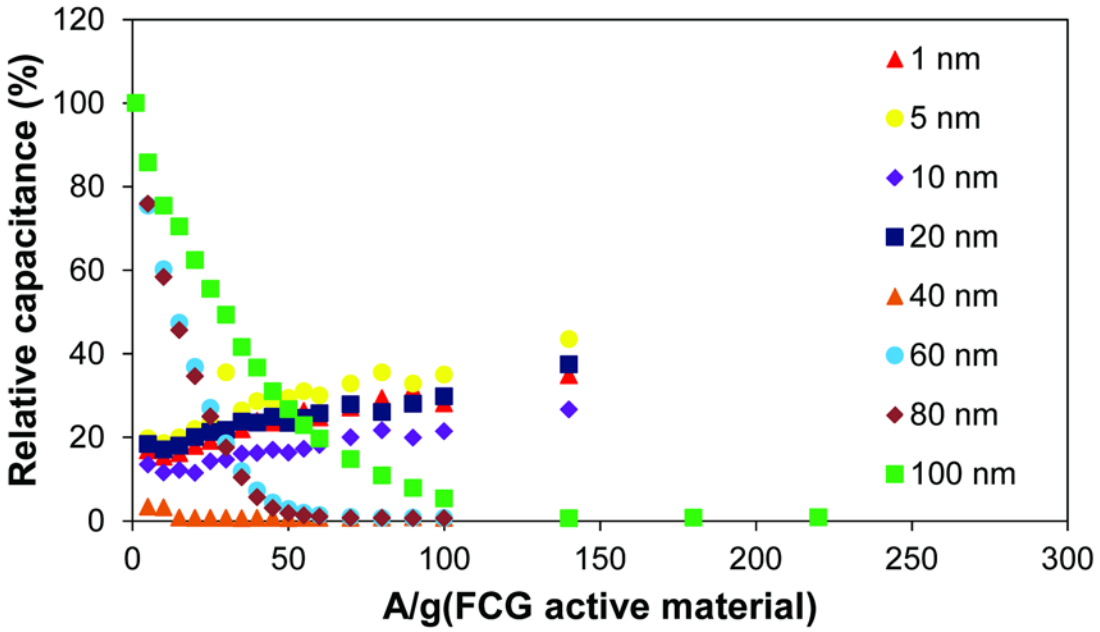

Figure 3.10 The plot of rate capability (current density vs. relative capacitance) of air-FCG with different gold current collector thicknesses show that a thicker layer of gold allows the air-FCG supercapacitor device to be more efficient in storing charge at higher current densities.

3.6 References

1. Zhang, L. L.; Zhao, X. *Chemical Society Reviews* 2009, 38, 2520-2531.
2. Pandolfo, A. G.; Hollenkamp, A. F. *Journal of Power Sources* 2006, 157, 11-27.
3. Schneuwly, A.; Gallay, R. Properties and applications of supercapacitors: From the state-of-the-art to future trends. *Rossens, Switzerland* 2000.
4. Portet, C.; Taberna, P. L.; Simon, P.; Flahaut, E. *Journal of The Electrochemical Society* 2006, 153, A649-A653.
5. Chmiola, J.; Largeot, C.; Taberna, P.-L.; Simon, P.; Gogotsi, Y. *Science* 2010, 328, 480-483.
6. Portet, C.; Yushin, G.; Gogotsi, Y. *Carbon* 2007, 45, 2511-2518.
7. Portet, C.; Taberna, P. L.; Simon, P.; Laberty-Robert, C. *Electrochimica Acta* 2004, 49, 905-912.
8. Yoon, B.-J.; Jeong, S.-H.; Lee, K.-H.; Seok Kim, H.; Gyung Park, C.; Hun Han, J. *Chemical Physics Letters* 2004, 388, 170-174.
9. Burke, A. *Journal of Power Sources* 2000, 91, 37-50.
10. Yoo, J. J.; Balakrishnan, K.; Huang, J.; Meunier, V.; Sumpter, B. G.; Srivastava, A.; Conway, M.; Mohana Reddy, A. L.; Yu, J.; Vajtai, R. *Nano letters* 2011, 11, 1423-1427.
11. Obreja, V. V. N. *Physica E: Low-dimensional Systems and Nanostructures* 2008, 40, 2596-2605.
12. Stoller, M. D.; Park, S.; Zhu, Y.; An, J.; Ruoff, R. S. *Nano Letters* 2008, 8, 3498-3502.

13. DeGarmo, E. P.; Black, J.; Kohser, R. A.; Klamecki, B. E. Materials and process in manufacturing. *Jolm Wiley and Sons, USA* 2003, 974.

14. Robertson, G. L. *Food packaging: principles and practice*. CRC press: 2012.

15. Liu, D.; Wang, Q.; Qiao, L.; Li, F.; Wang, D.; Yang, Z.; He, D. *Journal of Materials Chemistry* 2012, 22, 483-487.

16. Striebel, K.; Shim, J.; Sierra, A.; Yang, H.; Song, X.; Kostecki, R.; McCarthy, K. *Journal of Power Sources* 2005, 146, 33-38.

17. Brousse, T.; Taberna, P.-L.; Crosnier, O.; Dugas, R.; Guillemet, P.; Scudeller, Y.; Zhou, Y.; Favier, F.; Bélanger, D.; Simon, P. *Journal of Power Sources* 2007, 173, 633-641.

18. Li, D.; Muller, M. B.; Gilje, S.; Kaner, R. B.; Wallace, G. G. *Nat. nanotechnol.* **2008**, 3, 101.

19. Dreyer, D. R.; Park, S.; Bielawski, C. W.; Ruoff, R. S. *Chem. Soc. Rev.* **2010**, 39, 228.

Chapter 4: Improving Energy and Power of Flash Converted Graphene Supercapacitor Electrodes by Compositing with Activated Carbon

Abstract

Commercial supercapacitor electrodes are manufactured with activated carbon (AC) materials. However, because of the poor inter-particle contact, the electrochemical performance of the activated carbon based supercapacitors is not as ideal as it can be. In this research, flash converted graphene (FCG) is used in a composite with activated carbon to make a high energy, high power supercapacitor electrode. The uniform composite of flash converted graphene and activated carbon shows a synergistic effect, where the electrochemical properties are improved compared to that of the activated carbon or flash converted graphene only devices. Several different mixing parameters were explored to produce a uniform composite film. The capacitance, specific energy, and specific power of FCG/AC composite supercapacitors at 2 V window are 113 $F/g_{/electrode}$, 16 Wh/kg, and $4x10^5$ W/kg. The capacitance of FCG/AC with 2.7 V window is 124 $F/g/_{electrode}$. The thicknesses of the composite device is also explored, and the results show that the highest capacitance (212 mF) is achieved for the thickest electrode film (93 μm of active material on one electrode), but the thickest film also has the longest time constant (1.33 s).

4.1 Introduction

Supercapacitors are becoming increasingly important in everyday life, thus, many commercial technologies are replacing batteries with supercapacitors.[1-5] There have emerged

many companies world-wide that specialize in supercapcaitor production for various technologies, i.e. portable electronics,[1] memory protection,[2] cold start of trucks, electric vehicles.[3-5] The leading material currently used in commercial supercapacitor electrodes is activated carbon (AC). Activated carbon is carbon that has been altered to be porous so that it has a high surface area (over 500 m^2/g) for ion adsorption. The conductivity of activated carbons depends on its porosity. Higher porosity gives lower conductivity, ranging from a few tens of mS/m up to 100 mS/m.

Activated carbon can be synthesized using many different methods. One of the predominant methods used for commercial supercapacitor electrodes is by activating coconut shells. For example, coconut shells can be physically activated using CO_2 at 800 °C or chemically activated with phosphoric acid at 500 °C.[6] The pore sizes are controlled through using different synthesis methods. Activated carbon electrodes show around 100-200 F/g of capacitance in aqueous electrolytes and 50-150 F/g in organic electrolytes, and have specific energies of 1-10 Wh/kg and specific powers of above 500 W/kg.[7] Although activated carbon has high surface area and reasonable conductivity, the energy of activated carbon supercapacitors is still at least around 6 times lower than batteries.[8]

One cause of resistance in activated carbon electrodes is poor inter-particle contact, leading to a decrease in effective conductivity.[7] The electrochemical performances can be improved by increasing the inter-particle contact by incorporating another type of material to composite with the activated carbon particles. Thus, composites have been investigated to enhance electrochemical properties of charge storage and reduce ESR in the activated carbon

electrodes. The motivation is for the composite to form a potentially synergistic effect. For example, Portet et al. found that by adding double-walled carbon nanotubes to activated carbon electrodes, the ESR was lowered. They found that the addition of 30% CNTs lowered the ESR from 0.50 ohm•cm^2 to 0.35 ohm•cm^2.[9] Many types of composites are synthesized and different types of composites target different electrochemical properties depending on the types of materials used in the electrodes. Yan et al. used MnO_2 to composite with graphene to make a supercapacitor that has three times higher capacitance than pure graphene.[10] In ideal cases, the composites used for electrode materials have more than one active material for charge storage. For example, one of the composite materials could act as the matrix or substrate material and the other(s) provide the energy enhancing components.[11-13] For pure electric double layer capacitor (EDLC) devices, all the individual materials used to form the composite electrode material needs to be absent of redox components.[14] One advantage of pure EDLC electrode materials is that they have relatively higher power. Some examples of materials used in carbon composite are carbon nanotubes, carbon fibers, nanodiamond, carbon felts, carbon black, carbon aerogels, and graphene.[7,12,14,15]

Graphene, subject of the Physics 2010 Noble Prize,[16,17] is a highly conductive sheet of carbon with sp^2 bonded carbons. Graphene is unique because of its ballistic transport.[16] Furthermore, graphene's sheet-like morphology enables it to be a good composite material acting much like a matrix for the AC particles. For example, not only does graphene serve as an electron highway for the charges stored in AC particles by connecting AC particles to each other and to the current collector (Figure 4.1), but it can also hold a significant amount of charge in its

graphene sheets because of its high conductivity and surface area. In order for the graphene to optimize its role as an electron highway for the AC particles, the graphene sheets need to be disordered, corrugated, and low density in morphology.

Flash converted graphene (FCG) is a good candidate because of its 3D morphology, and because of its excellent electrochemical properties as previously shown.[18] Thus, in this study FCG is used as the graphene source to composite with AC. The FCG/AC composite electrode material is expected to have improved EC performances as compared to 100% AC or 100% FCG electrode materials. There are several important variables for improving the performance of the FCG/AC composite. One way is to optimize the mixing method to ensure homogeneity. The best method of mixing is through probe sonication and ball milling, where the uniformity from each of these methods is comparable. The capacitance of FCG/AC (113 $F/g/_{electrode}$) is higher than that of either pure FCG (77 $F/g/_{electrode}$) or pure AC (80 $F/g/_{electrode}$). Furthermore, the voltage window of FCG/AC is able to be extended to 2.7 V. Also, by tuning the FCG/AC electrode film thickness, the capacitance and frequency response can be optimized for a desired application. In this study, the homogeneous composite of FCG and AC produced an electrode that gave improved and tunable EC performances with varying thicknesses.

4.2 Results and Discussion

4.2.1 Homogeneity of FCG/AC Composite Electrodes

Flash converted graphene (FCG) and activated carbon were mixed together to form homogeneous supercapacitor electrodes. Several different mixing methods were tested to optimize and ensure uniform FCG and AC electrode films. The homogeneity of electrode active

material is especially important because it can affect synergistic contributions of composites. The morphology and uniformity of FCG/AC composites, which were made with the same FCG:AC ratio and cast in the same way as with pre-FCG, i.e. prepared using bath sonication, probe sonication, or ball milling, were compared. Figure 4.2A shows the morphology of FCG/AC electrode films prepared via stirring for 10 min, then bath sonicated for 99 min, and followed by 5 min of stirring. The FCG and AC particles are seen to be non-uniform, with AC particle size ranging anywhere from <10 μm to >10 μm. Furthermore the graphene sheets are aggregated together and located in a few pockets among the AC particles instead of being evenly distributed. The FCG/AC composite electrodes made from probe sonication, however, gave a more uniform distribution of AC particles and graphene sheets as seen from Figure 4.2B. In this method, the FCG and AC slurry, consisting of FCG, AC, binder, and water, were stirred for 10 min, then probe sonicated for 60 min, then stirred for 5 more min. The AC particles in the probe sonication method are on average smaller and more uniform in size (<10 μm) than AC particles from the bath sonication method. The graphene sheets are also smaller and more uniform, and do not aggregate as much as those in the bath sonication method.

Ball milling was another mixing method that was explored. Ball milling, like probe sonication, also showed a uniform mixture of graphene and AC particles in the electrode films (Figure 4.2C). The FCG/AC composite prepared in this method was carried out by ball milling AC and water at 800 rpm for 15 min, then adding FCG into the slurry and ball milling again at 800 rpm for 15 min, then finally adding binder and ball milling at 800 rpm for 15 min. The homogeneity of the FCG/AC composite as prepared by ball milling looked very similar to that

prepared by probe sonication and also showed similar capacitive behavior. The capacitance of the FCG/AC supercapacitor device via probe sonication is 126 mF, via ball milling is 123 mF, and via bath sonication method is 86 mF. When comparing the capacitance of the FCG/AC electrodes to those prepared by bath sonication, it can be seen that the more uniform methods such as probe sonication and ball milling gives better EC performances. In this study probe sonication is used to illustrate the FCG/AC composite electrode performances.

4.2.2 Synergistic EC Properties for FCG/AC Composite Electrodes

FCG and AC act synergistically as a composite electrode material for improving the electrochemical properties. Activated carbon particles are high in surface area and have relatively good conductivity.[19-21] Graphene has higher conductivity along with high surface area, and its sheet morphology allows it to transport electrons efficiently.[16,22] The graphene sheets act as an electron highway by connecting the activated carbon particles to each other and to the current collector. The capacitance of the FCG/AC composite supercapacitor calculated from Equation 4.1 is 113 $F/g_{/electrode}$ and 15 $F/cm^3_{/electrode}$, which is greater than that of pure FCG supercapcitor (77 $F/g_{/electrode}$, 0.98 $F/cm^3_{/electrode}$). Because FCG graphene (0.0080 g/cm^3) has a lower density than activated carbon (0.48 g/cm^3), having a larger thickness per mass, it has a higher gravimetric capacitance, but a lower volumetric capacitance than activated carbon supercapacitors. The density of the FCG/AC electrodes is 0.26 g/cm^3. The capacitance of an activated carbon supercapacitor is 80 $F/g_{/electrode}$ and 38 $F/cm^3_{/electrode}$. The specific energy also shows an improvement with the FCG/AC composite (16 Wh/kg) as compared to pure FCG (10 Wh/kg) and AC (11 Wh/kg). The FCG/AC composite as seen from the CV in Figure 4.3 has a

nearly ideal EDL behavior and maintains an ideal rectangular shape even at high scan rates of 1000 mV/s. Furthermore, the FCG/AC composite supercapacitor shows a maximum phase angle reaching -88°. The phase angle of the FCG/AC composite is therefore closer to the ideal angle than either the 100% FCG (-83°) or the 100% AC (-85°) supercapacitors. Additionally, from a comparison of the Bode plot curves of FCG/AC, FCG, and AC supercapacitor (Figure 4.4) the frequency response of the FCG/AC composite (0.59 s) is greater than that of FCG (0.23 s), but lower than that of AC (3.8 s). The specific power of the FCG/AC composite ($4x10^5$ W/kg) is lower than that of the pure FCG ($5.6x10^5$ W/kg), but one order of magnitude higher than that of AC ($6x10^4$ W/kg) supercapacitors. The synergistic effect of the FCG/AC composite material also improves the rate capability. The rate capability of the FCG/AC composite is 1.1 times greater than that of FCG, and 8.8 times greater than that of AC (Figure 4.5).

4.2.3 Extending the Voltage Window of the FCG/AC Composites

The capacitive behavior of the FCG/AC composite electrode further improves when the voltage window is extended to 2.7 volts. The rectangular shape of the CV at 100 mV/s shows that the FCG/AC composite is stable at 2.7 V and also maintains an ideal capacitive behavior (Figure 4.6). The capacitance of the FCG/AC composite supercapacitor operated between a 2.7 V window is 124 F/g/electrode and 17 F/cm^3/electrode. Calculations were made based on industry protocols in order to be more realistic for real consumer usage (see Experimental Section 4.4.4). FCG/AC has a specific ESR of 7.4 ohm•cm^2.

4.2.4 Increase in Capacitance with Thicker FCG/AC Electrodes

The FCG/AC composite electrodes can be tuned by casting different thicknesses of the electrode material, thus giving different overall capacitances. The capacitive behaviors of the FCG/AC films with thicknesses of 44, 53, and 93 μm were compared at the 2.7 V window. Thicker films of FCG/AC resulted in supercapacitor devices with higher capacitance, as can be witnessed from the increase in current achieved for thicker FCG/AC films in the CV plot (Figure 4.7). However, the frequency response is also larger for the thicker FCG/AC electrodes. The capacitances and frequency responses of the FCG/AC devices measured at 2.7 V window with electrode active material thicknesses of 44 μm is 126 mF and 0.59 s, of 53 μm is 164 mF and 0.94 s, and of 93 μm is 212 mF and 1.33 s (Table 4.1).

4.3 Conclusions

Flash converted graphene composited with activated carbon particles showed improved EC performance. FCG sheets act to connect the AC particles to each other and to the current collector, thus, forming a faster electron transport network. The FCG/AC composite was made into a uniform film by mixing via probe sonication. The capacitance and energy of the FCG/AC composite electrodes are 113 F/g/electrode and 16 Wh/kg, which is higher than that of either the 100% AC or the 100% FCG electrodes. Furthermore, the capacitance (124 $F/g/_{electrode}$) of the FCG/AC composite is increased at 2.7 V. This FCG/AC composite is easily tuned for different thickness such as 44, 53, and 93 μm and, therefore can be tuned to meet the needs of a variety of different applications.

4.4 Experimental Section

4.4.1 Synthesis of FCG

Flash converted graphene (FCG) was synthesized in the lab using an Alien Bees B1600 flash lamp. A solution of 2.6% graphene oxide prepared via a modified Hummer's Method[23,24] was freeze-dried using a 1 L Labconco Freezone lyophilizer and then flash converted to FCG powder.

4.4.2 FCG/AC Composite Electrode Preparation

The FCG/AC composite was prepared from as-synthesized FCG powder, activated carbon (commercial) powder, a binder (carboxymethyl cellulose/styrene-butadiene rubber-CMC/SBR from MTI) in a ratio of 2:1:47, and 3 mL of water as the solvent. First, the FCG/AC composite was mixed in order to achieve homogeneity. In this study, several mixing parameters were investigated for its ability to homogenize the FCG/AC composite materials, such as bath sonication, probe sonication, and ball milling. The FCG/AC composite prepared via the bath sonication method was synthesized by stirring for 10 min, then bath sonicating for 99 min followed by 5 min of stirring. In the probe sonication method, the FCG/AC composite was stirred for 10 min, then probe sonicated for 60 min, then stirred for 5 min. For the ball mill method, the FCG/AC composite was synthesized by milling AC at 800 rpm for 15 min, then adding FCG into the slurry and milling again at 800 rpm for 15 min, then finally adding binder and ball milling at 800 rpm for 15 min. The milling process was carried out using a planetary ball mill with a single half inch stainless steel ball. After mixing the FCG/AC composite, the slurry was cast onto a carbon coated aluminum foil using a Guardco automatic drawdown machine II at the desired thicknesses (76, 127, 204 microns). The coated electrode films were allowed to dry in a 60 °C oven overnight.

4.4.3 FCG/AC Coin Cell Assembly

15 mm diameter electrode discs were punched from the dried FCG/AC films. The FCG/AC composite electrodes were assembled into coin cell supercapacitor devices with a 17 mm diameter polypropylene separator with 1.0 M $TEABF_4$ in acetonitrile as the electrolyte. The electrodes and separator were cut into circular discs using a McMaster-Carr round hole arch punch.

4.4.4 EC Testing and Analysis Using a Commercial 5 Step Protocol

All electrochemical measurements were collected from a Biologic VMP3 potentiostat and a VMP3b-10 booster. The coin cells were tested in a 4-point coin cell holder. All impedances were measured at 2 V from 1 MHz to 10 mHz.

Capacitances were calculated from the discharge curves of the constant current plots at 1 A/g from 0 to 2 V using Equation 4.1:

$$C = \frac{idt}{dV} \qquad \text{(Eq. 4.1)}$$

For measurements at 0 to 2.7 V, the analysis was done based on commercial calculation protocol to be more realistic to consumer uses. The capacitance was calculated from constant current discharge curves at a reasonable operating current. The self-discharge exhibited when using a supercapacitor device in real applications was also accounted for.

The time constants were calculated from the inverse frequency at -45° in the Bode Plot.

4.4.5 Morphological Characterizations of FCG/AC Composite Electrodes

The morphology of the FCG/AC electrodes was investigated under SEM using a FEI Nova 230 Nano SEM.

4.5 Tables and Figures

Table 4.1 Trend in Capacitance and Frequency Response with Different Thicknesses of FCG/AC Electrode

Thickness-active material one electrode (μm)	Capacitance (mF)	Frequency Response (s)
44	126	0.59
53	164	0.94
93	212	1.33

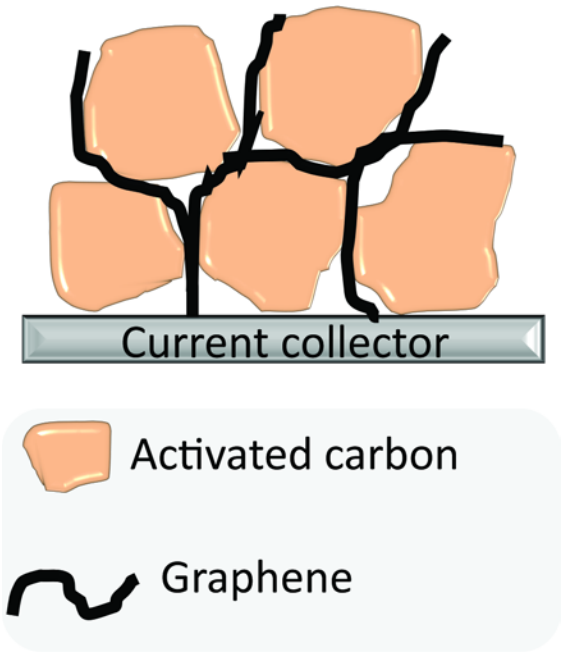

Figure 4.1 Graphene sheets partially wrap around activated carbon particles to connect the particles to each other and to the current collector. The graphene sheets act as an electron highway allowing for more effective charge transport in the electrode active material.

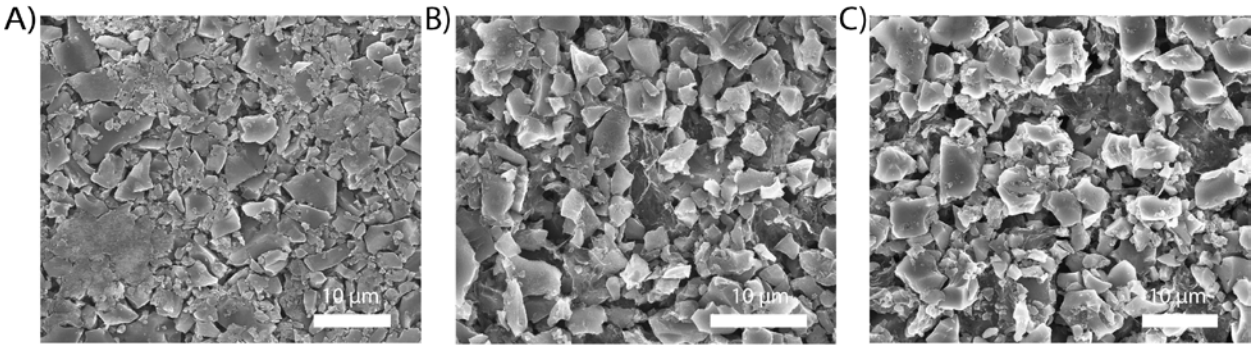

Figure 4.2 SEM images showing uniformity of FCG sheets and AC particles. The FCG/AC electrode films prepared using a) a bath sonication method, b) a ball milling method, and c) a probe sonication method.

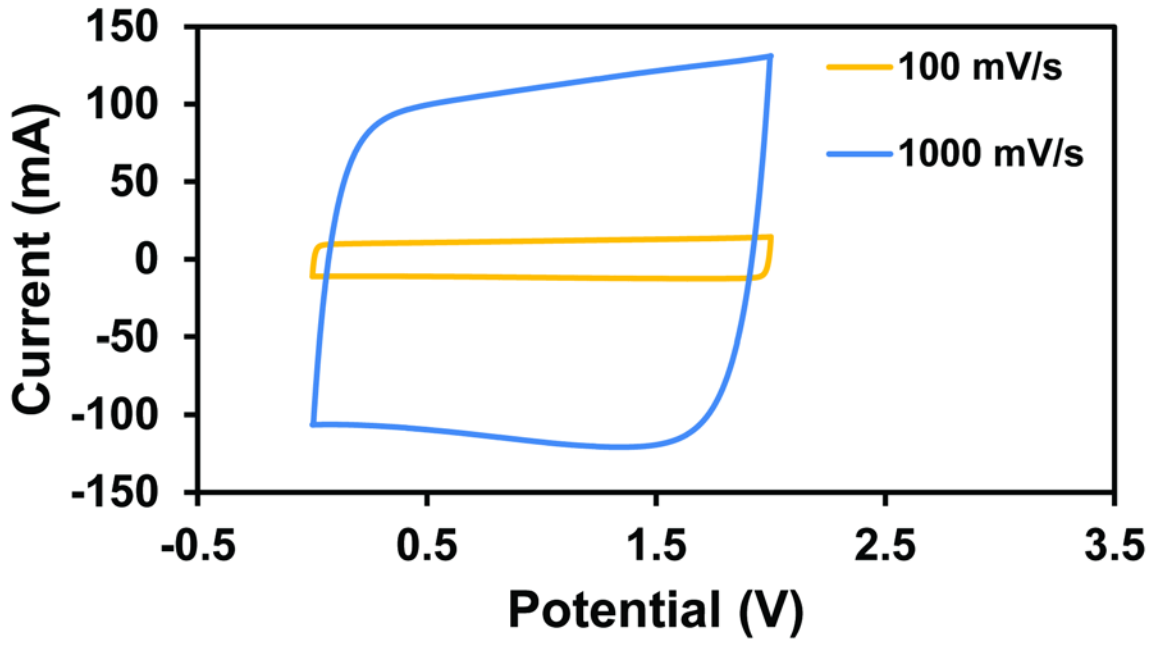

Figure 4.3 The rectangular shape, even at high scan rates of 1000 mV/s, shown in the cyclic voltammetry curves of FCG/AC device indicates the close to ideal electric double layer capacitance behavior of the composite electrodes.

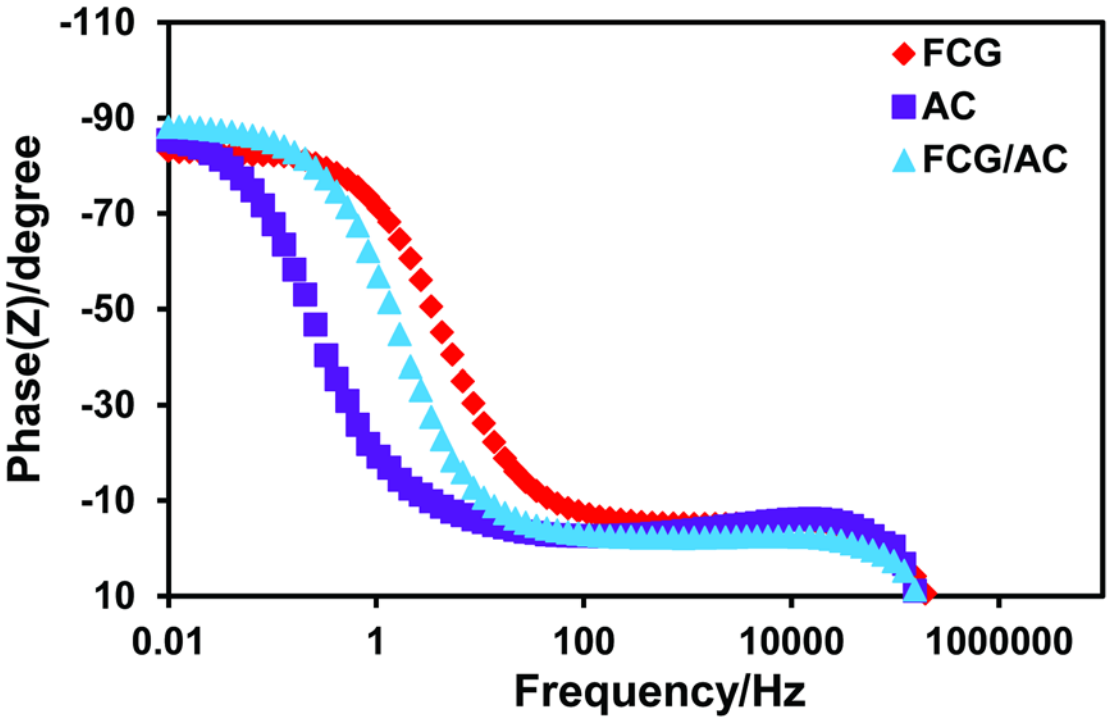

Figure 4.4 Bode plot of the FCG, AC, and FCG/AC devices for comparison. Electrochemical impedance spectroscopy taken from 1 MHz to 10 mHz at open circuit potential.

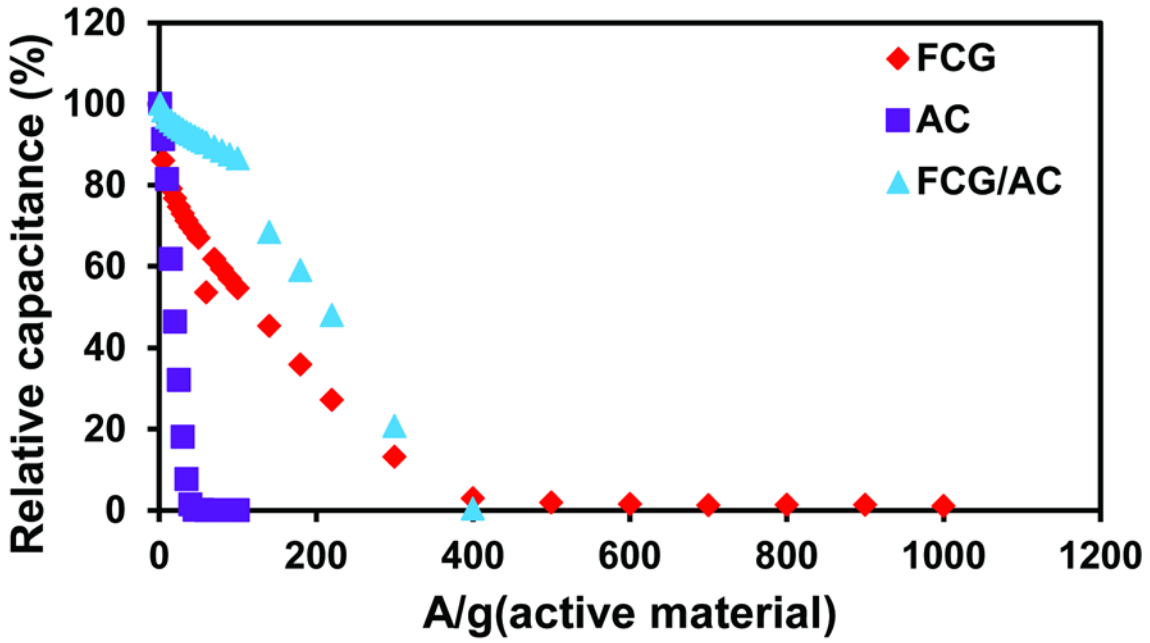

Figure 4.5 Comparison of the rate capability potential of the FCG, AC, and FCG/AC devices.

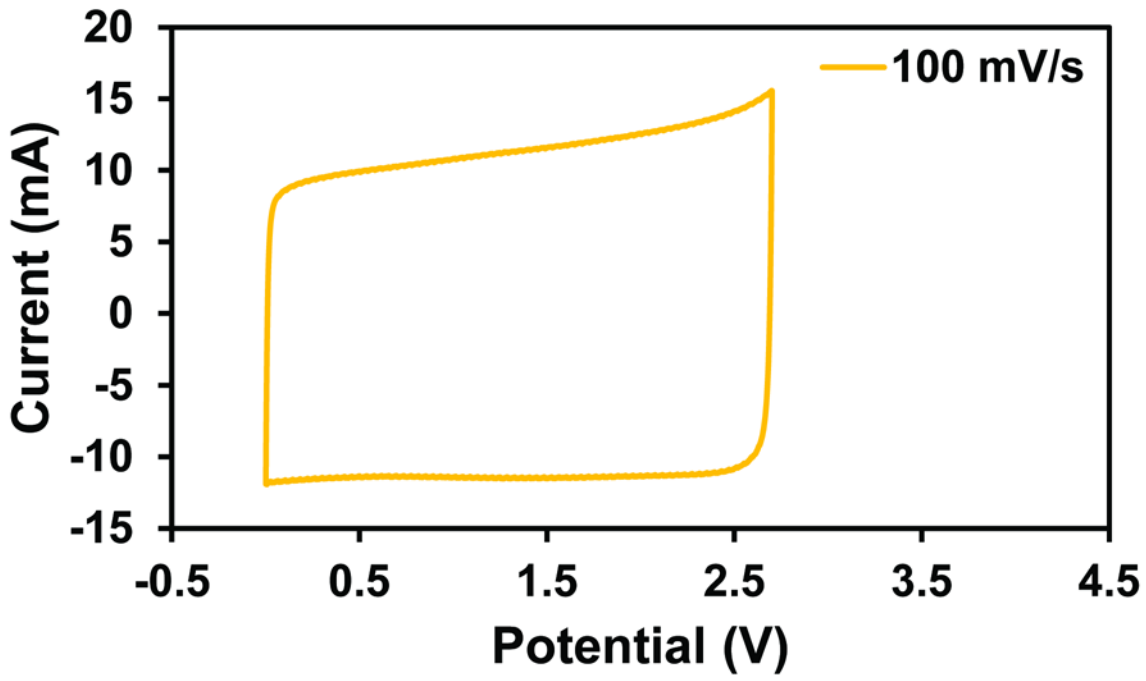

Figure 4.6 The operating voltage window of the FCG/AC device extended to 2.7 V, as shown from the cyclic voltammetry curve.

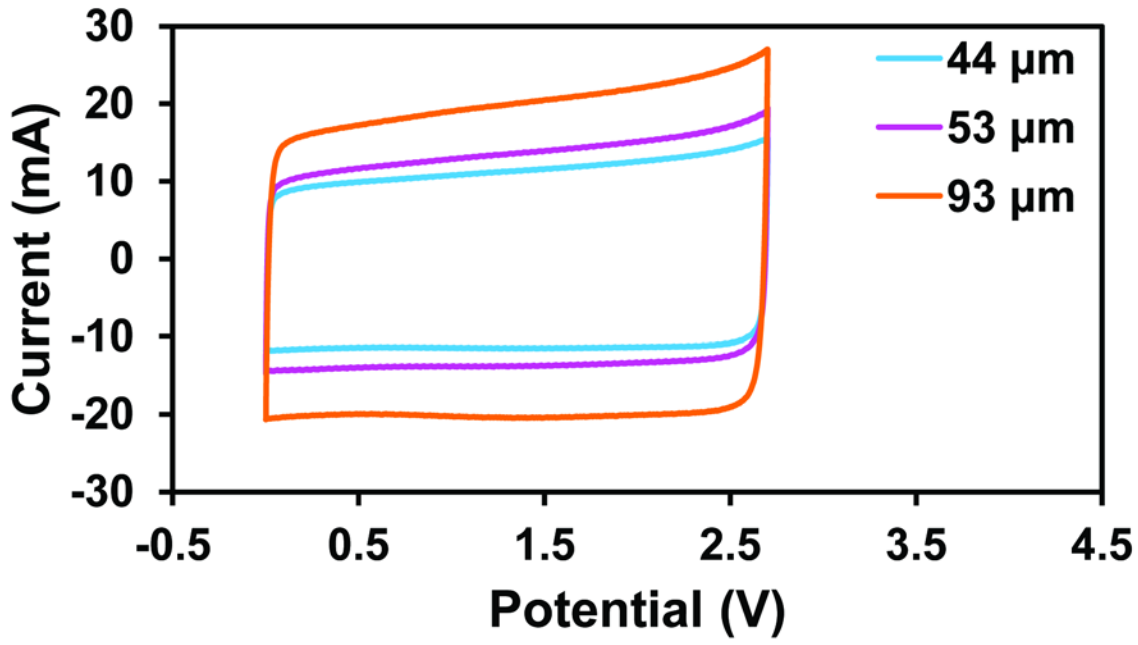

Figure 4.7 Cyclic voltammetry curves comparing the FCG/AC devices made from electrodes of different thicknesses.

4.6 References

1. Hall, P. J.; Bain, E. J. *Energy Policy* 2008, 36, 4352-4355.
2. Winter, M.; Brodd, R. J. *Chemical Reviews* 2004, 104, 4245-4270.
3. Chu, A.; Braatz, P. *Journal of Power Sources* 2002, 112, 236-246.
4. Baughman, R. H.; Zakhidov, A. A.; de Heer, W. A. *Science* 2002, 297, 787-792.
5. Simon, P.; Gogotsi, Y. *Nat Mater* 2008, 7, 845-854.
6. Laine, J.; Yunes, S. *Carbon* 1992, 30, 601-604.
7. Pandolfo, A. G.; Hollenkamp, A. F. *Journal of Power Sources* 2006, 157, 11-27.
8. Obreja, V. V. N. *Physica E: Low-dimensional Systems and Nanostructures* 2008, 40, 2596-2605.
9. Portet, C.; Taberna, P. L.; Simon, P.; Flahaut, E.; Laberty-Robert, C. *Electrochimica Acta* 2005, 50, 4174-4181.
10. Yan, J.; Fan, Z.; Wei, T.; Qian, W.; Zhang, M.; Wei, F. *Carbon* 2010, 48, 3825-3833.
11. Wang, G.; Zhang, L.; Zhang, J. *Chemical Society Reviews* 2012, 41, 797-828.
12. Peng, C.; Zhang, S.; Jewell, D.; Chen, G. Z. *Progress in Natural Science* 2008, 18, 777-788.
13. Stankovich, S.; Dikin, D. A.; Dommett, G. H. B.; Kohlhaas, K. M.; Zimney, E. J.; Stach, E. A.; Piner, R. D.; Nguyen, S. T.; Ruoff, R. S. *Nature* 2006, 442, 282-286.
14. Zhang, L. L.; Zhao, X. S. *Chemical Society Reviews* 2009, 38, 2520-2531.
15. Frackowiak, E. *Physical Chemistry Chemical Physics* 2007, 9, 1774-1785.
16. Geim, A. K.; Novoselov, K. S. *Nat Mater* 2007, 6, 183-191.

17. Meyer, J. C.; Geim, A. K.; Katsnelson, M. I.; Novoselov, K. S.; Booth, T. J.; Roth, S. *Nature* 2007, 446, 60-63.

18. Gilje, S.; Dubin, S.; Badakhshan, A.; Farrar, J.; Danczyk, S. A.; Kaner, R. B. *Advanced Materials* 2010, 22, 419-423.

19. Sircar, S.; Golden, T. C.; Rao, M. B. *Carbon* 1996, 34, 1-12.

20. Matranga, K. R.; Myers, A. L.; Glandt, E. D. *Chemical Engineering Science* 1992, 47, 1569-1579.

21. Wigmans, T. *Carbon* 1989, 27, 13-22.

22. Castro Neto, A. H.; Guinea, F.; Peres, N. M. R.; Novoselov, K. S.; Geim, A. K. *Reviews of Modern Physics* 2009, 81, 109-162.

23. Li, D.; Muller, M. B.; Gilje, S.; Kaner, R. B.; Wallace, G. G. *Nat. nanotechnol.* **2008**, 3, 101.

24. Dreyer, D. R.; Park, S.; Bielawski, C. W.; Ruoff, R. S. *Chem. Soc. Rev.* **2010**, 39, 228.

Chapter 5: Synthesis and Characterization of Metal-Organic Framework-74 Containing Two, Four, Six, Eight, and Ten Different Metals

Abstract

Metal-organic frameworks (MOFs) containing more than two kinds of metal ions mixed in one secondary building unit are rare because the synthesis often yields mixed MOF phases rather than a pure phase of a mixed-metal MOF (MM-MOF). In this study, we use a one-pot reaction to make microcrystalline MOF-74 [M_2(DOT); DOT = dioxidoterephthalate] with two (Mg, Co), four (Mg, Co, Ni, Zn), six (Mg, Sr, Mn, Co, Ni, Zn), eight (Mg, Ca, Sr, Mn, Fe, Co, Ni, Zn), and ten (Mg, Ca, Sr, Ba, Mn, Fe, Co, Ni, Zn, Cd) different kinds of divalent metals. The powder X-ray diffraction patterns of MM-MOF-74 were identical to those of single metal MOF-74, and no amorphous phases were found by scanning electron microscopy. Successful preparation of guest free MM-MOF-74 samples was confirmed by N_2 adsorption measurements. Elemental analysis data also support the fact that all metal ions used in the MOF synthesis are incorporated within the same MOF-74 structure. Energy-dispersive X-ray spectroscopies indicate that metal ions are heterogeneously distributed within each of the crystalline particles. This approach is also employed to incorporate metal ions (i.e. Ca, Sr, Ba, and Cd) from which the parent MOF structure could not be made as a single metal containing MOF.

5.1 Introduction

Metal-organic frameworks (MOFs) are well-known for the diversity in their chemical composition and connectivity of their underlying constituent organic and inorganic secondary

building units (SBUs).[1] Progress in the field over the past decade, has led to reports of >6000 unique MOF structures. MOFs' interior can also be tailored by both pre- and post-synthetic functionalization of organic linkers; further expanding the scope of this chemistry.[2] Recently, we have reported the synthesis and characterization of a multivariate (MTV) MOF, where a MOF-5 framework was made with multiple organic functionalities.[3] In this structure, up to eight organic functionalities are incorporated into MOF-5 without phase separation. Interestingly, these MOFs showed higher hydrogen and carbon dioxide uptake capacities compared with the unfunctionalized MOF-5.[3] After the discovery of this unique phenomenon, we sought to extend the concept of MTV-MOFs to include the incorporation of several metal ions within one structure to make mixed metal MOFs (MM-MOFs).[4] Herein, we report the synthesis and characterization of five isostructural, single-phase MOF-74 structures having two (Mg, Co), four (Mg, Co, Ni, Zn), six (Mg, Sr, Mn, Co, Ni, Zn), eight (Mg, Ca, Sr, Mn, Fe, Co, Ni, Zn), and ten (Mg, Ca, Sr, Ba, Mn, Fe, Co, Ni, Zn, Cd) divalentmetals, respectively (Figure 5.1, Figure 5.2). These materials were characterized by powder X-ray diffraction (PXRD), inductively coupled plasma optical emission and energy-dispersive X-ray spectroscopies (ICP-OES and EDS), scanning electron microscopy (SEM), and N_2 adsorption measurements. The results demonstrate that MM-MOF-74, of varying metal composition containing up to 10 different metal ions, is obtained through a one-pot solvothermal reaction with good reproducibility, and that this approach can be employed to incorporate metal ions (i.e. Ca, Sr, Ba, and Cd) from which the parent MOF structure remains unknown.

5.2 Results and Discussion

It is known that the equivalent Zn-MOF-74 [Zn_2(DOT); DOT = 2,5-dioxidoterephthalate][5,6] structure can be made using many different (but unmixed) divalent metal ions (M (II) = Mg,[7] Ni,[8] Co,[9] Fe,[10] Mn,[11] and Cu[12]). The MOF-74 structure is composed of infinite rods $M_3O_3(CO_2)_3$ and DOT linkers, where each metal ion is coordinated to three carboxyl, two hydroxyl groups and a coordinated ligand (DMF or water).[5] These characteristics provide evidence that MOF-74 is a logical system to expand the MTV concept of incorporating multiple metals, with a wide range of ionic radii sizes, within a single SBU of a pure phase of MOF-74.

Crystalline samples of the entire series of MM-MOF-74 (M2M-, M4M-, M6M-, M8M-, M10M-MOF-74, where the number indicates the number of metal ions incorporated within the respective MM-MOFs) were obtained through a solvothermal reaction. H_4DOT and selected metal salts (nitrate salts of Mg, Ca, Sr, Ba, Mn, Co, Ni, and Zn, and acetate salts of Fe and Cd) were dissolved in a solvent mixture of *N*,*N*-dimethylformamide (DMF), ethanol, and water (10:0.6:0.6, *v*/*v*). The solvent mixture was placed in a vial and heated at 120 °C for 20-24 h.[13-15] M2M-, M4M-, and M6M-MOF-74 samples are obtained in the form of prismatic crystals, whose size ranged from 5 to 50 micrometers. M8M- and M10M-MOF-74 appear in the form of sub-micrometer size particles.

Guest free materials were prepared prior to the detailed characterization because any contamination by unreacted metal salts (residing in the pores) can affect the results of the metal analysis. Therefore, the as-synthesized MM-MOF-74 materials were washed five times with 15

mL of DMF, exchanged twelve times with 15 mL of anhydrous methanol, and then evacuated at room temperature. Dried samples were then heated at 250 °C to remove coordinated methanol.[16] As discussed below the porosity of these phases indicates the absence of any metal complexes in the pores.

The crystallinity of the MM-MOF-74 series was confirmed by PXRD analysis (Figure 5.3). All PXRD patterns of MM-MOF-74 series coincide with the calculated PXRD pattern of the parent MOF-74 structure, indicating that the topology is retained and thus, all members are isostructural. To exclude the possibility of contamination by an amorphous phase in this sample, SEM observation was performed (Figures 5.4-5.8). The SEM image of MM-MOF-74 samples display homogenous nano-crystallites aggregated in clusters with no other morphology present.[17]

measurements. The porosity of the MM-MOF-74 materials was evaluated by N_2 adsorption at 77 K (Figure 5.9). The presence of guest molecules within the pores was also excluded by gas adsorption of the N_2 isotherm for all activated MM- MOF-74 is classified as a typical Type I isotherm, in which the Langmuir (BET) surface areas of M2M-, M4M-, M6M-, M8M-, and M10M-MOF-74 were calculated to be 1,310 (1,200), 1,040 (900), 1,240 (1,100), 1,210 (1,070), and 1,280 (1,140) m^2/g, respectively. The surface area values for the MM-MOF-74 are slightly lower than that for Mg-MOF-74 [1,490 (1,350) m^2/g], as it is 20-30% lighter than the MM-MOF-74. Nevertheless, the porosity measurement data clearly supports the fact that the MOF pores were successfully activated and guest molecules, including free metal ions, were removed.

The amounts of metals in the activated MM-MOF-74 materials was analyzed using ICP-OES.[15] When the results were normalized to 1.00 for Mg, the averaged normalized metal ratio and corresponding standard deviations for M10M-MOF-74 were calculated to be: Mg, 1.00; Ca, 0.08±0.02; Sr, 0.11±0.01; Ba, 0.28±0.04; Mn, 0.87±0.06; Fe, 1.57±0.34; Co, 1.01±0.11; Ni, 1.05±0.04; Zn, 0.74±0.04; Cd, 0.73±0.09. The small standard deviations indicate that the synthesis of the MM-MOFs is reproducible. From the ICP-OES data, an empirical formula of the M10M-MOF-74 is described as $Mg_{0.269}Ca_{0.022}Sr_{0.030}Ba_{0.075}Mn_{0.234}Fe_{0.422}Co_{0.272}Ni_{0.282}Zn_{0.199}Cd_{0.196}(DOT)\cdot(H_2O)_{7.8}$.[18] As expected, ICP-OES data also demonstrate that M2M-, M4M-, M6M-, and M8M-MOF-74 samples contain all metal ions added to the reaction mixture (Table 5.1). There is a trend that the observed amounts of Ca, Sr, and Ba ions are less than the other metal ions (Mg, Mn, Fe, Co, Ni, Zn, Cd), although the starting molar ratio of metal ions remained the same. This is most likely a result of Ca, Sr, and Ba ions being capable of easily taking the coordination number of eight rather than six. However, it is to be noted that the final molar ratio of the metal ions is affected by many factors, such as reactivity, solubility and coordination sphere of metal ions, and pH of the reaction mixture.

5.3 Conclusions

The data presented above indicate that mixing different kinds of metal ions in a one pot MOF synthesis can form MM-MOF-74. Considering that each metal ion should have different crystal growth rate, there is a possibility that metal ions are heterogeneously distributed in microcrystalline sample, resulting in the deviation of metal ratio in microenvironment. To

investigate the distribution of metal ions in micrometer resolution, SEM and EDS analyses were carried out using for M2M-, M4M-, M6M-, and M10M-MOF-74 samples.[15] As an illustrative example, the mapping data for M10M-MOF-74 is shown in Figure 5.10A. EDS mapping of each element in a sample of M10M-MOF-74 shows that all metals are spread out within the area of the crystalline particles. This clearly demonstrates the presence of all ten metals in M10M-MOF-74 microcrystalline sample. The SEM and EDS map of micro-size crystal particles for M2M-, M4M-, and M6M-MOF-74 also show the presence of all expected metal ions;[15] indicating that the samples are not a physical mixture of several different kinds of metal MOF-74 compounds.

To assess the metal distribution at the micrometer scale, EDS analysis of M10M-MOF-74 was performed on three distinct regions of the same sample (Figure 5.10B). The data show the presence of all 10 metals, and a non-negligible degree of deviation was observed. Similar deviation was observed for other MM-MOF-74 samples.[15] If each MM-MOF-74 crystal has the same homogeneous distribution of metals, then the EDS data would show similar metal values for several different regions or crystals of the materials. However, the EDS results implied a different scenario; it is highly likely that each MM-MOF-74 crystal contains all the metals expected but with each crystal having a different distribution of the metals.

5.4 Experimental Section

5.4.1 General Procedure for Preparing MM-MOF-74 Compounds:

2,5-Dihydroxyterephthalic acid (H_4DOT), cobalt nitrate hexahydrate [$Co(NO_3)_2{\cdot}6H_2O$], magnesium nitrate hexahydrate [$Mg(NO_3)_2{\cdot}6H_2O$], nickel nitrate hexahydrate [$Ni(NO_3)_2{\cdot}6H_2O$], zinc nitrate hexahydrate [$Zn(NO_3)_2{\cdot}6H_2O$], manganese nitrate tetrahydrate [$Mn(NO_3)_2{\cdot}4H_2O$],

strontium nitrate [$Sr(NO_3)_2$], iron acetate [$Fe(OAc)_2$], calcium nitrate tetrahydrate [$Ca(NO_3)_2 \cdot 4H_2O$], barium nitrate [$Ba(NO_3)_2$], and cadmium acetate dihydrate [$Cd(OAc)_2 \cdot 2H_2O$], *N*,*N*-dimethylformamide (DMF), ethanol (EtOH), and methanol (MeOH) were purchased from Aldrich Chemical Co.

MM-MOF-74 compounds were synthesized using varying amounts of metal salts combined with H_4DOT. The solid reagents were then dissolved in DMF/EtOH/water (in a 15:1:1 ratio respectively) and heated to 120 °C for 20-24 hours. The resulting crystals were soaked and washed, first with 75 mL of fresh DMF solvent for 5 exchanges over a 3 day period, and then with 180 mL of anhydrous MeOH for 12 exchanges over a 4 day period. The porous MOF compounds were then activated to remove all solvent by evacuating under vacuum (100-200 mTorr) overnight, and then heating stepwise under vacuum at 4 °C/min to 80 °C and held at that temperature for 1 h, then at 4 °C/min to 100 °C and held for 1 h, then at 4 °C/min to 150 °C and held for 1 h, then at 4 °C/min to 200 °C and held for 1 h, and lastly at 4 °C/min to 250 °C held for 10 h (30 mTorr). Synthesis of each MM-MOF-74 compound was repeated three separate times. The PXRD pattern of each sample was checked to match the simulated MOF-74 powder pattern. The metal values were recorded by inductively coupled plasma optical emission (ICP-OES) spectroscopy. The averaged values for the three experiments for each compound is reported with standard errors in Table 5.1.

5.4.2 Elemental Analysis of MM-MOF-74 Compounds

All measurements for the analysis of carbon, hydrogen, and nitrogen were taken on a Thermo (Carlo Erba) Flash EA112 Combustion CHNS analyzer using 2–3 mg of a MM-MOF-74 sample.

Metal detection for all samples was carried out on a TJA radial IRIS 1000 ICP-OES spectroscope with a charge injection device array of 512 × 512 pixels of a continuous wavelength detector. All solid samples (0.5-1 mg) were first digested using 200 microliters of fuming nitric acid purchased from Aldrich Chemical Co., and then the samples were diluted with 2% nitric acid to a total volume of 10 mL in a volumetric flask. The solutions were then transferred to low density polyethylene tubes purchased from Fisher Scientific International Inc. The solution, 2% nitric acid in water, was prepared by using fuming nitric acid purchased from Aldrich Chemical Co. and ultrapure water. The solid MOF samples immediately dissolved upon treatment with 2% nitric acid. All glassware for ICP-OES was rinsed thoroughly for a minimum of five times with ultrapure water. Standards were prepared from Inorganic Ventures' multi-element standard solutions of Mg, Ca, Sr, Ba, Mn, Fe, Co, Ni, Zn, and Cd. R.F. power was 1150 watts, auxiliary flow was 0.5 L/min, nebulizer flow was 32.06 psi, pump rate was 70 rpm, CID temperature was -41 °C, and the FPA temperature was 28.3 °C.

Relative amounts (moles) of metals in the empirical formula were determined from experimental weight percent values. The linker, DOT, has a total anionic charge of four, with a minus charge on each carboxylate group and a minus charge on each hydroxyl group. Charge balance was achieved by assuming all metals were divalent and constraining the total moles of metals to 1.0. The empirical equations were then fit by varying the number of water molecules.

5.4.3 Powder X-ray Diffraction Analysis of MM-MOF-74 Compounds

All PXRD patterns were collected with a Bruker AXS D8 Advance diffractometer at 40 kV, 40 mA using Cu K_α radiation (λ = 1.5406 Å). The PXRD pattern for each compound was compared to a simulated MOF-74 PXRD pattern. The simulated MOF-74 PXRD pattern was calculated using the software Powder Cell v. 2.2. This procedure has been described in previous publications.[19]

5.4.4 Synthesis of MM-MOF-74:

(Mg, Co) M2M-MOF-74, $Mg_{0.428}Co_{1.572}(DOT)\cdot(H_2O)_{8.2}$:

H_4DOT (30 mg, 1.5 × 10^{-4} mol), $Mg(NO_3)_2\cdot6H_2O$ (58.2 mg, 2.27 × 10^{-4} mol), $Co(NO_3)_2\cdot6H_2O$ (66.1 mg, 2.27 × 10^{-4} mol) were sonicated and dissolved in 10 mL DMF, 0.6 mL EtOH, and 0.6 mL H_2O in a 20-mL scintillation vial. The vial was sealed tightly and placed in an isothermal oven at 120 °C for 20 h for the completion of the solvothermal reaction. The resulting as-synthesized product is a red microcrystalline powder. Different sizes of rod shaped single crystals and aggregates were seen under an optical microscope. The PXRD pattern of the synthesized compound matches the simulated MOF-74 powder diffraction pattern. Elemental Analysis (activated): Calculated for $Mg_{0.428}Co_{1.572}C_8H_{18.4}O_{14.2}$ = $Mg_{0.428}Co_{1.572}(DOT)\cdot(H_2O)_{8.2}$: C, 21.60; H, 4.17; N, 0.00; Found (%): C, 21.18; H, 4.12; N, <0.1.

(Mg, Co, Ni, Zn) M4M-MOF-74, $Mg_{0.190}Co_{0.612}Ni_{0.562}Zn_{0.636}(DOT)\cdot(H_2O)_{8.4}$:

H_4DOT (30 mg, 1.5 × 10^{-4} mol), $Mg(NO_3)_2\cdot6H_2O$ (30.7 mg, 1.20 × 10^{-4} mol), $Co(NO_3)_2\cdot6H_2O$ (34.9 mg, 1.20 × 10^{-4} mol), $Ni(NO_3)_2\cdot6H_2O$ (34.9 mg, 1.20 × 10^{-4} mol), $Zn(NO_3)_2\cdot6H_2O$ (35.7 mg, 1.20 × 10^{-4} mol) were sonicated and dissolved in 10 mL DMF, 0.6 mL

EtOH, and 0.6 mL H_2O in a 20-mL scintillation vial. The vial was sealed tightly and placed in an isothermal oven at 120 °C for 24 h for the completion of the solvothermal reaction. The resulting as-synthesized product is an orange microcrystalline powder. Different sizes of rod shaped single crystals and aggregates were seen under an optical microscope. The PXRD pattern of the synthesized compound matches the simulated MOF-74 powder diffraction pattern. Elemental Analysis (activated): Calculated for $Mg_{0.190}Co_{0.612}Ni_{0.562}Zn_{0.636}C_8H_{18.8}O_{14.4}$ = $Mg_{0.190}Co_{0.612}Ni_{0.562}Zn_{0.636}(DOT)\cdot(H_2O)_{8.4}$ (%): C, 20.86; H, 4.11; N, 0.00; Found (%): C, 20.37; H, 3.72; N, <0.1.

(Mg, Sr, Mn, Co, Ni, Zn) M6M-MOF-74, $Mg_{0.124}Sr_{0.004}Mn_{0.212}Co_{0.592}Ni_{0.528}Zn_{0.540}(DOT)\cdot(H_2O)_{8.2}$:

H_4DOT (30 mg, 1.5×10^{-4} mol), $Mg(NO_3)_2\cdot 6H_2O$ (25.6 mg, 9.98×10^{-5} mol), $Sr(NO_3)_2$ (21.2 mg, 1.00×10^{-4} mol), $Mn(NO_3)_2\cdot 4H_2O$ (25.1 mg, 1.00×10^{-4} mol), $Co(NO_3)_2\cdot 6H_2O$ (29.1 mg, 1.00×10^{-4} mol), $Ni(NO_3)_2\cdot 6H_2O$ (29.1 mg, 1.00×10^{-4} mol), $Zn(NO_3)_2\cdot 6H_2O$ (29.7 mg, 9.98×10^{-5} mol) were sonicated and dissolved in 10 mL DMF, 0.6 mL EtOH, and 0.6 mL H_2O in a 20-mL scintillation vial. The vial was sealed tightly and placed in an isothermal oven at 120 °C for 22 h for the completion of the solvothermal reaction. The resulting as-synthesized product is a green-black microcrystalline powder. Crystals were too small to be seen under an optical microscope. The PXRD pattern of the synthesized compound matches the simulated MOF-74 powder diffraction pattern. Elemental Analysis (activated): Calculated for $Mg_{0.124}Sr_{0.004}Mn_{0.212}Co_{0.592}Ni_{0.528}Zn_{0.540}C_8H_{18.4}O_{14.2}$ = $Mg_{0.124}Sr_{0.004}Mn_{0.212}Co_{0.592}Ni_{0.528}Zn_{0.540}(DOT)\cdot(H_2O)_{8.2}$ (%): C, 20.98; H, 4.05; N, 0.00; Found (%): C, 20.89; H, 3.61; N, <0.1.

(Mg, Ca, Sr, Mn, Fe, Co, Ni, Zn) M8M-MOF-74,

$Mg_{0.268}Ca_{0.034}Sr_{0.048}Mn_{0.258}Fe_{0.314}Co_{0.432}Ni_{0.392}Zn_{0.254}(DOT)\cdot(H_2O)_{8.2}$:

H_4DOT (30 mg, 1.5 × 10^{-4} mol), $Mg(NO_3)_2\cdot 6H_2O$ (14.6 mg, 5.69 × 10^{-5} mol), $Ca(NO_3)_2\cdot 4H_2O$ (13.5 mg, 5.72 × 10^{-5} mol), $Sr(NO_3)_2$ (12.1 mg, 5.72 × 10^{-5} mol), $Mn(NO_3)_2\cdot 4H_2O$ (14.3 mg, 5.70 × 10^{-5} mol), $Fe(OAc)_2$ (9.9 mg, 5.7 × 10^{-5} mol), $Co(NO_3)_2\cdot 6H_2O$ (16.5 mg, 5.67 × 10^{-5} mol), $Ni(NO_3)_2\cdot 6H_2O$ (16.5 mg, 5.67 × 10^{-5} mol), $Zn(NO_3)_2\cdot 6H_2O$ (16.7 mg, 5.61 × 10^{-5} mol) were sonicated and dissolved in 10 mL DMF, 0.6 mL EtOH, and 0.6 mL H_2O in a 20-mL scintillation vial. The vial was sealed tightly and placed in an isothermal oven at 120 °C for 24 h for the completion of the solvothermal reaction. The resulting as-synthesized product is a black microcrystalline powder. Crystals were too small to be seen under an optical microscope. The PXRD pattern of the synthesized compound matches the simulated MOF-74 powder diffraction pattern. Elemental Analysis (activated): Calculated for $Mg_{0.268}Ca_{0.034}Sr_{0.048}Mn_{0.258}Fe_{0.314}Co_{0.432}Ni_{0.392}Zn_{0.254}C_8H_{18.4}O_{14.2}$ = $Mg_{0.268}Ca_{0.034}Sr_{0.048}Mn_{0.258}Fe_{0.314}\ Co_{0.432}Ni_{0.392}Zn_{0.254}(DOT)\cdot(H_2O)_{8.2}$ (%): C, 21.49; H, 4.06; N, 0.00; Found (%): C, 20.96; H, 4.12; N, <0.1.

(Mg, Ca, Sr, Ba, Mn, Fe, Co, Ni, Zn, Cd) M10M-MOF-74,

$Mg_{0.269}Ca_{0.022}\ Sr_{0.030}Ba_{0.075}Mn_{0.234}Fe_{0.422}Co_{0.272}Ni_{0.282}Zn_{0.199}Cd_{0.196}(DOT)\cdot(H_2O)_{7.8}$:

H_4DOT (30 mg, 1.5 × 10^{-4} mol), $Mg(NO_3)_2\cdot 6H_2O$ (11.6 mg, 4.52 × 10^{-5} mol), $Ca(NO_3)_2\cdot 4H_2O$ (10.6 mg, 4.49 × 10^{-5} mol), $Sr(NO_3)_2$ (9.6 mg, 4.5 × 10^{-5} mol), $Ba(NO_3)_2$ (11.8 mg, 4.52 × 10^{-5} mol), $Mn(NO_3)_2\cdot 4H_2O$ (11.3 mg, 4.50 × 10^{-5} mol), $Fe(OAc)_2$ (7.9 mg, 4.5 × 10^{-5} mol), $Co(NO_3)_2\cdot 6H_2O$ (13.2 mg, 4.54 × 10^{-5} mol), $Ni(NO_3)_2\cdot 6H_2O$ (13.2 mg, 4.54 × 10^{-5} mol),

$Zn(NO_3)_2 \cdot 6H_2O$ (13.4 mg, 4.50×10^{-5} mol), $Cd(OAc)_2 \cdot 2H_2O$ (12.0 mg, 4.50×10^{-5} mol) were sonicated and dissolved in 10 mL DMF, 0.6 mL EtOH, and 0.6 mL H_2O in a 20-mL scintillation vial. The vial was sealed tightly and placed in an isothermal oven at 120 °C for 24 h for the completion of the solvothermal reaction. The resulting as-synthesized product was a black microcrystalline powder. Crystals were too small to be seen under an optical microscope. The PXRD pattern of the synthesized compound matches the simulated MOF-74 powder diffraction pattern. Elemental Analysis (activated): Calculated for $Mg_{0.269}Ca_{0.022}Sr_{0.030}Ba_{0.075}Mn_{0.234}Fe_{0.422}Co_{0.272}Ni_{0.282}Zn_{0.199}Cd_{0.196}C_8H_{17.6}O_{13.8}$ = $Mg_{0.269}Ca_{0.022}Sr_{0.030}Ba_{0.075}Mn_{0.234}Fe_{0.422}\ Co_{0.272}Ni_{0.282}Zn_{0.199}Cd_{0.196}(DOT)\cdot(H_2O)_{7.8}$ (%): C, 20.93; H, 3.86; N, 0.00; Found (%): C, 21.41; H, 3.67; N, <0.1.

5.4.5 Scanning Electron Microscopy Imaging (SEM)

All MM-MOF-74 samples were prepared for SEM by dispersing the material onto a double sided adhesive conductive carbon tape that was attached to a flat aluminum sample holder. The samples were imaged at a working distance of 5-6 mm with accelerating voltage of 10 kV using a low vacuum detector (LVD) on an FEI Nova NanoSEM 230. Several samples of each MM-MOF-74 compound were imaged and compared. Multiple regions of each compound were seen to have crystalline material of the same morphology in varying sizes and aggregations.

5.4.6 N_2 Adsorption Measurements

The porosities of the M2M-, M4M-, M6M-, M8M-, and M10M-MOF-74 were investigated using a Quantachrome Autosorb-1 volumetric gas adsorption analyzer. All samples

were activated and loaded into the sample holder in an argon glovebox. The N_2 adsorption measurements were carried out at 77 K, using a liquid N_2 bath. Ultra-high-purity grade N_2 and He (99.999% purity) were used throughout the adsorption experiments.

5.4.7 X-ray Energy Dispersive Spectroscopy (EDS)

All MM-MOF-74 compounds for EDS were analyzed were prepared in the same way as for SEM in an FEI Nova NanoSEM 230 operated at 15 kV with Thermo Fisher Scientific Noran System Six Energy Dispersive X-ray Spectrometer. The metals were identified for localized regions using the point and shoot mode. The samples were all analyzed at several different areas that are not closely neighboring one another to get a survey of the metals in the sample. Mapping of the metals and oxygen for some of the compounds were also taken using spectral mapping mode.

5.5 Tables and Figures

Table 5.1. Ratio of Metals Found for MM-MOF-74 Crystals (bold) and Reaction Stoichiometry (parentheses).

MOF	Mg	Ca	Sr	Ba	Mn	Fe	Co	Ni	Zn	Cd
M2M-MOF-74	**1.0** (1)	n/a	n/a	n/a	n/a	n/a	**3.20 ±0.38** (1)	n/a	n/a	n/a
M4M-MOF-74	**1.0** (1)	n/a	n/a	n/a	n/a	n/a	**2.46±0.48** (1)	**2.30±0.42** (1)	**2.62±0.44** (1)	n/a
M6M-MOF-74	**1.0** (1)	n/a	**0.05±0.02** (1)	n/a	**1.62±0.06** (1)	n/a	**4.11±0.40** (1)	**3.97±0.20** (1)	**3.57±0.49** (1)	n/a
M8M-MOF-74	**1.0** (1)	**0.10±0.03** (1)	**0.16±0.04** (1)	n/a	**0.92±0.07** (1)	**1.07±0.13** (1)	**1.40±0.25** (1)	**1.38±0.18** (1)	**0.94±0.07** (1)	n/a
M10M-MOF-74	**1.0** (1)	**0.08±0.02** (1)	**0.11±0.01** (1)	**0.28±0.04** (1)	**0.87±0.06** (1)	**1.57±0.34** (1)	**1.01±0.11** (1)	**1.05±0.04** (1)	**0.74±0.04** (1)	**0.73±0.09** (1)

* The ratios for each metal in all five samples were normalized to the value of 1.0 for the metal Mg. n/a, not applicable

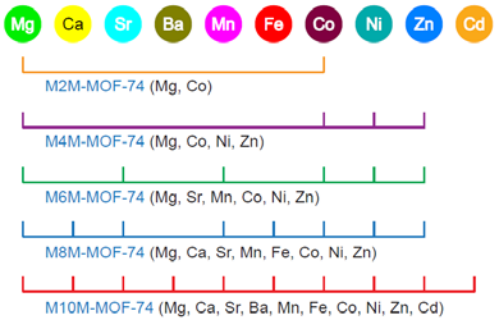

Figure 5.1 Combination of metal ions used to synthesize MM-MOF-74.

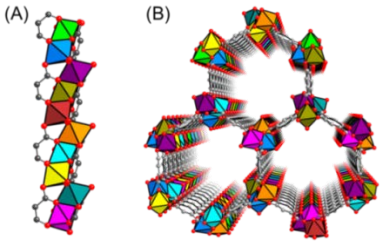

Figure 5.2 (A) Schematic illustration of the rod type inorganic SBU ($M_3O_3(CO_2)_3$; M = metal ions) present in a MM-MOF-74 structure. (B) The structure of MOF-74 is composed of infinite rod type SBUs allowing the incorporation of up to ten different metal ions in the same SBU. Gray and red spheres represent carbon and oxygen atoms. Polyhedra in various colors indicate the incorporation of different metal ions in one structure.

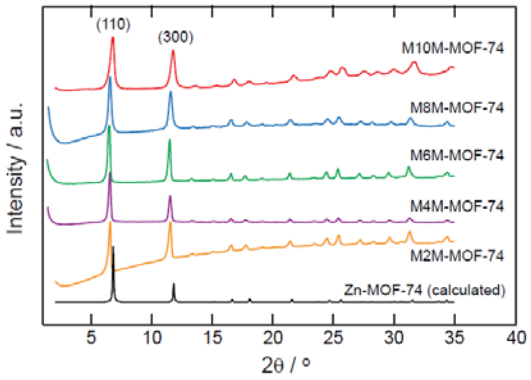

Figure 5.3 PXRD patterns of a series of MM-MOF-74. As a reference, calculated pattern of Zn-MOF-74 is overlaid.

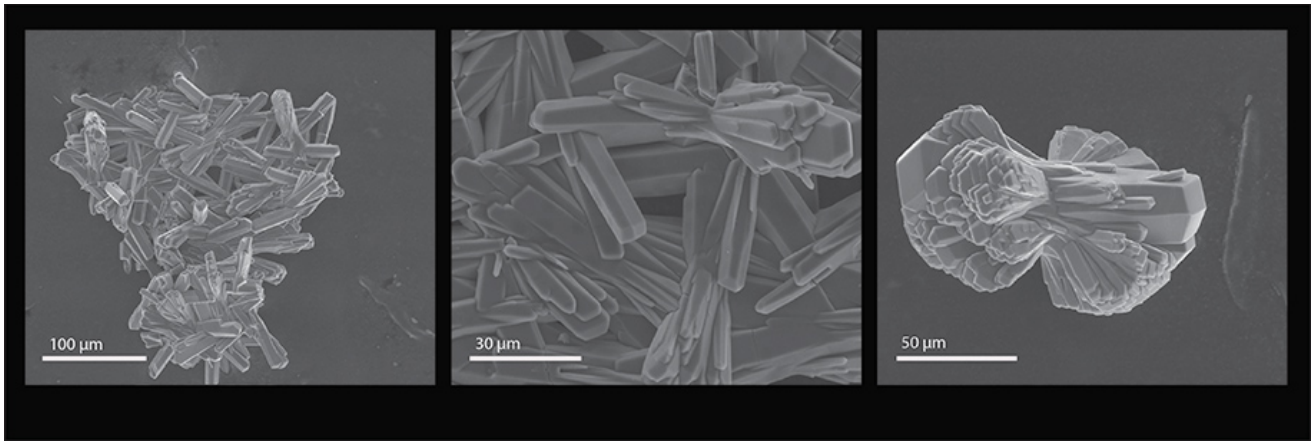

Figure 5.4 SEM images of M2M-MOF-74 at different magnifications showing single-phase morphology.

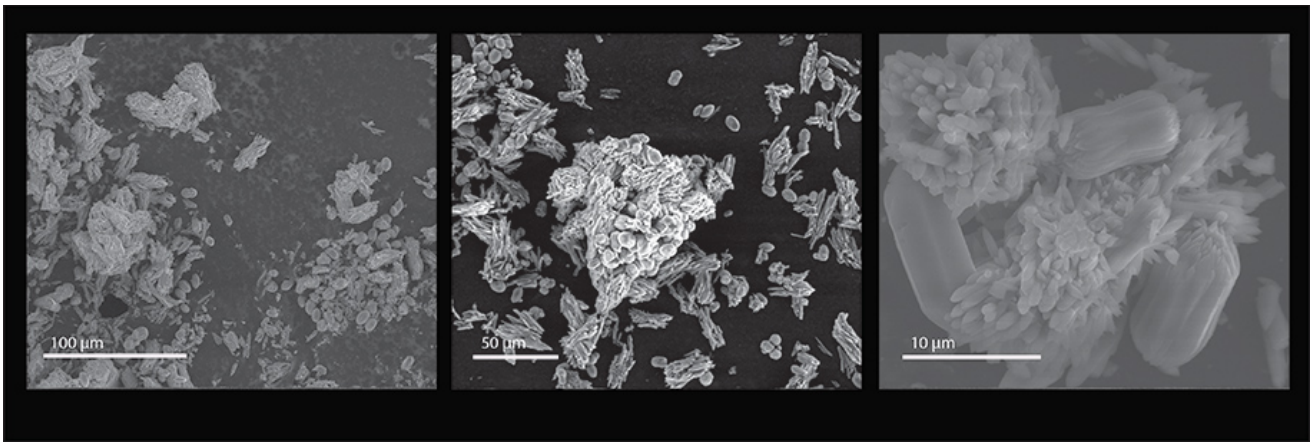

Figure 5.5 SEM images of M4M-MOF-74 at different magnifications showing single-phase morphology.

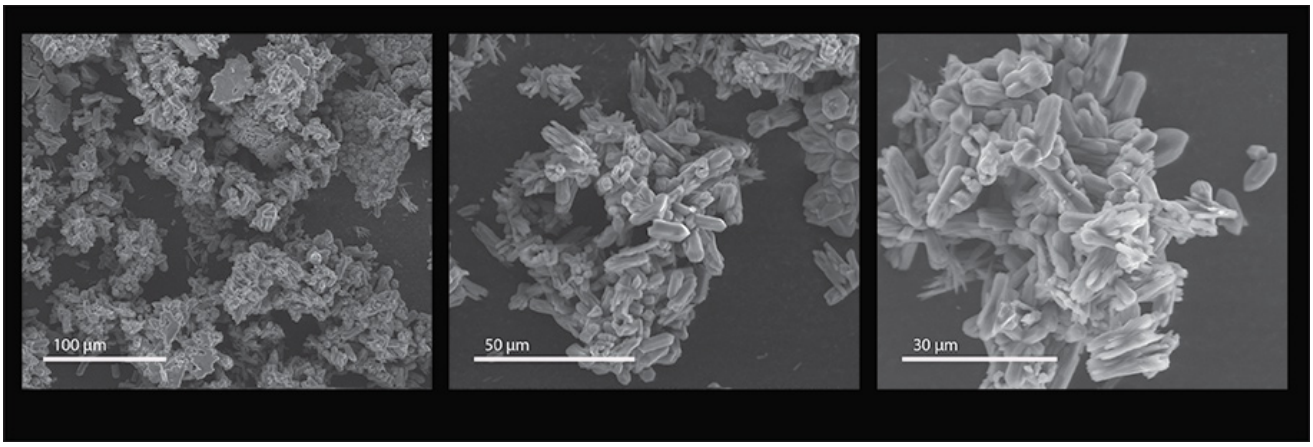

Figure 5.6 SEM images of M6M-MOF-74 at different magnifications showing single-phase morphology.

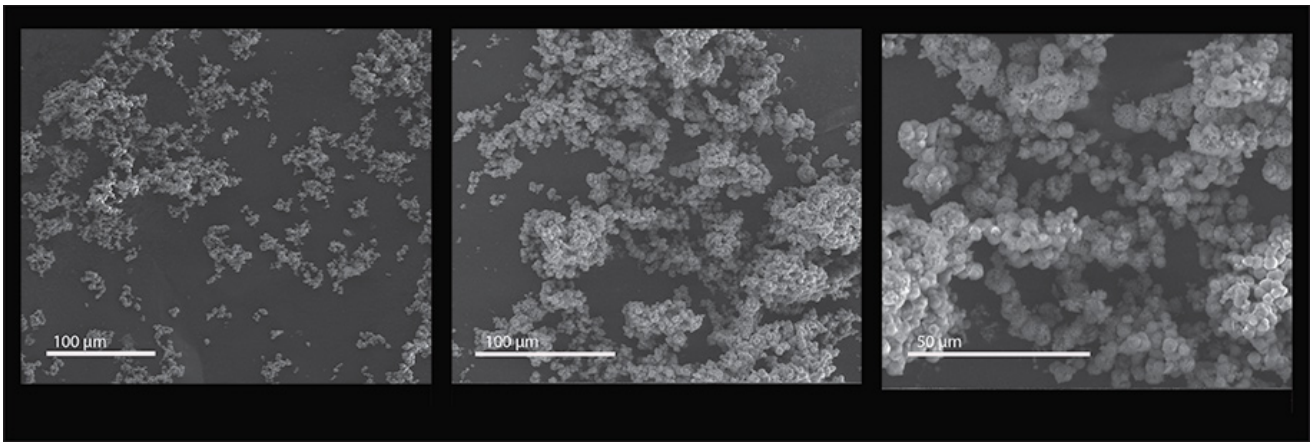

Figure 5.7 SEM images of M8M-MOF-74 at different magnifications showing single-phase morphology.

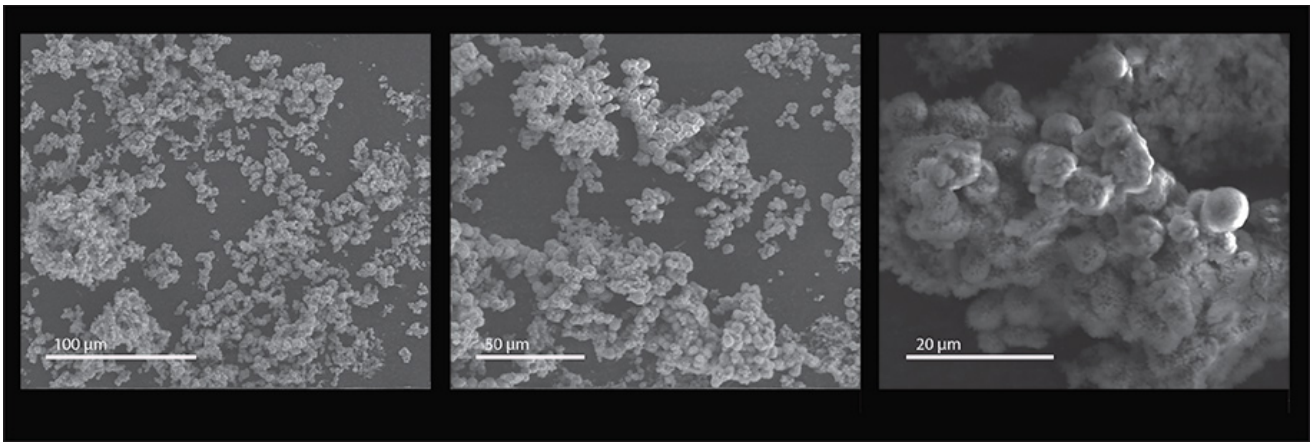

Figure 5.8 SEM images of M10M-MOF-74 at different magnifications showing single-phase morphology.

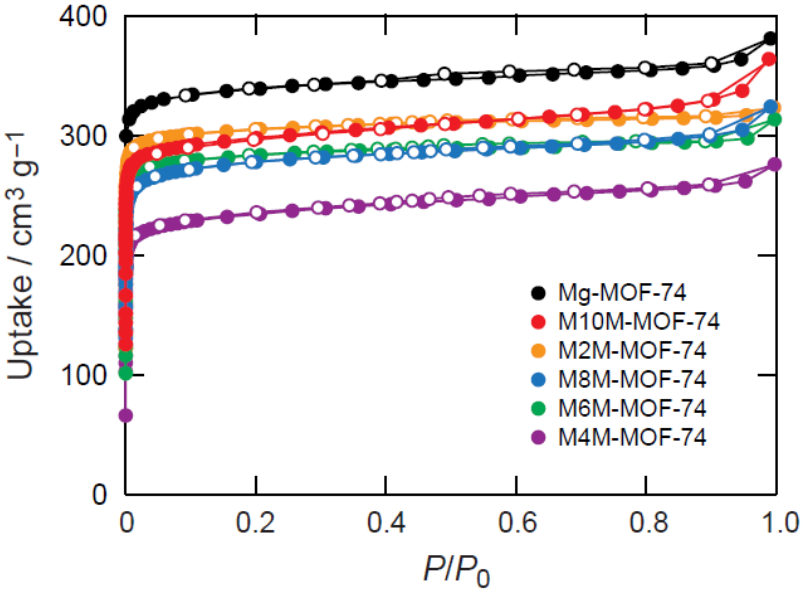

Figure 5.9 Nitrogen adsorption isotherms of a series of MM-MOF-74 measured at 77 K. As a reference, the isotherm of Mg-MOF-74 is overlaid.

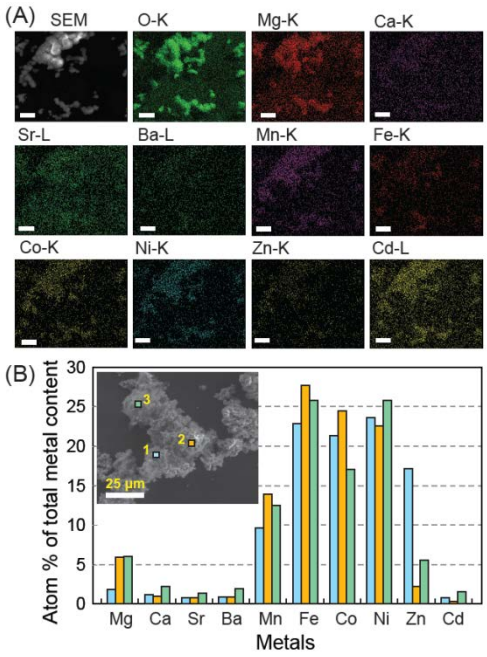

Figure 5.10 EDS analysis of M10M-MOF-74. (A) SEM image and EDS mapping of the same sample area demonstrating the presence of oxygen and each of the ten metals. Scale bars, 10 µm. (B) Ratio of metals found in three distinct regions of a different M10M-MOF-74 sample (indicated by different colors: blue, orange, and green). (Inset) SEM image indicating the specific region EDS was collected to quantify the ratio of metals present.

5.6 References and Notes

1. (a) Furukawa, H.; Cordova, K. E.; O'Keeffe, M.; Yaghi, O. M. *Science* 2013, *341*, 974; *Science* 2013, *341*, 1230444-1–1230444-12. (b) Kitagawa, S.; Kitaura, R.; Noro, S. *Angew. Chem. Int. Ed.* 2004, *43*, 2334–2375. (c) Liu, L.; Konstas, K.; Hill, M. R.; Telfer, S. G. *J. Am. Chem. Soc.* 2013, *135*, 17731–17734. (d) O'Keeffe, M.; Yaghi, O. M. *Chem. Rev.* 2012, *112*, 675–702. (e) Yaghi, O. M.; O'Keeffe, M.; Ockwig, N. W.; Chae, H. K.; Eddaoudi, M.; Kim, J. *Nature* 2003, *423*, 705–714.

2. (a) Wang, Z.; Cohen, S. M. *J. Am. Chem. Soc.* 2007, *129*, 12368–12369. (b) Wu, C.-D.; Hu, A.; Zhang, L.; Lin, W. *J. Am. Chem. Soc.* 2005, *127*, 8940–8941. (c) Morris, W.; Doonan, C. J.; Furukawa, H.; Banerjee, R.; Yaghi, O. M. *J. Am. Chem. Soc.* 2008, *130*, 12626–12627. (d) Morris, W.; Volosskiy, B.; Demir, S.; Gándara, F.; McGrier, P. L.; Furukawa, H.; Cascio, D.; Stoddart, J. F.; Yaghi, O. M. *Inorg. Chem.* 2012, *51*, 6443–6445.

3. (a) Deng, H.; Doonan, C. J.; Furukawa, H.; Ferreira, R. B.; Towne, J.; Knobler, C. B.; Wang, B.; Yaghi, O. M. *Science* 2010, 327, 846–850. (b) Kong, X.; Deng, H.; Yan, F.; Kim, J.; Swisher, J. A.; Smit, B.; Yaghi, O. M.; Reimer, J. A. *Science* 2013, *341*, 882–885.

4. (a) Brozek, C. K.; Dincă, M. *J. Am. Chem. Soc.* 2013, *135*, 12886–12891. (b) Kim, M.; Cahill, J. F.; Fei, H.; Prather, K. A.; Cohen, S. M. *J. Am. Chem. Soc.* 2012, *134*, 18082–18088. (c) Burrows, A. D. *CrystEngComm* 2011, *13*, 3623–3642. (d) Botas, J. A.; Calleja, G.; Sánchez-Sáchez, M.; Orcajo, M. G. *Int. J. Hydrogen Energy* 2011, *36*,

10834–10844. (e) Botas, J. A.; Calleja, G.; Sánchez-Sánchez, M.; Orcajo, M. G. *Langmuir* 2010, *26*, 5300–5303. (f) Cui, Y.; Xu, H.; Yue, Y.; Guo, Z.; Yu, J.; Chen, Z.; Gao, J.; Yang, Y.; Qian, G.; Chen, B. *J. Am. Chem. Soc.* 2012, *134*, 3979–3982. (g) Zeng, M.-H.; Wang, B.; Wang, X.-Y.; Zhang, W.-X.; Chen, X.-M.; Gao, S. *Inorg. Chem.* 2006, *45*, 7069–7076.

5. Rosi, N. L.; Kim, J.; Eddaoudi, M.; Chen, B.; O'Keeffe, M.; Yaghi, O. M. *J. Am. Chem. Soc*. 2005, *127*, 1504–1518.

6. Deng, H.; Grunder, S.; Cordova, K. E.; Valente, C.; Furukawa, H.; Hmadeh, M ; Gándara, F.; Whalley, A. C.; Liu, Z.; Asahina, S.; Kazumori, H.; O'Keeffe, M.; Terasaki, O.; Stoddart, J. F.; Yaghi, O. M. *Science* 2012, *336*, 1018–1023.

7. Dietzel, P. D. C.; Blom, R.; Fjellvåg, H. *Eur. J. Inorg. Chem.* 2008, 3624–3632.

8. Dietzel, P. D. C.; Panella, B.; Hirscher, M.; Blom, R.; Fjellvåg, H. *Chem. Commun.* 2006, 959–961.

9. Dietzel, P. D. C.; Morita, Y.; Blom, R.; Fjellvåg, H. *Angew. Chem. Int. Ed.* 2005, *44*, 6354–6358.

10. Bhattacharjee S.; Choi, J.-S.; Yang, S.-T.; Choi, S. B. Kim, J.; Ahn, W.-S. *J. Nanosci. Nanotech.* 2010, *10*, 135–141.

11. Zhou, W.; Wu, H.; Yildirim, T. *J. Am. Chem. Soc.* 2008, *130*, 15268–12529.

12. Sanz, R.; Martínez, F.; Orcajo, G.; Wojtas, L.; Briones, D. *Dalton Trans.* 2013, *42*, 2392–2398.

13. For example, M10M-MOF-74 was prepared by the following procedure: Equimolar amounts (ca. 4.5×10^{-5} mol) of ten different divalent metal salts [$Mg(NO_3)_2 \cdot 6H_2O$ (11.6 mg), $Ca(NO_3)_2 \cdot 4H_2O$ (10.6 mg), $Sr(NO_3)_2$ (9.6 mg), $Ba(NO_3)_2$ (11.8 mg), $Mn(NO_3)_2 \cdot 4H_2O$ (11.3 mg), $Fe(CO_2CH_3)_2$ (7.9 mg), $Co(NO_3)_2 \cdot 6H_2O$ (13.2 mg), $Ni(NO_3)_2 \cdot 6H_2O$ (13.2 mg), $Ni(NO_3)_2 \cdot 6H_2O$ (13.4 mg), and $Cd(CO_2CH_3)_2 \cdot 6H_2O$ (12.0 mg)] were dissolved with H_4DOT (30 mg, 1.5×10^{-4} mol) in a 20-mL scintillation vial containing a solvent mixture of 10 mL DMF, 0.6 mL ethanol, and 0.6 mL H_2O. The vial was capped tightly and placed in an oven at 120 °C for 24 h to yield black microcrystalline powder.

14. Although all metals used in the synthesis were in the +2 oxidation state, we cannot rule out the possibility that several metals were oxidized during the synthesis and have been incorporated into the structure with a higher oxidation state. Bloch, E. D.; et al. *J. Am. Chem. Soc.* 2011, *133*, 14814–14822.

15. See experimental section for the description of synthesis, SEM images, thermogravimetric analysis, N_2 isotherms, and EDS mapping.

16. Methanol exchanged M10M-MOF-74 was evacuated under vacuum (100-200 mTorr) at room temperature for 12 h, and then heated at a constant rate 4 °C/min to 250 °C for 10 h in stepwise fashion (100 °C for 1 h, 150 °C for 1 h, and 200 °C for 1 h) under vacuum (30 mTorr).

17. SEM observations indicate that the particle size of M6M-, M8M-, and M10M-MOF-74 is smaller than that of M2M- and M4M-MOF-74. M6M-, M8M-, and M10M-MOF-74

contain metal ions that can have a coordination number of eight, which may hinder these metal ions' ability to react readily during the formation of the MM-MOF-74 structure. This is in sharp contrast to M4M-MOF-74 where such metals are not included in the synthesis. It is thus implied that the lowered crystallinity is caused by the presence of these metal ions rather than by the simple incorporation of many different types of metal ions within the MOF structure.

18. Elemental microanalysis: Calculated (%): C, 21.22; H, 3.83; N, 0.00; Mg, 1.57; Ca, 0.30; Sr, 0.54; Ba, 2.00; Mn, 2.89; Fe, 3.77; Co, 4.43; Ni, 4.02; Zn, 3.09; Cd, 4.27; Found (%): C, 21.41; H, 23.67; N, <0.1.

19. Rosi, N. L.; Kim, J.; Eddaoudi, M.; Chen, B.; O'Keeffe, M.; Yaghi, O. M. *J. Am. Chem. Soc.* 2005, *127*, 1504–1518.

5.6.1 Complete Ref. 14

14. Bloch, E. D.; Murray, L. J.; Queen, W. L.; Chavan, S.; Maximoff, S. N.; Bigi, J. P.; Krishna, R.; Peterson, V. K.; Grandjean, F.; Long, G. J.; Smit, B.; Bordiga, S.; Brown, C. M.; Long, J. R. *J. Am. Chem. Soc.* 2011, *133*, 14814–14822.

Chapter 6: Future Work

Flash Converted Graphene and Metal Organic Framework Composite for High Energy Pseudocapacitor Electrode

Abstract

With increasing demand for new technologies, energy storage devices are gaining more importance. Pseudocapacitors are potential candidates for high energy storage applications. One of the state-of-the-art electrode materials in terms of energy storage is hydrated ruthenium with a capacitance of 500-1300 F/g, but the high cost of ruthenium makes it impractical for widespread use. There are more cost-effective state-of-the-art pseudocapacitor electrode materials such as NiO, but their theoretical capacitance has not been achieved likely because they have low surface area and low accessibility of electrolyte ions to the metal ions. Thus, porous metal-organic frameworks (MOFs) have potential as pseudocapacitor electrode active material with the goal of having higher capacitances than current metal oxide electrodes. MOF materials have an advantage over metal oxides because of their extended porous structure which allows for more accessibility of the electrolyte to reach the metal ions. The approach will be to composite MOF particles with a conductive network of flash converted graphene (FCG) as the electrode active material. The MOF will be synthesized and homogeneously mixed with FCG. The dispersion slurry will be coated onto gold foil current collector. Characterizations will be done to evaluate the homogeneity and stability of the electrodes materials based on morphology, material composition and electronic properties. The MOF/FCG pseudocapacitor electrode will be tested using electrochemical methods such as cyclic voltammetry and constant current measurements.

6.1 Introduction

Supercapacitors are electrical energy storage devices with high power, composed of electrodes soaked in electrolyte, which can be aqueous salts, organic salts, ionic liquids, or a solid state gel salts.[1,2] The charge storage mechanism of a traditional supercapcaitor, the electric double layer capacitor (EDLC), is through electrostatic interactions at the electrode and electrolyte interface. The adsorption and desorption of electrolyte ions to the electrode material surface forms an electrochemical double layer establishing electroneutrality during charging and discharging. Current electrode materials include graphene, carbon nanotubes, and other pure forms of carbon.[3,4] EDLC contains no metal ions and thus generally have lower energy than metal ion containing devices such as Li ion batteries. Metal ions undergo redox charge transfer reactions during charging and discharging.[5] Li ion batteries, a different type of electrical energy storage device, stores electrical energy based on the migration and intercalation of Li^+ ions to and from the positive and negative electrodes. The positive electrode is often composed of a layer structured metal oxide such as $Li(Co)O_2$ or $Li(Mn)O_2$ that undergoes redox charge transfer reactions (Faradaic) when the Li^+ ions are intercalated.[6] Another newer type of energy storage device, pseudocapacitors, store electrical energy via redox charge transfer reactions of either organic materials, metal oxides, or metal oxide-carbon composites, similar to a Li ion battery, but the electrolyte ions only adsorb onto the surface instead of migrating between electrodes like for an EDLC. Thus, pseudocapacitors are able to store more energy (one order of magnitude higher capacitance) than EDLC devices and have higher power densities than Li ion batteries. Currently, metal oxides such as NiO, MnO_2, Fe_2O_3, Co_3O_4, ZnO, CuO, and V_2O_5 are used as

redox charge transfer (Faradaic) components in pseudocapacitors.[7-9] A NiO thin film electrode showed a high specific capacitance of 1776 F/g, but can only be operated at low currents. More realistic values for NiO electrode (nanoparticles) is 20-122 F/g (specific energy: 2-8.5 Wh/kg) with a surface area of 150 m^2/g and conductivity of 0.01-0.32 S/cm. Metal oxides are often composited with porous materials such as porous carbons and polymers to increase their capacitance.[10] A composite of NiO with activated carbon as a conducting support/binder gave a capacitance of 100 F/g (7 Wh/kg).[10] A NiO/CNT composite made by hydrothermal growth of NiO nanoparticles in a CNT suspension gave one of the highest capacitances reported for NiO-1600 F/g (111 Wh/kg).[11] Another state-of-the-art pseudocapacitor electrode material, hydrated RuO_2, has capacitances of 500-1300 F/g (34.7-90.3 Wh/kg), but is too costly to be practically implemented on a large scale.[12,13] Furthermore, it should be possible to reach even higher capacitances since the theoretical capacitances for many metal oxides are above 1000 F/g. As we have only reached a fraction their theoretical capacitances, i.e. NiO reached is 20-122 F/g with a theoretical value of 2584 F/g. One reason is because of their low surface area, i.e. NiO has a surface area of 150 m^2/g (the structure of NiO is face centered cubic). Thus, it is expected that the capacitance can be increased if the accessibility of electrolyte ions to the surfaces of the metal ions can be maximized.[11]

An alternative to metal oxides is metal organic frameworks (MOF), which are not only redox active, but also have the ability to store charge through electric double layers because of their high porosity and surface area. The metal joints and organic linkers of MOFs form a porous extended structure, with high surface area up to greater than >4000 m^2/g and pore diameters up

to 98 angstroms.[14-18] MOFs are obtained by a coordination of inorganic building units (SBUs) composed of metal ions or clusters with rigid organic molecular linkers. The resulting compound is a porous extended structure that can be 1D, 2D, or 3D. The atomistic connectivity of the MOF structure is easily designed by changing the combination of inorganic SBUs and organic linkers; therefore, several thousands of MOF structures have been reported in the last decade. Each MOF has different properties and thus are more useful towards different types of applications, the primary application being gas storage and separation because of their high porosity and high surface areas. Traditionally MOFs are made with carboxylate-based linkers, but recently there has been interest in using other types of linkers such as azolate-based linkers. These new linkers increase the variation of MOFs in terms of not only structure, but also properties and thus potentially expanding their applications.[16,19]

In future work, a series of MOFs, for example, MM-MOF-74 will be composited with flash converted graphene (FCG) to obtain both the high energy property of the redox active MOF material as well as the high power properties of the EDL FCG material. Furthermore, the FCG sheets can also serve to enhance the mechanical integrity to bind the MOF particles together. MOF is used because it not only contains different types of metals in its framework, but it also has high surface area. MM-MOF-74 is an ideal candidate because it contains more than one type of metal in one framework, allowing for the potential of more redox reactions. FCG is selected because of its excellent EDL behavior and low resistance.

6.2 Preparation and Characterization of Homogeneous MOF/FCG Electrode Slurries

The electrode slurry is to be prepared by adding x% MOF with 100-x% FCG with 1-5 mL water to produce a range of MOF:FCG mixing ratios (Table 6.1). Then, the mixture will be placed in a bath sonicator at room temperature until homogeneously mixed.

Scanning electron microscopy (SEM) characterization will be carried out to examine the morphology and make sure the MOF and FCG particles in the slurry dispersion are homogeneously distributed. The electrode slurry will be optimized to be uniform by modifying parameters such as sonication and stirring times. The electrode composite should look uniform with MOF particles and FCG interconnected.

Furthermore, conductivity measurements can be carried out on several different areas of the dried MOF/FCG electrodes to make sure the electrode preserves conductivity and to make sure the electrode is uniform. The conductivity measurements can be carried out using four-point probe measurements. The desired conductivity is on the order of 60 S/m, comparable to that of FCG. Although in reality, the conductivity is likely to be lower because of the non-existent conductivity of MOF. We expect to see a decrease in conductivity with increase in amount of MOF added.

X-ray diffraction (XRD) can also be done on the MOF/FCG electrodes to investigate the MOF and FCG after the electrode preparation steps such as sonication. For example, it will be important to explore whether the MOF and FCG are still intact and not degraded or undergone a phase change. Because the sonication is expected to break the particles into smaller nano-size particles, the diffraction peaks corresponding to the d-spacing are expected to broaden. The

specific particle size can also be calculated using Scherrer's equation, where the d-spacing can be calculated from Bragg's Law.

6.3 Fabrication of MOF/FCG Electrodes

To fabricate the MOF/FCG composite electrodes, 1-2 mL of the slurry will be drop-cast onto a gold foil current collector (commercially available). Kapton tape will be used to limit the gold foil to precisely 1 cm by 1 cm square to normalize the area of electrode, and to seal in the copper tape connector. The slurry will then be drop-cast onto the 1 cm^2 area. After drop-casting, the slurry will be allowed to dry overnight in air (Figure 6.1).

The electrode can be assembled in air under ambient conditions. There must be conductivity between the copper tape and the gold foil, a simple test using a voltmeter is sufficient. The contact resistance should be minimized. Also, the dried MOF/FCG electrode film must have good mechanical integrity and connection to the gold foil; if the film cracks then a binder such as Nafion can be added.

6.4 Testing of the MOF/FCG Electrodes Using Electrochemical Methods

The prepared electrode will to be first characterized using a three-electrode method, with the new composite electrode serving as the working electrode and a gold foil as a counter electrode and Ag/AgCl as the reference electrode. All electrodes will be connected to a potentiostat for EC measurements. The three-electrode method can give detailed information on the electrochemical behavior of the electrodes. The MOF component of the MOF/FCG electrode is expected to operate similar to a negative and positive electrode of a battery, depending on the metal ion and its oxidation states; for example, Co^{+2} and Fe^{+2} are expected to undergo oxidation

reactions to Co^{+3}, Fe^{+3}, and thus would work better as the negative electrode. However, the FCG component is expected to stabilize and balance the MOF allowing the MOF/FCG composite electrode to be able to serve as either negative or positive electrode. The FCG can act as either negative or positive electrode. Thus, we can also make a symmetric two electrode device from the MOF/FCG electrode, from which we can calculate a more accurate energy and power results (real application situation as compared to the three-electrode method).

The pertinent initial measurements to be carried out are cyclic voltammetry (CV) and constant current (CC). Capacitance can be obtained by using either CV or CC. Capacitance is defined as the ability for a system to store electrical charge, and is related to the amount of charge adsorbed in a given time over a given voltage (units of A•s/V or Farad).[5]

$$C = \frac{q}{V} \qquad \text{(Eq. 6.1)}$$

$$q = Idt \qquad \text{(Eq. 6.2)}$$

Where C is capacitance in Farads, q is charge in coulombs, V is electric potential or voltage in volts, I is current in amperes, and t is time in seconds. In cyclic voltammetry, an input potential is given and current is measured against the change in voltage (Figure 6.2a and 6.2b). Capacitance can be calculated by integrating the area under the I-V curve. In constant current measurement, the input is the current which is held constant, and voltage is measured vs. change in time (Figure 6.2c and 6.2d). The capacitance is also calculated from the slope of the curve. Furthermore, from either CV or CC, independent capacitance values for charging and discharging can be obtained by integrating the area under the charging or discharging curve separately. A CV that exhibits pure electrochemical double layer behavior, such as carbon

materials, will show no redox peaks while Faradaic pseudocapacitors will exhibit redox peaks corresponding to the redox potentials of the metals in the material (Figure 6.2a and 6.2b). A CC that exhibits pure electrochemical double layer behavior will show no redox peaks and little to no voltage drop due to resistance (Figure 6.2c). A CC curve of a Faradaic pseudocapacitor has redox peaks and voltage drop (Figure 6.2d).[5] After obtaining the capacitance value, the energy can be calculated. Electrical energy (E) depends on the amount of capacitance a system is able to store. The energy is also directly related to capacitance (C) and the voltage (V).[11]

$$E = qV = IdtV = CV^2 \quad \text{(Eq. 6.3)}$$

Further considerations have to be made to Equation 6.3 due to the configuration of the capacitor device tested. A factor of 1/2 is used in finding the energy of a two electrode system because the initial potential between the plates is 0, where the final potential is V so the average is V/2.

Because energy and power are related, another way to think of energy is by looking at the units; energy is power (P) multiplied by time (t) (Equation 6. 4)

$$E = Pt \quad \text{(Eq. 6.4)}$$

Power is characterized as the amount of energy that can be used in an instantaneously time (rate of doing work).

$$P = \frac{E}{t} = \frac{qV}{t} = IV \quad \text{(Eq. 6.5)}$$

With simple manipulation of the equation and using ohms law (V = IR), we can convert Equation 6.5 to include the measured metrics obtained from CV and CC. The energy and power can then be normalized. Some common normalizations are based on mass (gravimetric), area (areal), or volume (volumetric).[11]

6.5 Summary

Metal organic frameworks with different metals such as manganese, iron, cobalt, copper, and zinc are to be composited with FCG to make electrode active materials for a high energy pseudocapacitors. The electrodes will be fabricated by using FCG as a conducting network current collector and binder. MOF and FCG will be sonicated and made into a homogeneous composite dispersion in water. Characterizations of the electrode morphology, composite materials, and electronic properties will be carried out using SEM, XRD, and conductivity measurements. The electrode will be assembled and tested using a potentiostat. The electrochemical tests include cyclic voltammetry and constant current measurements. The capacitance, energy, and power will be investigated.

6.6 Tables and Figures

Table 6.1 Example of Initial Experiments with x% MOF and 100-x% FCG.

Trial	1	2	3	4	5	6	7
MOF	5%	10%	15%	20%	30%	40%	50%
FCG	95%	90%	85%	80%	70%	60%	50%

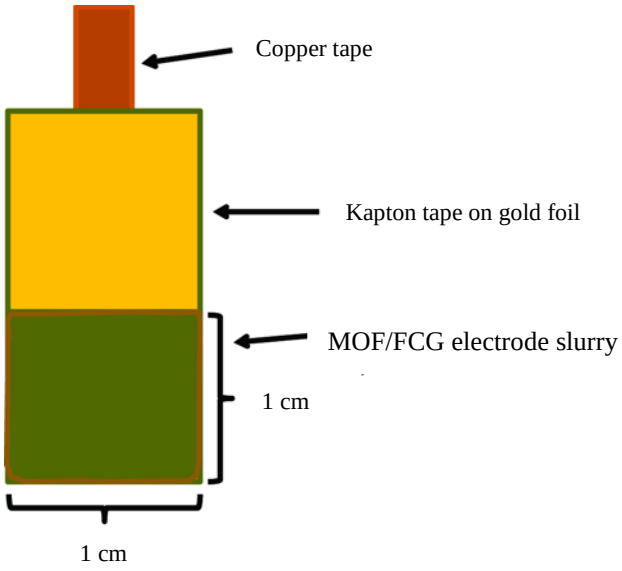

Figure 6.1 Electrode of the proposed MOF/FCG composite material.

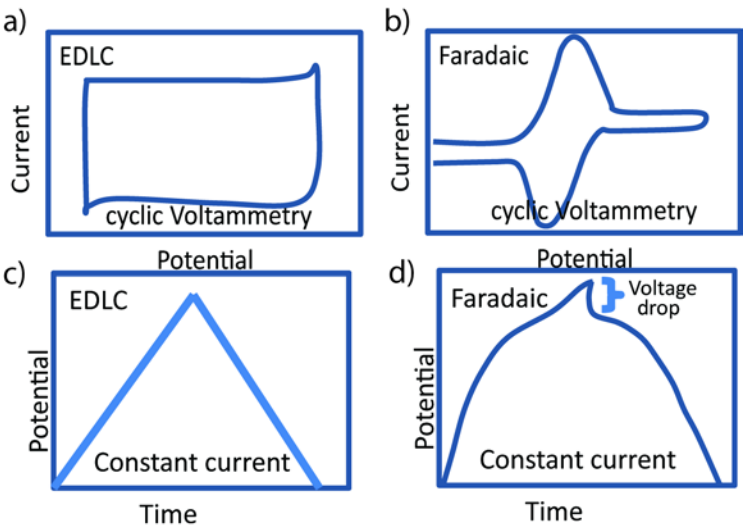

Figure 6.2 Examples of CV curves expected for EDLCs (a), and for Faradaic reactions such as in pseudocapacitors (b). Examples of CC curves for EDLCs (c), and for Faradaic reactions (d).

6.7 References

1. Winter, M.; Brodd, R. J. *Chemical reviews* 2004, 104, 4245-4270.
2. Davies, A.; Yu, A. *The Canadian Journal of Chemical Engineering* 2011, 89, 1342-1357.
3. Pandolfo, A. G.; Hollenkamp, A. F. *Journal of Power Sources* 2006, 157, 11-27.
4. Zhang, L. L.; Zhao, X. S. *Chemical Society Reviews* 2009, 38, 2520-2531.
5. Bard, A. J., Faulkner, Larry R. Electrochemical Methods: Fundamentals and Applications *John Wiley & Sons, Inc., New York* 2001, 87-90, 137-141.
6. Mizushima, K.; Jones, P.; Wiseman, P.; Goodenough, J. *Materials Research Bulletin* 1980, 15, 783-789.
7. Halper, M. S.; Ellenbogen, J. C. Supercapacitors: A brief overview. *Report No. MP 05W0000272, The MITRE Corporation, McLean, Virginia* 2006.
8. Chen, Y.-L.; Hu, Z.-A.; Chang, Y.-Q.; Wang, H.-W.; Zhang, Z.-Y.; Yang, Y.-Y.; Wu, H.-Y. *The Journal of Physical Chemistry C* 2011, 115, 2563-2571.
9. Kalpana, D.; Omkumar, K.; Kumar, S. S.; Renganathan, N. *Electrochimica acta* 2006, 52, 1309-1315.
10. Xu, C.; Kang, F.; Li, B.; Du, H. *Journal of materials research* 2010, 25, 1421.
11. Zhi, M.; Xiang, C.; Li, J.; Li, M.; Wu, N. *Nanoscale* 2013, 5, 72-88.
12. Song, M.-K.; Cheng, S.; Chen, H.; Qin, W.; Nam, K.-W.; Xu, S.; Yang, X.-Q.; Bongiorno, A.; Lee, J.; Bai, J. *Nano letters* 2012, 12, 3483-3490.
13. McKeown, D. A.; Hagans, P. L.; Carette, L. P.; Russell, A. E.; Swider, K. E.; Rolison, D. R. *The Journal of Physical Chemistry B* 1999, 103, 4825-4832.

14. Gándara, F.; Uribe-Romo, F. J.; Britt, D. K.; Furukawa, H.; Lei, L.; Cheng, R.; Duan, X.; O'Keeffe, M.; Yaghi, O. M. *Chemistry-A European Journal* 2012, 18, 10595-10601.

15. Rosi, N. L.; Kim, J.; Eddaoudi, M.; Chen, B.; O'Keeffe, M.; Yaghi, O. M. *Journal of the American Chemical Society* 2005, 127, 1504-1518.

16. Furukawa, H.; Cordova, K. E.; O'Keeffe, M.; Yaghi, O. M. *Science* 2013, 341, 1230444.

17. Deng, H.; Grunder, S.; Cordova, K. E.; Valente, C.; Furukawa, H.; Hmadeh, M.; Gándara, F.; Whalley, A. C.; Liu, Z.; Asahina, S. S*cience* 2012, 336, 1018-1023.

18. An, K. H.; Kim, W. S.; Park, Y. S.; Moon, J.-M.; Bae, D. J.; Lim, S. C.; Lee, Y. S.; Lee, Y. H. *Advanced Functional Materials* 2001, 11, 387-392.

19. Gao, W.-Y.; Yan, W.; Cai, R.; Meng, L.; Salas, A.; Wang, X.-S.; Wojtas, L.; Shi, X.; Ma, S. *Inorganic chemistry* 2012, 51, 4423-4425.